Faqeeh, Abdulhai Hani A. (2025) *Exploring zero-gap water electrolysis technologies: benchmarking, evaluation, and comparative analysis.* PhD thesis.

https://theses.gla.ac.uk/85311/

Exploring Zero-gap Water Electrolysis Technologies: Benchmarking, Evaluation, and Comparative Analysis

Abdulhai Hani A. Faqeeh

Submitted in fulfilment of the requirements for the Degree of Doctor of Philosophy

School of Chemistry

College of Science and Engineering

University of Glasgow

January 2025

For my parents and my beloved wife Afnan

Abstract

Water electrolysis is a promising process to produce green hydrogen, a sustainable and environmentally friendly fuel and a crucial chemical used in numerous industrial applications. Zero-gap water electrolysers have become a key technology for green hydrogen production, mainly due to their high efficiency and hydrogen purity and their rapid response to a wide range of operating conditions and intermittent electricity, facilitating their coupling with renewable energy sources. In Chapter 1, the fundamentals and history of the water electrolysis process are discussed, and the low-temperature water electrolyser technologies are introduced. Moreover, the key evaluation parameters of water electrolysis electrocatalysts are reported. In Chapter 2, all the experimental techniques used throughout this work are introduced and discussed, covering their theoretical background and operation principles.

In Chapter 3, a standard anion exchange membrane water electrolyser, a type of zero-gap electrolyser design, is developed and optimised to be used as a universal testbed for evaluating novel electrocatalysts and other components of (anion exchange membrane) water electrolysis. The benchmark is developed because of the absence of a reliable evaluating protocol due to variations in testing conditions and water electrolyser components across studies, obstructing a comprehensive and cohesive comparison of new electrocatalysts (or other components of anion exchange membrane water electrolysis technology). The construction and operation of the standard water electrolyser are described in detail. In addition, 3D drawings of the water electrolyser components are provided (located in the University of Glasgow's open access data repository, https://researchdata.gla.ac.uk/1672/), enabling others to construct and operate their own identical flow cell.

In Chapter 4, the flow cell introduced in Chapter 3 is used to evaluate a new commercially available polymer membrane as an alternative proton exchange membrane to Nafion and Aquivion membranes, which have been in short supply recently. The performance, stability, and hydrogen crossover characteristics of the new membrane is evaluated and compared to those of the Nafion and Aquivion membranes.

In Chapter 5, the standard water electrolyser developed and optimised in Chapter 3 is adopted to evaluate a radiation-grafted anion exchange membrane supplied by a research team based at the University of Surrey. The membrane is assessed and compared to a commercial anion exchange membrane (FAA-3-50).

Table of Contents

List of publications

1. A.H. Faqeeh, M.D. Symes, A standard electrolyzer test cell design for evaluating catalysts and cell components for anion exchange membrane water electrolysis, Electrochim. Acta 444 (2023) 142030, https://doi.org/10.1016/j.electacta.2023.142030.

2. A.K. Samuel, A.H. Faqeeh, W. Li, Z. Ertekin, Y. Wang, J. Zhang, N. Gadegaard, D.A.J. Moran, M.D. Symes, A.Y. Ganin, Assessing Challenges of 2D-Molybdenum Ditelluride for Efficient Hydrogen Generation in a Full-Scale Proton Exchange Membrane (PEM) Water Electrolyzer, ACS Sustain. Chem. Eng. 12 (2023) 1276–1285, https://doi.org/10.1021/acssuschemeng.3c06616.

3. A.H. Faqeeh, M.D. Symes, Zero-gap bipolar membrane water electrolyzers: Principles, challenges and practical insights, Electrochim. Acta 493 (2024) 144345, https://doi.org/10.1016/j.electacta.2024.144345.

List of conferences

1. **Electrochem 2022,** Edinburgh, UK from 4 – 6 September 2022.
Poster presentation: “Anion Exchange Membrane Water Electrolysis (AEMWE) Benchmark”.

2. **74th Annual Meeting of the International Society of Electrochemistry (ISE)**, Lyon, France from 3 – 8 September 2023.
Oral presentation: “A standard electrolyzer test cell design for evaluating catalysts and cell components for anion exchange membrane water electrolysis”.

3. **Energy Transition and NET-ZERO Carbon Capture Technologies (Powering Tomorrow)**, Oxford, UK on July 30, 2024.
Oral presentation: “A standard electrolyzer test cell design for evaluating catalysts and cell components for anion exchange membrane water electrolysis”.

4. **38th Topical Meeting of the International Society of Electrochemistry**, Manchester, UK, from 8 – 11 September 2024.
Poster presentation: “A Standard Operating Procedure for Air-spray Deposition of Oxygen Evolution Reaction Electrocatalysts in Proton Exchange Membrane Water Electrolysis”.

Acknowledgements

First, I express my deepest gratitude to God (Allah), the Most Gracious and the Most Merciful, for providing the blessings and creating the conditions necessary to complete this work.

I express my deep appreciation to my PhD supervisor Prof. Mark Symes for his instrumental and invaluable guidance, throughout my entire postgraduate journey, which started since my master program at the University of Glasgow. I owe him immense gratitude for his patience, constructive feedback, and supportive personality. Without his supervisory, the completion of this work would not have been possible.

I would like to show my gratitude to my beloved wife Afnan for her unwavering love, support, and patience during this journey. I am thankful for all the moments we have spent together, which were full of happiness and joy. I cannot thank you enough for the immense pleasure you have brought into my life.

I am thankful as well for my parents, who were a significant part of my success. I express my gratitude for your prayers, love, and patience for being away from you for all these years. I will forever be indebted to you for your love and compassion. I also extend my immense gratitude to all my siblings for their love and patience.

My appreciation also extends to all my colleagues, especially Dr. Zeliha Ertekin for her advice and support throughout my PhD journey, and Dr. Patrick McHugh for introducing me to a flow cell for the first time. A special thanks to King Khalid University and the government of Saudi Arabia for their great support and funding of studies.

Finally, I am thankful to all the friends I met in Glasgow for all the help and good times we have spent together. Especially, a deep gratitude is expressed to my close friend Dr. Saad Noor Wali for the considerable help and advice he has given me in Glasgow.

Author's declaration

I declare that, except where explicit reference is made to the contribution of others, this thesis is the result of my own work and has not been submitted for any other degree at the University of Glasgow or any other institution.

I declare that this thesis has been produced in accordance with the University of Glasgow's Code of Good Practice in Research.

I acknowledge that if any issues are raised regarding good research practice based on review of the thesis, the examination may be postponed pending the outcome of any investigation of the issues.

Abdulhai Hani A. Faqeeh

List of Abbreviations and symbols

a	activity
AC	alternating current
AEM	anion exchange membrane
η_a	anodic overpotential
ASR	area specific resistance
N_A	Avogadro constant
M	catalyst active site
η_c	cathodic overpotential
Q	charge coulombs (C)
CCM	catalyst-coated membrane
CCS	catalyst-coated substrate
CAD	computer-aided design
CVD	chemical vapor deposition
j	current density
ECSA	electrochemical surface area
ΔH	enthalpy
F	Faraday constant
FT-IR	Fourier-Transform infrared
f_{H_2}	fugacity of hydrogen gas
f_{O_2}	fugacity of oxygen gas
HER	hydrogen evolution reaction
ICP-OES	inductively coupled plasma optical emission spectrometry
LOM	lattice oxygen mechanism
E_M	membrane resistance
MEA	membrane electrode assembly
MPL	microporous layer
n	number of electrons
m	number of moles
η_R	ohmic overpotential
iR_{cell}	ohmic resistance
E	operational potential
OER	oxygen evolution reaction

ETFE	poly(ethylene-co-tetrafluoroethylene)
PFAS	polyfluoroalkyl substances
ppb	part per billion
ppm	part per million
E_{pH}	pH gradient overpotential
PTFE	polytetrafluoroethylene
PEM	proton exchange membrane
$E°_{cell}$	standard cell potential
$\Delta H°$	standard enthalpy
$\Delta S°$	standard entropy
$\Delta G°$	standard Gibbs free energy
SHE	standard hydrogen electrode
Γ	surface catalytic active site
θ	surface coverage
b	Tafel slope
$E°$	theoretical potential
TOF	Turnover frequency

Chapter 1: Introduction

Most of Section 2 (Overview of low-temperature electrolyser technologies) in this Chapter is adapted from a published review; “A.H. Faqeeh, M.D. Symes, Zero-gap bipolar membrane water electrolysers: Principles, challenges and practical insights, Electrochim. Acta 493 (2024) 144345, https://doi.org/10.1016/j.electacta.2023.142030”. The manuscript of the published review was written by me, then edited by my supervisor for publication.

Acknowledgements and declarations

I acknowledge the Geoanalytical Electron Microscopy and Spectroscopy (GEMS) facility at the University of Glasgow for the support and assistance with performing the scanning electron microscope imaging for Figure 15 and 16.

1.1. Fundamentals of water electrolysis

1.1.1. Overview of hydrogen and water electrolysis

Using fossil fuels, including natural gas, coal, and oil, as energy sources has negative environmental and health-related impacts, whereby carbon dioxide and various noxious pollutants, such as nitrogen dioxides and sulfur dioxides, are released. In contrast, hydrogen is a sustainable and environmentally friendly energy source due to its zero-carbon emissions and high abundance as an element combined with numerous other elements [1]. It is also an efficient energy carrier, which can be used in fuel cells or internal combustion engines, providing high calorific value of ~ 142 MJ kg^{-1} [2], providing the second best, after Uranium, energy-to-weight ratio compared to all conventional fuels [3]. Additionally, hydrogen has numerous uses as a valuable chemical in many industrial applications, including ammonia production, direct reduction of iron, methanol production, petroleum refining (e.g. desulfurization), etc [4]. However, hydrogen is mostly generated using the endothermic steam-methane reforming reaction (equation 1) coupled with the exothermic water gas-shift reaction (equation 2) [5]. The steam-methane reforming process operates at ~ 800 °C – 1000 °C, consuming substantial amounts of energy and releasing immense carbon emissions.

$$CH_4 + H_2O \rightarrow CO + 3H_2 \qquad \Delta H = +206.1\ \text{kJ mol}^{-1} \qquad (1)$$

$$CO + H_2O \rightarrow CO_2 + H_2 \qquad \Delta H = -42.2\ \text{kJ mol}^{-1} \qquad (2)$$

Thus, environmentally friendly alternative hydrogen production processes operating under ambient conditions should be used. Water electrolysis for green hydrogen production with zero-carbon emissions is a crucial process for the renewable energy transition, due to the feasibility of coupling water electrolysis technologies to renewable energy resources, such as solar and wind energy [6]. In this process, hydrogen is generated from water with zero carbon footprint, whereby water splits electrochemically into oxygen and hydrogen gases via a thermodynamically non-spontaneous reaction, consuming an energy of +286 kJ mol^{-1} at standard temperature and pressure (equation 3) [7].

$$2H_2O + \text{electric current} \rightarrow O_2 + 2H_2 \qquad \Delta G^\circ = +286 \text{ kJ mol}^{-1} \qquad (3)$$

1.1.2. A brief history of water electrolysis

The identification of hydrogen as an element was made by Henry Cavendish in 1766, whereby he collected the hydrogen gas generated by the reaction of a strong acid with different metals (Figure 1).

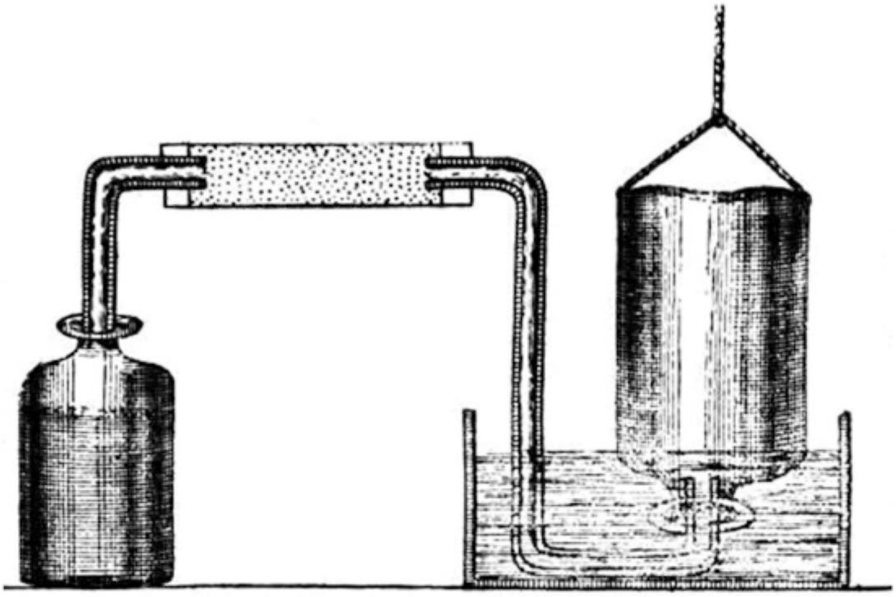

Figure 1: *Henry Cavendish's equipment for producing hydrogen gas in the left-hand container by the reaction of a strong acid with a metal and collecting the hydrogen gas over water in the right-hand upturned container. Reproduced from [8], page 3. Copyright 2023 Springer.*

After this discovery, hydrogen production through the water electrolysis process was discovered by Adriaan Paets van Troostwijk and Jan Rudolph Deiman in 1789 by using an electrostatic generator producing electricity between two gold electrodes submerged in water [9]. Later, William Nicholson and Anthony Carlisle decomposed water into hydrogen and oxygen gases successfully using the first electric battery (the Voltaic pile) in 1800 (Figure 2) [10].

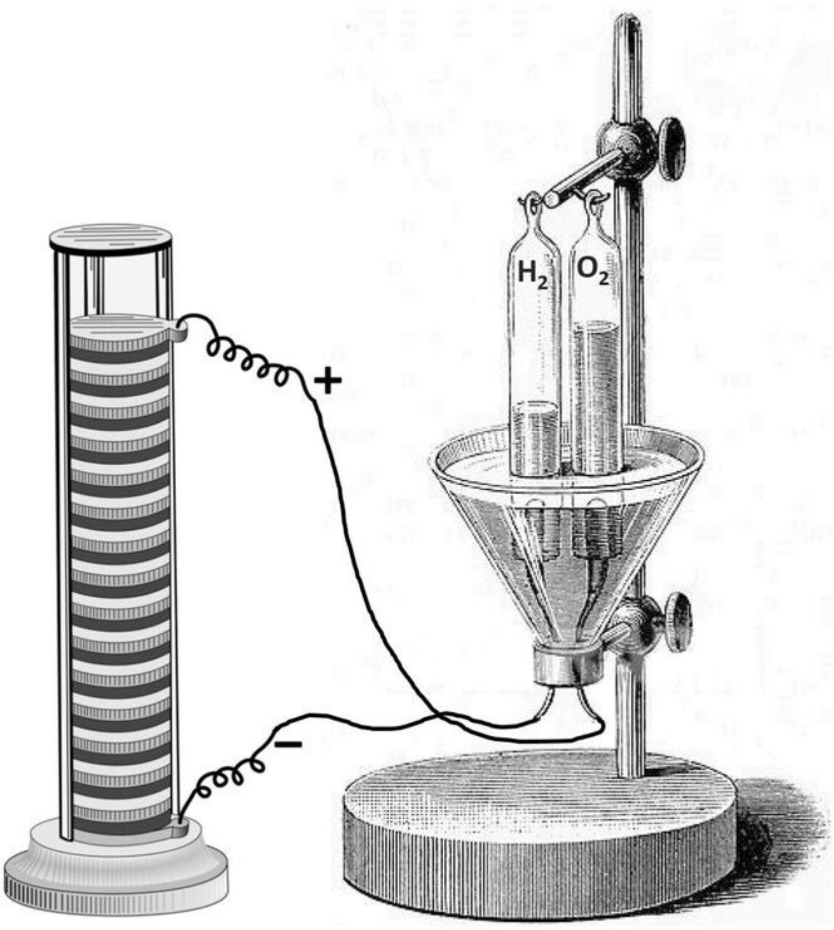

Figure 2: *Schematic illustration of Nicholson and Carlisle's system for water electrolysis using a Voltaic pile (battery) coupled to the electrodes submerged in water. Reprinted with permission [10]. Copyright 2021 Wiley-VCH.*

In 1833, Faraday's first law of electrolysis (equation 4) was published by Michael Faraday, leading to the quantitative relationship between the amount of electric charge transferred and the amount of hydrogen generated [11].

$$Q = mnF \tag{4}$$

where Q is the total charge passed through the electrolyte in coulombs (C), m is the number of moles of the substance deposited or liberated at a surface of an electrode throughout electrolysis, n is the number of electrons transferred per mole of electroactive species, and F is the Faraday constant (96,485 C mol^{-1}).

The first industrial system for hydrogen production by water electrolysis was established by Dmitry Lachinov in 1888; more than 400 industrial water electrolysers were already in operation by 1902 [11]. In the mid-1950s, the solid polymer electrolyte water electrolysis system was introduced by General Electric [12], featuring a compact design containing a solid sulfonated polystyrene membrane acting as a solid polymer electrolyte. In 1966, the Dupont company developed the first perfluorinated membrane, marketed under the trade name Nafion, marking a considerable breakthrough in hydrogen production technology, due to the superior mechanical durability and electrochemical properties of the membrane [13].

1.1.3. Principles of water electrolysis

Water electrolysis is a process for green hydrogen production, with zero carbon emissions, using electricity as a driving force for splitting water into oxygen and hydrogen gases. A typical electrolytic cell comprises four main components: an electrolyte (either acidic, alkaline, or neutral) which conducts ions, cathode and anode electrodes, whereat reactions occur, a membrane separating the cathodic and anodic compartments, and an external power supply (Figure 3). In the water electrolysis process, two half-reactions occur at the electrode/electrolyte interfaces: the oxygen evolution reaction (OER) at the anode electrode and the hydrogen evolution reaction (HER) at the cathode electrode. Under acidic media, the OER occurs through the dissociation of two water molecules, releasing one oxygen molecule, four protons, and four electrons (equation 5), which travel through an external circuit, while the protons permeate through the membrane to the cathode compartment. At the cathode electrode, the HER takes place through the reduction of the four protons, releasing two hydrogen molecules (equation 6).

$$\text{Anodic reaction: } 2H_2O \rightarrow O_2 + 4e^- + 4H^+ \qquad (5)$$

$$\text{Cathodic reaction: } 4e^- + 4H^+ \rightarrow 2H_2 \qquad (6)$$

In contrast, under basic or neutral conditions, the water molecules dissociate at the cathode, generating two hydrogen molecules and four hydroxide ions (equation 7). The hydroxide ions travel through a diaphragm to the anode compartment, wherein they are oxidised at the anode electrode, releasing two water molecules, one oxygen molecule, and four electrons (equation 8).

$$\text{Cathodic reaction: } 4H_2O + 4e^- \rightarrow 2H_2 + 4OH^- \qquad (7)$$

$$\text{Anodic reaction: } 4OH^- \rightarrow 2H_2O + O_2 + 4e^- \qquad (8)$$

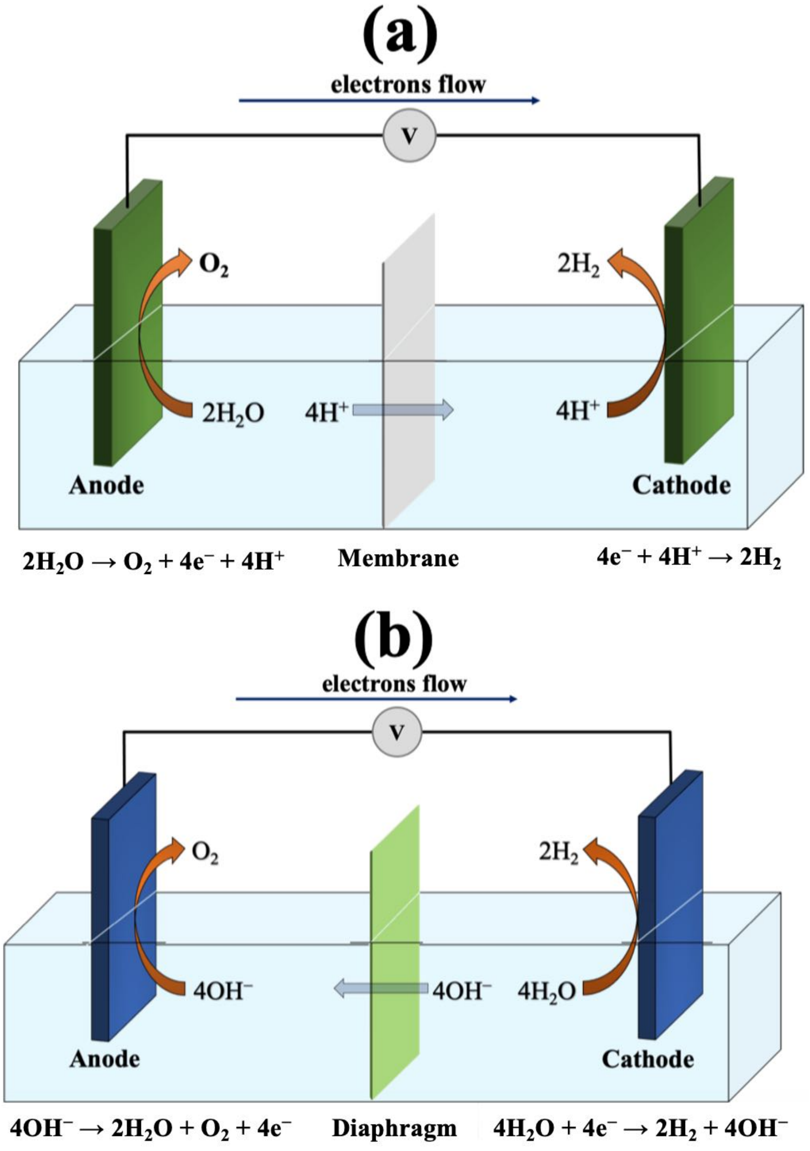

Figure 3: *Water electrolysis under (a) acidic and (b) neutral or alkaline conditions.*

1.1.3.1. Thermodynamics of the water electrolysis process

The water electrolysis process includes the conversion of heat and electrical energy to chemical energy, stored in the form of hydrogen molecules. Water electrolysis is an endothermic process requiring a minimal theoretically energy (ΔH) of +286 kJ mol^{-1} at standard conditions of temperature and pressure ($T° = 298$ K, $P° = 1$ atm) to split one mole of water, as shown in equation 9 [14].

$$\Delta G° = \Delta H° + T\Delta S° \qquad (9)$$

where $\Delta G°$ and $T\Delta S°$ represent the Gibbs free energy and entropy terms for the water dissociation process at standard conditions, respectively.

The Gibbs free energy ($\Delta G°$) maps onto the minimal theoretical electrical energy (i.e. the reversible cell potential) of 237 kJ mol^{-1} required to split one mole of water at standard conditions. This electrical energy required for splitting one mole of water (237 kJ mol^{-1}) equals an electrical potential of 1.23 V, as calculated by equation 10.

$$\Delta G° = -nFE°_{cell} \qquad (10)$$

where n is the number of electrons (2 electrons) transferred by splitting one water molecule (Equation 3), and F is the Faraday constant (96,485 C mol^{-1}).

The remaining energy (~ 49 kJ mol^{-1}) could be supplied as heat from the surroundings, due to the entropic contribution ($\Delta S° = 0.163$ kJ mol^{-1} K^{-1}), whereby the water splitting reaction generates 1.5 mole of gaseous species (i.e. higher entropy than the initial situation) [15]. Thus, although $\Delta H°$ is a temperature-independent parameter in water electrolysis, increasing the operational temperature does reduce the electrical potential required, whereby higher heat is supplied to the reaction [16]. In the case the $\Delta H°$ of +286 kJ mol^{-1} required for splitting one mole of water is supplied completely as electrical energy, a thermoneutral potential of 1.48 V is required for splitting one mole of water at standard conditions [14].

Nonetheless, in practice, a higher potential is needed for water electrolysis to occur, due to the kinetic energy barriers required for the two half-reactions of water electrolysis, the internal ohmic resistance within the electrochemical cell, and the mass transport limitations, as demonstrated by equation 11 [16]. Thus, hydrogen and oxygen evolution reaction electrocatalysts should be employed to reduce these kinetic energy barriers.

$$E = E^{\circ} + \eta_c + \eta_a + \eta_R + \eta_{mass} \quad (11)$$

where E and E° depict the operational and theoretical potentials required for water electrolysis, η_R represents the voltage “dropped” due to ohmic resistance, and η_c, η_a depict the overpotentials arising from the kinetic energy barriers of the hydrogen and oxygen evolution reactions, respectively. The mass transport overpotential is represented as η_{mass}.

1.1.3.2. The effect of pH on the water electrolysis potential

The two half-reactions of water electrolysis require electrical potentials of 0 V vs. SHE for hydrogen evolution reaction and 1.23 V vs. SHE for oxygen evolution reaction, at standard conditions, when the pH of the catholyte and anolyte is 0. However, the change in pH does affect the potential, whereby each half-reaction depends on the reactant chemical activity according to Nernst equation for the anodic reaction (equation 12) and cathodic reaction (equation 13) [15].

$$E_{anode} = E^{\circ}{}_{H_2O/O_2} - \frac{RT}{2F} \ln \frac{(a_{H^+})^2 \times (f_{O_2})^{\frac{1}{2}}}{a_{H_2O}} \quad (12)$$

$$E_{cathode} = E^{\circ}{}_{H^+/H_2} - \frac{RT}{2F} \ln \frac{f_{H_2}}{(a_{H^+})^2} \quad (13)$$

where E° represents the standard potential for the two half-reactions, R represents the universal gas constant (8.314 J mol^{-1} K^{-1}), F represents the Faraday constant (96,485 C mol^{-1}), a_{H^+} represents the activity of protons in the electrolyte, a_{H_2O} represents the activity of water in the anolyte, and f_{H_2} and f_{O_2} represent the fugacity of hydrogen and oxygen gases in the cathode and anode compartments, respectively.

Equations 12 and 13 can be simplified into equations 14 and 15, respectively:

$$E_{anode} = 1.23\ \text{V (vs. SHE)} - 0.059\ \text{V} \times pH_{anode} \quad (14)$$

$$E_{cathode} = 0\ \text{V (vs. SHE)} - 0.059\ \text{V} \times pH_{cathode} \quad (15)$$

where 59 mV more cathodic potential is required for the hydrogen evolution reaction at pH 1, while 59 mV less anodic potential is required for the oxygen evolution reaction at pH 1.

Thus, the thermodynamic potentials for the hydrogen and oxygen evolution reactions, for example, in high alkaline media (pH = 14) can be calculated from equation 16 and 17, respectively:

$$E_{anode} = 1.23\ \text{V (vs. SHE)} - 0.059\ \text{V} \times 14 = +0.404\ \text{vs. SHE} \quad (16)$$

$$E_{cathode} = 0\ \text{V (vs. SHE)} - 0.059\ \text{V} \times 14 = -0.826\ \text{vs. SHE} \quad (17)$$

The water electrolysis electrode potentials as a function of pH at standard conditions can be displayed as an E-pH plot called Pourbaix diagram (Figure 4). This plot maps the conditions of pH and electric potential and shows where different species are stable [17].

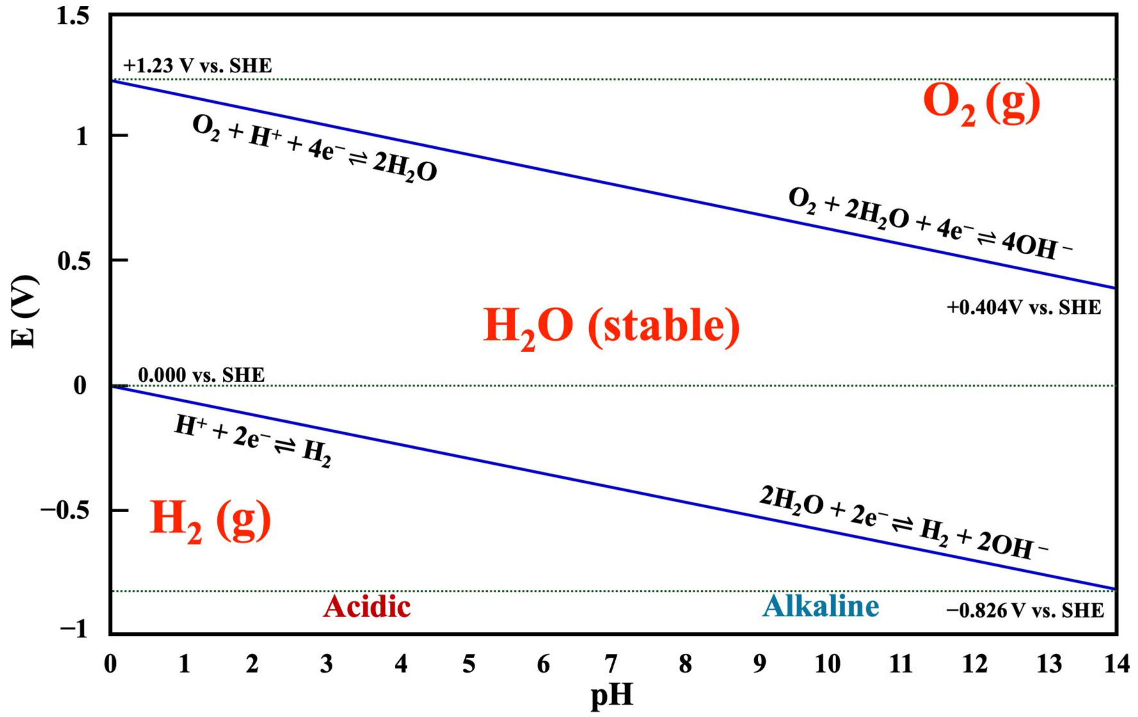

Figure 4: *The Pourbaix diagram of the redox potentials for water electrolysis at standard conditions.*

1.1.3.3. Basic mechanisms of the hydrogen and oxygen evolution reactions

The hydrogen evolution reaction is a two electron-transfer process taking place through two possible two-step mechanisms: Volmer-Heyrovsky and Volmer-Tafel mechanisms. Both mechanisms begin with converting protons into H_{ad} intermediate (an uncharged hydrogen atom adsorbed onto the electrode surface) by combining a proton (under acidic conditions) or water molecule (under neutral and alkaline conditions) with an electron at the cathode surface. This first adsorption step is called the Volmer step, and it is followed by either the Heyrovsky step or the Tafel step [16]. In the Heyrovsky step, under acidic conditions, the hydrogen adatom (H_{ad}) reacts with a proton from electrolyte in the presence of an electron, producing a hydrogen molecule. Under alkaline or neutral conditions, a hydrogen molecule is produced through the simultaneous reaction of H_{ad} with a water molecule from electrolyte and an electron. In contrast, in the Tafel step, a hydrogen molecule is produced due to the coupling of two adjacent hydrogen adatoms in the presence of two electrons (under all-pH conditions) [18]. Equations for the two hydrogen evolution reaction mechanisms are illustrated in Table 1.

Table 1: *The most reported mechanisms for the hydrogen evolution reaction [17,19–21].*

The hydrogen evolution reaction under acidic conditions	The hydrogen evolution reaction under neutral/alkaline conditions
$H^+ + e^- + M \rightarrow H_{ad}$ (Volmer) $H^+ + e^- + H_{ad} \rightarrow H_2 + M$ (Heyrovsky) $2H_{ad} \rightarrow H_2 + 2M$ (Tafel)	$H_2O + e^- + M \rightarrow OH^- + H_{ad}$ (Volmer) $H_2O + e^- + H_{ad} \rightarrow H_2 + OH^- + M$ (Heyrovsky) $2H_{ad} \rightarrow H_2 + 2M$ (Tafel)

where “M” and “ad” represent the catalyst active site at the surface of the electrode material.

The oxygen evolution reaction is kinetically less favourable compared to hydrogen evolution reaction, due to the transfer of multiple electrons and protons and the formation of multiple intermediates (HO_{ad}, O_{ad}, HOO_{ad}, and OO_{ad}) during the oxygen evolution reaction process. Although there are many mechanisms proposed in the literature for this process [22], the most reported mechanisms in the literature for this process will be discussed only, and they are illustrated in Table 2.

The traditional adsorbate evolution mechanism for the oxygen evolution reaction can be divided into two well-known pathways: the Eley–Rideal and the Langmuir–Hinshelwood mechanisms, which differ in terms of the formation of the OO_{ad} intermediate. In both pathways, the reaction starts with forming the HO_{ad} intermediate that converts to the O_{ad} intermediate subsequently under all-pH conditions. The production of O_2 is achieved through the formation of the OO_{ad} intermediate that decompose, releasing oxygen molecule. In case of Eley–Rideal pathway, one O_{ad} intermediate reacts with either a water molecule (under acidic conditions) or OH^- (under neutral and alkaline conditions), forming one HOO_{ad} intermediate, which further oxidises to the OO_{ad} intermediate, producing O_2 subsequently. In contrast, in the Langmuir-Hinshelwood adsorbate evolution reaction pathway, the OO_{ad} intermediate is formed through the interaction between two adsorbed deprotonated oxygen atoms ($2O_{ad}$), forming an adsorbed $_{ad}O\text{-}O_{ad}$ complex. This complex reacts with a water molecule (under acidic conditions) or OH^- (under neutral and alkaline conditions) to form the OO_{ad} intermediate, subsequently forming an oxygen molecule [14,17]. Moreover, the lattice oxygen mechanism (LOM) is another well-known mechanism proposed for the oxygen evolution reaction, wherein the adsorbates may react with the catalyst active site and lattice oxygen atoms within the structure of the electrode material as well. This mechanism is like the Langmuir–Hinshelwood-based adsorbate evolution mechanism in terms of bypassing the formation of the HOO_{ad} intermediate. However, it differs by forming an oxygen vacancy defect, acting as an active site, upon the release of O_2 from the catalyst surface [11,17].

Table 2: *The most reported mechanisms for the oxygen evolution reaction [17,21,23].*

(a) The oxygen evolution reaction under acidic conditions (Eley–Rideal adsorbate evolution reaction pathway)	(b) The oxygen evolution reaction under neutral and alkaline conditions (Eley–Rideal adsorbate evolution reaction pathway)
(1) $H_2O + M \rightarrow HO_{ad} + H^+ + e^-$ (2) $HO_{ad} \rightarrow O_{ad} + H^+ + e^-$ (3) $O_{ad} + H_2O \rightarrow HOO_{ad} + H^+ + e^-$ (4) $HOO_{ad} \rightarrow H^+ + e^- + OO_{ad}$ (5) $OO_{ad} \rightarrow O_2 + M$	(1) $OH^- + M \rightarrow HO_{ad} + e^-$ (2) $HO_{ad} + OH^- \rightarrow O_{ad} + H_2O + e^-$ (3) $O_{ad} + OH^- \rightarrow HOO_{ad} + e^-$ (4) $HOO_{ad} + OH^- \rightarrow OO_{ad} + H_2O + e^-$ (5) $OO_{ad} \rightarrow O_2 + M$
(c) The oxygen evolution reaction under acidic condition (Langmuir-Hinshelwood adsorbate evolution reaction pathway)	(d) The oxygen evolution reaction under neutral and alkaline conditions (Langmuir-Hinshelwood adsorbate evolution reaction pathway)
(1) $H_2O + M \rightarrow HO_{ad} + H^+ + e^-$ (2a) $HO_{ad} \rightarrow O_{ad} + H^+ + e^-$ (2b) $HO_{ad} \rightarrow O_{ad} + H^+ + e^-$ (3) $O_{ad} + O_{ad} \rightarrow {}_{ad}O\text{-}O_{ad}$	(1) $OH^- + M \rightarrow HO_{ad} + e^-$ (2a) $HO_{ad} + OH^- \rightarrow O_{ad} + H_2O + e^-$ (2b) $HO_{ad} + OH^- \rightarrow O_{ad} + H_2O + e^-$ (3) $O_{ad} + O_{ad} \rightarrow {}_{ad}O\text{-}O_{ad}$ (4) ${}_{ad}O\text{-}O_{ad} + OH^- \rightarrow OO_{ad} + e^- + HO_{ad}$

(4) ${}_{ad}O\text{-}O_{ad} + H_2O \rightarrow OO_{ad} + H_2O_{ad}$ (5) $H_2O_{ad} \rightarrow H^+ + e^- + HO_{ad}$ (6) $OO_{ad} \rightarrow O_2 + M$	(5) $OO_{ad} \rightarrow O_2 + M$
(c) The oxygen evolution reaction under neutral and alkaline conditions (lattice oxygen mechanism)	
(1a) $OH^- + M\text{-}\mathbf{O} \rightarrow HO_{ad}\mathbf{o} + e^-$ (2a) $HO_{ad}\mathbf{o} + OH^- \rightarrow O_{ad}\mathbf{o} + H_2O + e^-$ (3a) $O_{ad}\mathbf{o} \rightarrow O_2 + e^-$ or (1b) $M\text{-}\mathbf{O} \rightarrow M\text{-vacancy}$ (2b) $M\text{-vacancy} + OH^- \rightarrow H\mathbf{O}_{ad} + e^-$ (3b) $H\mathbf{O}_{ad} + OH^- \rightarrow \mathbf{O}_{ad} + H_2O + e^-$ Repeating steps 1a-3a	

where "M" and "ad" represent the catalyst active site at the surface of the electrode material and "**O**" represents the lattice oxygen in the crystal structure of the oxide catalyst.

1.2. Overview of low-temperature electrolyser technologies

The water electrolysis technologies operating at temperatures below 100 °C for green hydrogen production can be classified into three main technologies: alkaline water electrolysers, proton exchange membrane water electrolysers, and anion exchange membrane water electrolysers. The key features of each technology will be introduced in this section. Additionally, the bipolar membrane/interface water electrolysis technology will be discussed as well. The advantages and drawbacks of all these water electrolysis systems are summarised in Table 3.

1.2.1. Alkaline water electrolysers

Alkaline water electrolysis is the most mature and commercially viable water electrolysis technology for green hydrogen production because non-precious materials (e.g. Ni and Fe) can be used in alkaline water electrolysers as anode catalysts, reducing the costs of installing this type of electrolysers. Alkaline water electrolysers have an extensive history of usage in the chlor-alkali process to produce mainly chlorine gas and NaOH and hydrogen gas as a by-product [24]. Alkaline water electrolysers usually work at an operational temperature range of 50−80 °C and at pressures of up to 30 bar [25]. In a typical alkaline water electrolyser (Figure 5), two metallic electrodes (mostly Ni-based electrodes [26]) are submerged in a concentrated alkaline solution electrolyte (typically 30 wt% KOH solution). The electrodes are separated by the liquid electrolyte (giving a cell with a "finite gap" between the electrodes), in which sits a diaphragm (e.g. Zirfon Perl) allowing water and OH^- permeation and limiting the crossover of the gases evolved during the water electrolysis. As above-mentioned, under alkaline conditions, water is reduced at the cathode, generating OH^- and hydrogen gas (equation 18). The OH^- ions then move through the diaphragm towards the anode electrode, whereat they are oxidised to produce oxygen gas, water, and electrons (equation 19) [27].

$$\text{Cathode: } 4H_2O\ (l) + 4e^- \rightarrow 2H_2\ (g) + 4OH^- \qquad E^o = -0.826 \text{ V vs. SHE} \qquad (18)$$

$$\text{Anode: } 4OH^-\ (aq) \rightarrow O_2\ (g) + 2H_2O\ (l) + 4e^- \qquad E^o = +0.404 \text{ V vs. SHE} \qquad (19)$$

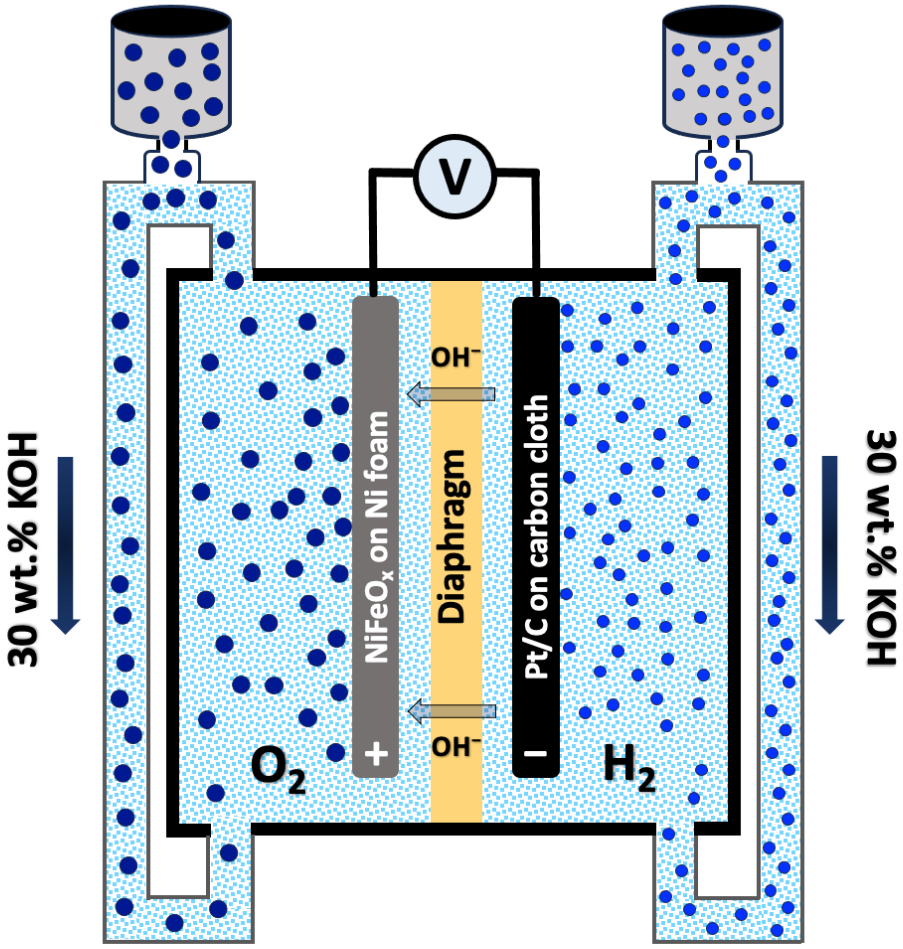

Figure 5: Schematic illustrations of typical finite-gap alkaline water electrolyser. Reprinted (adapted) with permission from [28]. Copyright 2024 Elsevier.

The diaphragm separator is a vital component of alkaline water electrolysers, allowing the permeation of hydroxide ions and water molecules. Over an extended period, asbestos-based diaphragms have been used in alkaline water electrolysers until being banned in the mid-1970s due to the health-related issues arising from the use of asbestos [23]. Recently, Zirfon diaphragm (a porous composite separator made of polysulfone and zirconia nanoparticles) is the mostly widely used separator in the market due to its low hydrogen crossover and high ionic conductivity [25,29]. In industrial alkaline water electrolysers, Pt/C (Pt anchored on mesoporous carbon support) is the benchmark hydrogen evolution reaction electrocatalyst due to its superior activity and stability [30–33]. For the oxygen evolution reaction, Ni-based oxide electrocatalysts (e.g. $NiFe_2O_4$) are commonly used due to their activity, stability, and low cost [7,27,34].

1.2.2. Proton exchange membrane water electrolysers

Proton exchange membrane water electrolysers use deionised water and feature a compact design with two liquid/gas diffusion layers acting as the anode and cathode electrodes, separated by a polymer electrolyte (e.g. Nafion). There is no gap between the electrodes and the solid electrolyte (all of which are pressed tightly together between two current collectors), and so proton exchange membrane electrolysers are "zero-gap" devices (Figure 6), ensuring minimal internal resistance within the electrolyser itself [35,36].

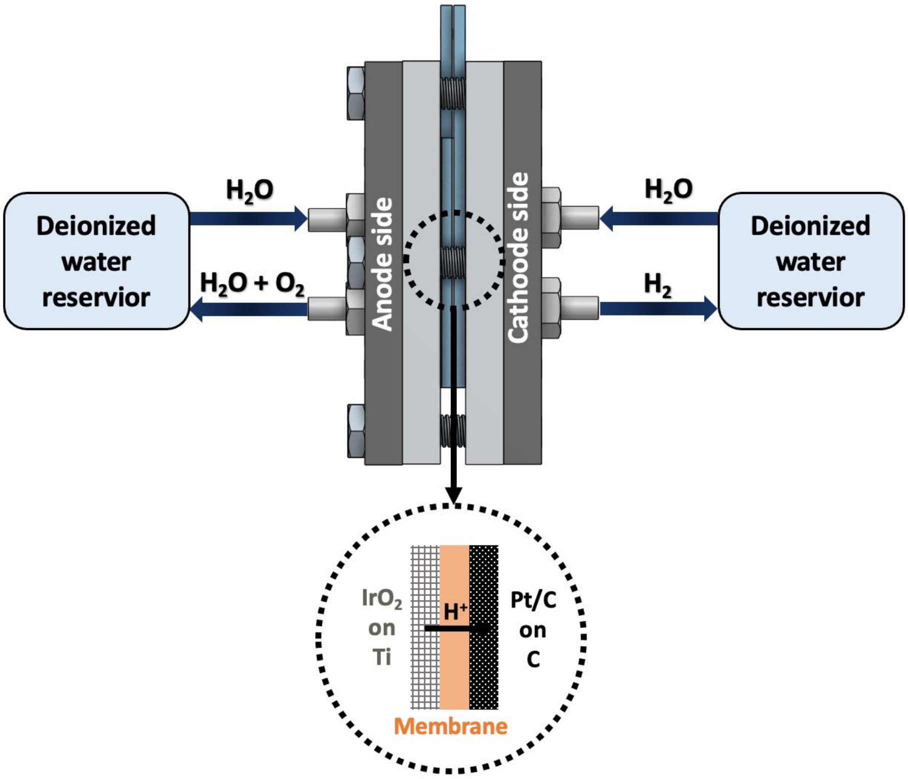

Figure 6: *Schematic illustrations of a typical zero-gap proton exchange membrane electrolyser. Reprinted (adapted) with permission from [28]. Copyright 2024 Elsevier.*

In this set-up, water electrolysis occurs under acidic conditions, wherein water is oxidised at the anode, producing oxygen, protons, and electrons (equation 20). The protons then permeate through a cationic exchange membrane to the cathode, whereat protons are reduced by electrons flowing round the external circuit to produce hydrogen (equation 21) [34].

Anode: $2H_2O \rightarrow O_2 + 4e^- + 4H^+$ $E^o = 1.23$ V vs. SHE (20)

Cathode: $4e^- + 4H^+ \rightarrow 2H_2$ $E^o = 0$ V vs. SHE (21)

The reactions summarised by equations 20 and 21 are kinetically sluggish, requiring multiple electron and proton transfers [35]. Introducing oxygen and hydrogen evolution electrocatalysts is therefore crucial for overcoming the kinetic limitations of these processes. The state-of-art electrocatalysts employed in proton exchange membrane water electrolysers are IrO_2 and RuO_2 for the oxygen evolution reaction and Pt/C for the hydrogen evolution reaction, due to their high catalytic activity and stability under acidic conditions [36,37]. Both IrO_2 and RuO_2 display high conductivity, attributed to a minimal difference in electronegativity between the oxygen (3.44) and Ir (2.2) and Ru (2.3) metals, resulting in the absence of a band gap [38]. These metal oxides can achieve strong binding to hydroxyl (HO_{ad}), a rate-determining reaction intermediate formed during the oxygen evolution reaction, with weak binding to oxygen, reducing the oxygen evolution reaction overpotential. A fundamental principle framing the design of intrinsically active electrocatalysts is the Sabatier principle, stating that an ideal catalytic activity is obtained when the binding energy of a reaction intermediate to the catalyst surface is neither too weak nor too strong [41]. A quantitative illustration of the Sabatier principle for hydrogen evolution reaction catalysts is the volcano plot, firstly recorded for metals by Trasatti in the 1970s [42]. The volcano plot (Figure 7) correlates the exchange current density (a measure of the intrinsic activity of a catalyst) to the binding energy (i.e. the Gibbs's free energy of hydrogen adsorption on the catalytic surface, ΔG_H). A higher positive value of ΔG_H signifies too weak hydrogen adsorption on the catalyst surface, impeding the formation of stable intermediates (Volmer step), whereas a higher negative ΔG_H indicates too strong hydrogen adsorption, limiting the H_2-releasing step (Heyrovsky or Tafel steps) from the catalytic surface [18]. In a seminal study conducted by Nørskov and co-workers [43], ΔG_H values for various metals were computationally-calculated and presented in a volcano plot, correlating these ΔG_H values with measured exchange current densities for the same metals. According to the Sabatier principle and volcano plot (Figure 7), Pt is the optimal catalyst for the hydrogen evolution reaction, at least under acid conditions, due to the thermoneutrality of H atom adsorption on the Pt surface (i.e. intermediate metal-H bond strength, facilitating the adsorption of H and desorption of H_2).

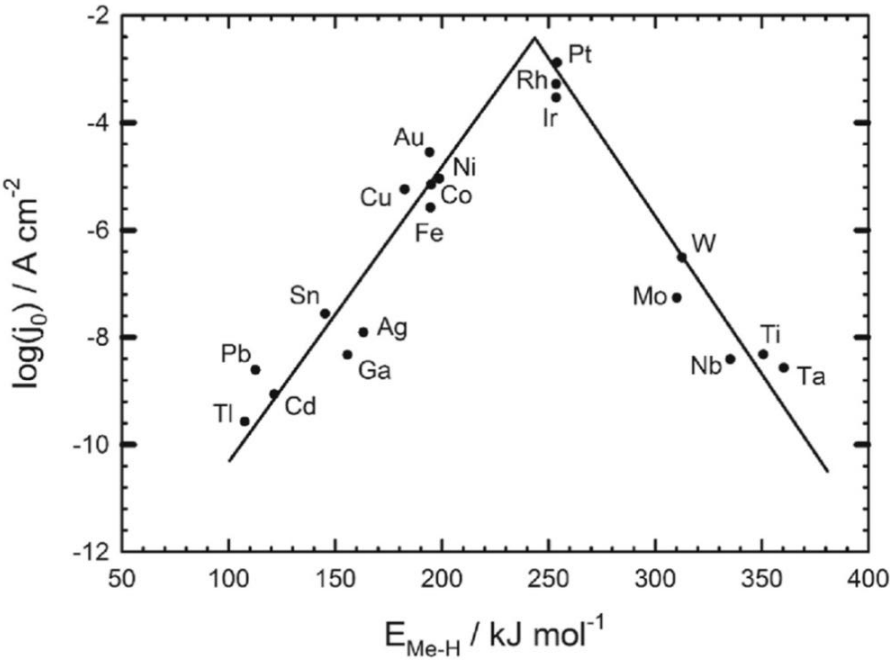

Figure 7: *A volcano plot of the hydrogen evolution reaction obtained from experimental current density results and computationally-calculated metal-H binding energies (i.e. Gibbs's free energy of hydrogen adsorption,* ΔG_H*). Pt is almost at the apex of this plot, suggesting it has optimal catalytic activity compared to other metals [44]. Reprinted with permission from [45]. Copyright 2021 Elsevier.*

1.2.3. Anion exchange membrane water electrolysers

Anion exchange membrane water electrolysis was first reported in 2011 [46], and these electrolysers resemble proton exchange membrane water electrolysers inasmuch as they consist of anode and cathode electrodes separated by a polymer exchange membrane serving as a solid electrolyte (Figure 8), providing a zero-gap configuration. The key difference lies in the fact that in anion exchange membrane water electrolysis, the membrane conducts OH^- ions instead of protons.

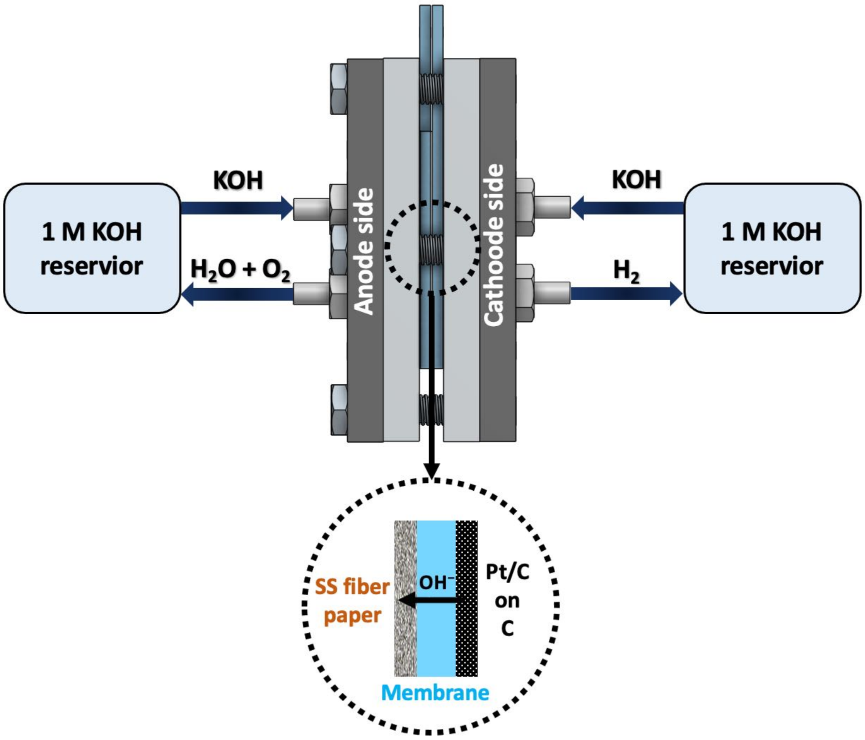

Figure 8: *Schematic illustration of a typical zero-gap anion exchange membrane electrolyser. Reprinted (adapted) with permission from [28]. Copyright 2024 Elsevier.*

1.2.3.1. Effect of the liquid electrolyte on water electrolyser performance

Hydroxide solutions, with various concentrations (0.1 M to 2.0 M) [47], are the most common liquid electrolyte circulated in anion exchange membrane water electrolysers, due to their high ionic conductivity, obtaining high current densities [48]. Despite the lower costs of sodium hydroxide (€480 t^{-1} NaOH, 2019 [49]) compared to potassium hydroxide (\$800 t^{-1} KOH [50]), the latter is more commonly used in anion exchange membrane water electrolysers as a liquid electrolyte. This is due to the higher ionic conductivity [51] and lower viscosity of KOH compared to NaOH [48]. Additionally, potassium carbonate salts are more soluble compared to sodium carbonate salts [49], mitigating the issue of precipitation arisen from the reaction with CO_2. However, there are hazards and costs associated with operating anion exchange membrane water electrolysers by using alkaline solutions, demanding implementing safety regulations and frequent maintenance. Additionally, using hydroxide solutions can lead to fouling issues in or near the membrane, mainly arising from the cationic poisoning of the membrane [50] and bicarbonate salt formation near the membrane-catalyst interface, reducing the electrolyser performance [51,52]. Thus, recently, operating anion exchange membrane water electrolysers using deionised water has been introduced to overcome the problems related to hydroxide solution use in anion exchange membrane water electrolysers. Operating anion exchange membrane water electrolysers using deionised water is 30 times cheaper compared to using alkaline solutions, with lower maintenance costs and alkaline solution disposal [42]. Nevertheless, despite the economical and operational advantages of the deionised water-circulated anion exchange membrane water electrolysis systems, these systems suffer mainly from low ionic conductivity, leading to high ohmic resistance [42]. Moreover, Ni-based anodes are prone to degradation, due to the instability of Ni-based catalysts at pH below 9 [48]. In addition, the triple-phase boundary, which is the interface where a catalyst, an ionic-conducting electrolyte, and reactants (e.g. H^+ or OH^-) come into contact [57], enabling electrochemical reactions to occur, is prone to degradation as well.

In alkaline solution-circulated configurations, the transport of hydroxide ions from the electrolyte to the electrode surface occurs through multiple pathways provided by the additional electrochemical interfaces, generated by the liquid electrolyte, with the catalyst surface [58]. In contrast, in the deionised water-circulated configuration, the transport is largely limited to that through the ionomer located amongst the membrane and catalyst surface (Figure 9) [46].

Therefore, any possible distancing between the catalyst active sites and membrane, caused by the triple-phase boundary degradation, does increase the ohmic resistance, leading to decreased reaction kinetics [58]. The triple-phase boundary degradation might occur due to changes in the morphology of the catalyst, causing a loss of contact between the catalyst and ionomer [59]. To address this issue, it is recommended to focus on enhancing the contact between the catalyst, ionomer, and membrane by developing novel catalysts that are conducive and highly stable under neutral/near-neutral conditions [46].

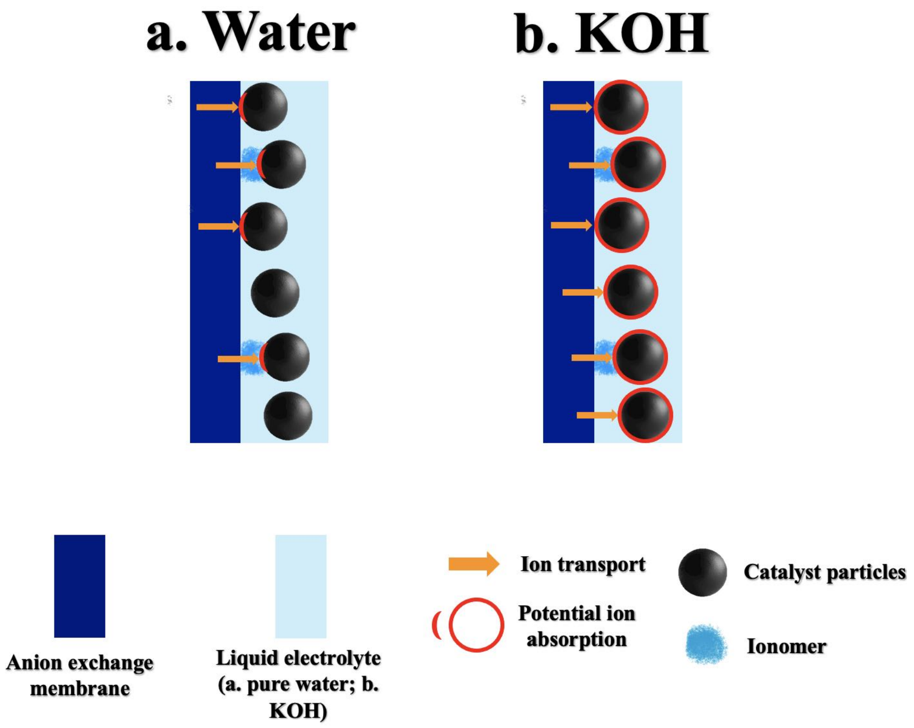

Figure 9: *Ion transport pathways through the membrane to adsorb at the catalyst surface in anion exchange membrane water electrolysis by using* ***a****. pure water or* ***b.*** *KOH as a liquid electrolyte.*

1.2.4. Bipolar membrane water electrolysers

In all alkaline and proton and anion exchange membrane electrolysis technologies, the membranes/separators do not permit a bulk pH gradient to be maintained across the cell. Consequently, the pH in the anode chamber can be assumed to be the same as in the cathode chamber for most purposes. In contrast, bipolar membrane water electrolysis allows a large pH gradient to be maintained across the electrolyser, so that the anode and cathode processes can run at completely different pH. It is the nature of the bipolar membrane that allows this. A bipolar membrane consists of two ion-exchange polymers: an anion exchange layer composed of anionic (e.g. quaternary ammonium-bearing) headgroups and a cation exchange layer composed of cationic (e.g. sulfonic acid-bearing) headgroups. The anion exchange layer allows the permeation of OH^- ions, whilst the cation exchange layer allows the permeation of H^+, with these two ions being generated by the water dissociation process taking place at the interface between the two ion-exchange layers (Figure 10) [60]. This interfacial region located between two ion exchange layers is known as the bipolar junction or bipolar interface, with a thickness much lower than 0.1 µm, as shown in scanning electron microscopy images of a commercial bipolar membrane (Figure 11) [61].

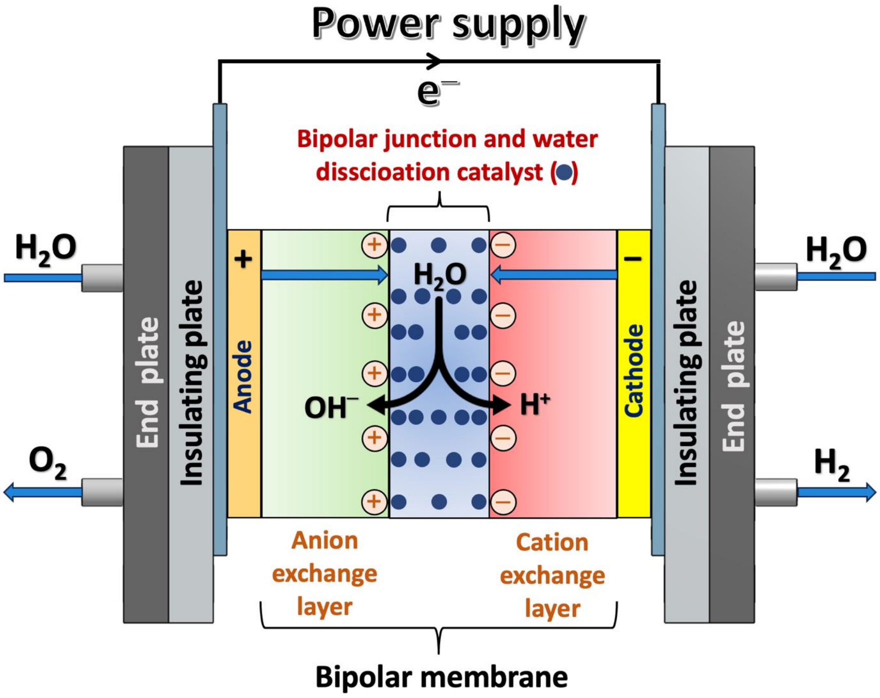

Figure 10: *Schematic of a zero-gap configuration bipolar membrane water electrolyser, illustrating the operating principles of a bipolar membrane under applied potential, where the water fed to the electrolyser is firstly dissociated at the bipolar junction into* OH^- *and* H^+. *A water dissociation catalyst (blue circles) can be incorporated at the bipolar junction to facilitate the water dissociation process. Afterwards, the* OH^- *and* H^+ *permeate through the anion and cation exchange layers, migrating to the anode and cathode, where* O_2 *and* H_2 *are formed, respectively. Reprinted (adapted) with permission from [28]. Copyright 2024 Elsevier.*

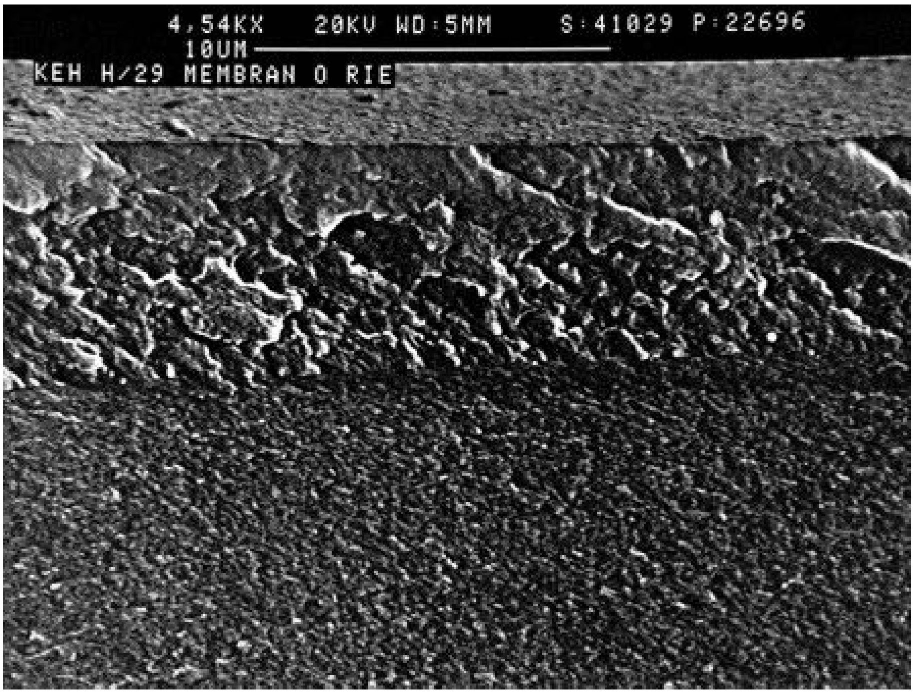

Figure 11: *Scanning electron micrograph of a bipolar membrane, showing a thin bipolar interface layer between the two ion exchange layers. Reprinted with permission from [61]. Copyright 1997 Elsevier.*

As the charge carriers are generated in the middle of the membrane and then migrate in opposite directions depending on their charge, bipolar membranes allow the cationic (cathode) side of the cell to be highly acidic, whilst the anionic (anode) side can be highly basic. This extreme pH gradient presents opportunities for optimising the types of catalysts used on each side of the electrolyser. Cheap and earth-abundant oxygen evolution catalysts can be used at the anode in combination with highly-active Pt-based catalysts at the cathode, with the anode and cathode electrocatalysts each operating under the pH regime in which they work best [62].

In bipolar membrane water electrolysis, the hydrogen evolution reaction has a minimum theoretical onset potential of 0 V vs. SHE (at pH = 0) and the oxygen evolution reaction's onset potential is +0.404 V vs. SHE (at pH = 14). However, the pH gradient across the cell also imposes a voltage penalty, equating to 59 mV per pH unit, representing an additional potential of 0.826 V (at 25 °C) at the bipolar junction (equation 22) [62–64].

$$E_{pH} = 2.3\,\frac{RT}{nF}\,\Delta pH = 0.059\ V \times \Delta pH = 0.826\ V\ (\text{when}\ \Delta pH\ \text{is}\ 14) \qquad (22)$$

1.2.4.1. Water dissociation process mechanisms

In bipolar membrane water electrolysers, the protons and hydroxide ions generated from water dissociation at the bipolar junction migrate towards the negatively charged cathode and the positively charged anode, respectively [63]. Water dissociation into protons and hydroxide ions is a complex process that can be explained by two main theoretical mechanisms (Figure 12). The Second Wien Effect describes the influence of strong electric fields on weak electrolytes (e.g. water), producing an increase in ionic mobility/conductivity at high electric fields [65–67]. In bipolar membrane water electrolysis, the Second Wien Effect refers to the phenomenon whereby applying a strong electric field at the bipolar junction enhances the water dissociation rate [68]. Nevertheless, assuming that the Second Wien Effect is the only contributor to water dissociation is insufficient to completely describe this process at the bipolar junction, as the potentials required for water dissociation at this junction are larger than the Second Wien Effect alone predicts [61]. Another proposed mechanism for water dissociation is the protonation-deprotonation reaction between water molecules and the anionic and cationic exchange layer headgroups in the bipolar membrane (Scheme 1) [69–71]. In reaction pathway a in Scheme 1, the sulfonic acid headgroup protonates a water molecule, and then the resulting sulfonate anion deprotonates a second water molecule, while in pathway b, a tertiary amine headgroup acts as a weak base, first deprotonating one water molecule and then protonating a second water molecule. Moreover, Strathmann *et al.* [61] devised a model combining the two theories to explain water dissociation. In their model, at a specific limiting current, obtained under a weak electric field, all salt ions are depleted from the bipolar junction. This depletion causes an elevation in the resistance across the junction, generating a high electric field (Second Wien Effect mechanism) exceeding the limiting current density (which gives the so-called over-limiting current density); thus, accelerating the water dissociation rate. The catalytic activity of the ion exchange layers' headgroups in the bipolar membrane supports this process (protonation-deprotonation mechanism).

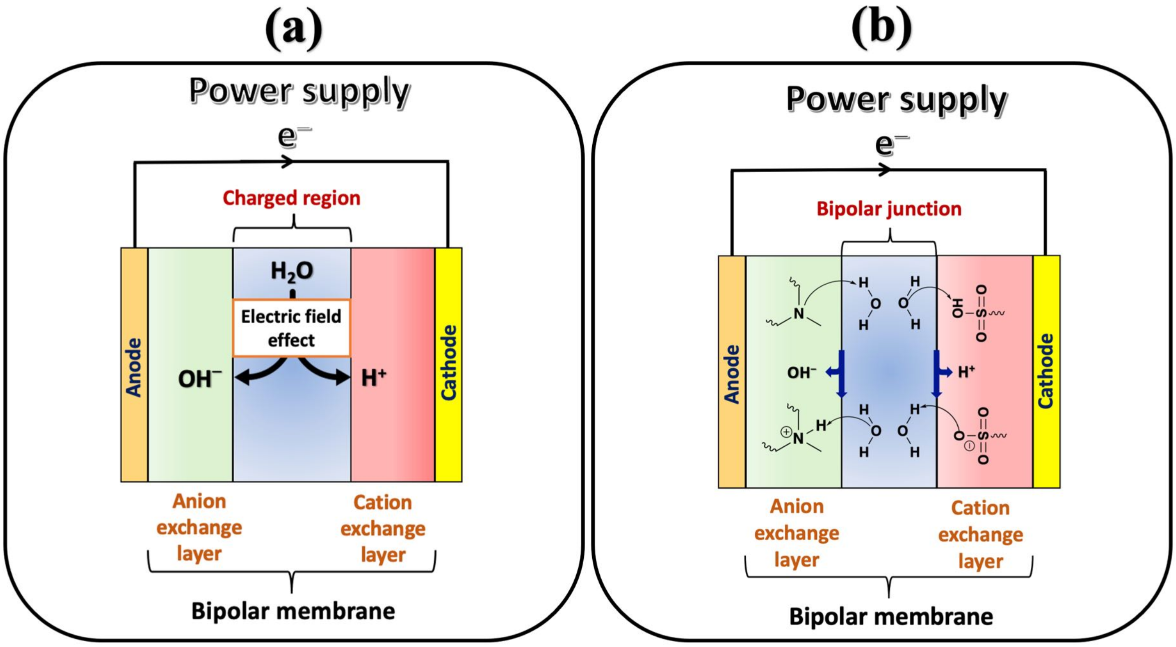

Figure 12: *Schematic of the two main mechanisms for water dissociation at a bipolar membrane junction within a bipolar membrane: (a) water dissociation under a strong electric field (Second Wien Effect mechanism); (b) the reaction of water molecules with cationic and anionic functional headgroups (protonation-deprotonation reaction mechanism). Reprinted (adapted) with permission from [28]. Copyright 2024 Elsevier.*

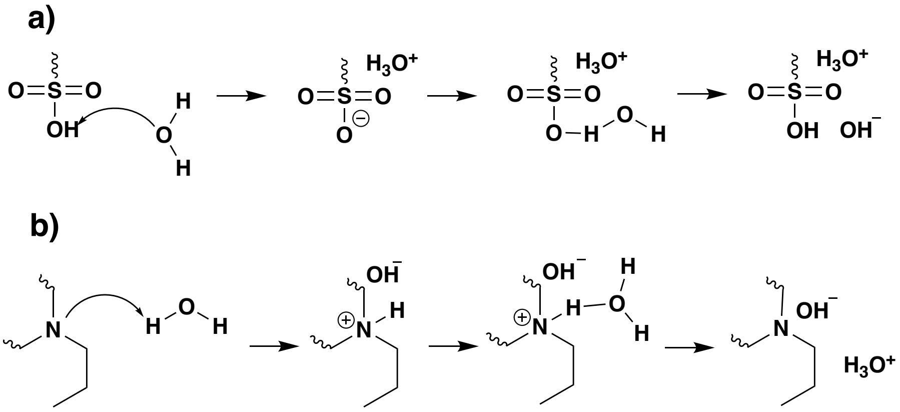

Scheme 1: *The (a) weak-acid (sulfonic functional headgroups) and (b) weak-base (amine functional headgroups) in a bipolar membrane can catalyse the water dissociation process through the protonation-deprotonation reaction mechanism. Reprinted (adapted) with permission from [28]*

1.2.4.2. Water dissociation catalysts

The introduction of water dissociation catalysts at the bipolar junction by placing a catalytic (bi)layer between the anion and cation exchange layers (Figure 13) promotes the water dissociation process by minimising the water dissociation overpotential [72].

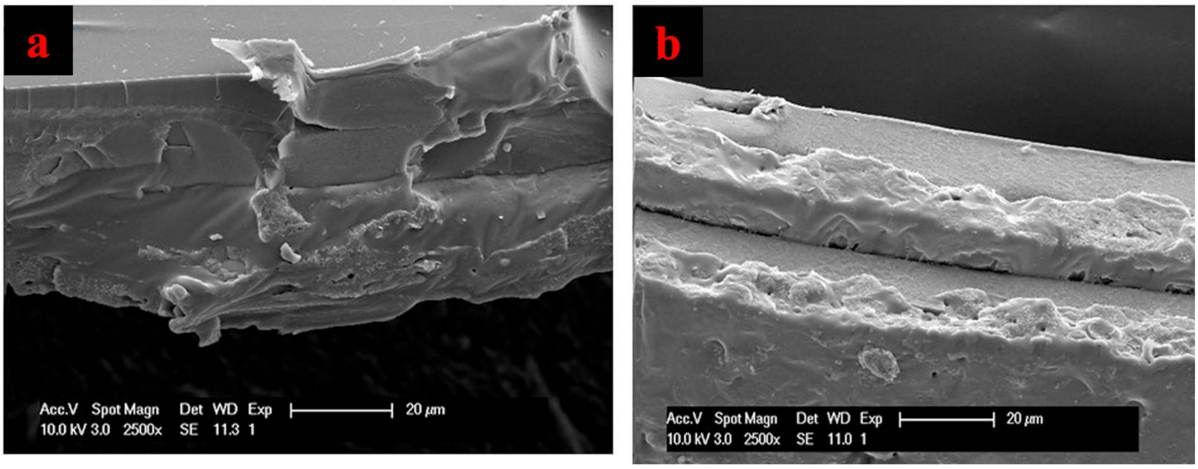

Figure 13: *Scanning electron microscope cross-section images of a bipolar membrane (a) without and (b) with a MoS_2 nanosheet water dissociation catalyst at the bipolar junction. Reprinted (adapted) with permission from [73]. Copyright 2018 Elsevier.*

A diverse range of materials can function as water dissociation catalysts. These include metal oxides (e.g. NiO and SiO_2) [74], nanomaterials (e.g. MoS_2) [73], and oxygen-containing graphitic materials (e.g. graphene oxide) [72]. However, it is essential to employ a catalyst that is highly stable in both acidic and alkaline conditions, since low-pH and high-pH conditions might be generated at the bipolar junction as the water dissociation reaction produces OH^- and H^+ [75]. For example, NiO is susceptible to dissolution at the cationic exchange layer [74]. Therefore, it is advisable to integrate stable water dissociation catalysts capable of functioning across a wide pH range, such as TiO_2 and IrO_2.

1.2.4.3. Bipolar membrane water electrolysis challenges

The total operational potential for bipolar membrane water electrolysis is influenced by a range of factors, as depicted in equation 23 [63,76,77].

$$E_{operational} = \eta_{anode} + \eta_{cathode} + \eta_{water\ dissociation} + E_M + E_{pH} + iR_{cell} \tag{23}$$

where the operational potential ($E_{operational}$) in bipolar membrane water electrolysis includes overpotentials for the anodic (η_{anode}) and cathodic ($\eta_{cathode}$) reactions, pH gradient overpotential (E_{pH}), ohmic resistance (iR_{cell}), membrane resistance (E_M), and overpotential for the water dissociation process taking place at the bipolar junction ($\eta_{water\ dissociation}$) [77].

Furthermore, insufficient water transport through the anion and cation exchange layers into the bipolar junction might lead to membrane dryness and poor water dissociation, due to limited availability of water molecules [78]. In addition, as bipolar membranes exhibit imperfect permselectivity in practice, extraneous ions (e.g. Na^+ and Cl^-) can enter the bipolar junction (so-called ion crossover), disturbing the pH gradient across the bipolar membrane over extended operation [79]. This ion crossover reduces the efficiency of the electrolyser because a portion of the charge is carried by this leakage of salt ions instead of being used for water dissociation [78,80]. Thus, operating an electrolyser containing a bipolar membrane generally entails higher complexity and expense compared to operating an electrolyser equipped with monopolar ion exchange membrane [81]. Moreover, adding a catalyst at the bipolar interface is crucial, as previously mentioned. However, the production of a bipolar membrane incorporating a water dissociation catalyst is complex, and there are currently no commercially accessible bipolar membranes featuring such a catalyst [82], hindering the advancement of research in this area.

***Table 3**: The advantages and drawbacks of different water electrolysers [35,48,83–85].*

	Finite-gap alkaline water electrolysers	**Anion exchange membrane water electrolysers**	**Proton exchange membrane water electrolysers**	**Zero-gap bipolar membrane water electrolysers**
Advantages	Historical precedence Affordable components Durable porous diaphragm at elevated temperatures	High H_2 purity Affordable components Least corrosive conditions High operational pressure	High H_2 purity High current density values Highly stable membranes	Can deploy oxygen and hydrogen evolution electrocatalysts in their most kinetically favourable pH conditions
Drawbacks	Low current density values Highly basic conditions Cross-over of gases Leakage issues	Intermediate current density values Membrane degradation Low technology readiness level	Highly corrosive conditions Expensive components	Bipolar membrane manufacturing complexity High operational potential Low technology readiness level

1.3. Key components of membrane-electrode assembly in zero-gap water electrolysers

The membrane electrode assembly (MEA), typically sandwiched between two flow field plates, also known as bipolar plates, is the core component of zero-gap water electrolysers, serving a vital role in determining the overall efficiency and performance of an electrolyser. A typical MEA consists of a solid polymer electrolyte membrane sandwiched by two liquid–gas diffusion layers, also known as porous transport layers, coated with anode and cathode catalyst layers (Figure 14) [86].

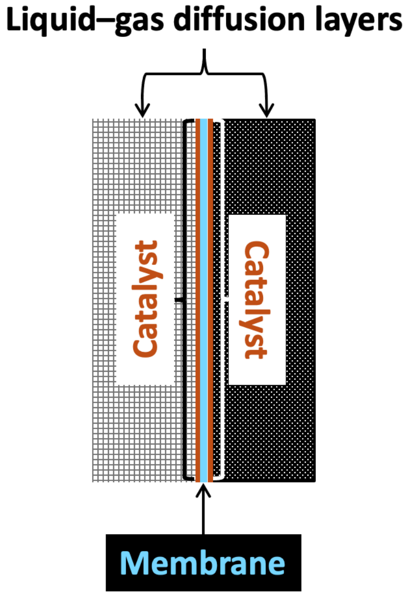

__Figure 14:__ A schematic illustration of a typical membrane electrode assembly (MEA) composed of an ion exchange membrane sandwiched between two liquid–gas diffusion layers coated with catalysts layers.

1.3.1. Liquid–gas diffusion layers

The liquid-gas diffusion layers, also known as porous transport layers (PTLs), is a key component in membrane electrode assemblies in water electrolysers. These layers facilitate the transport of liquid reactants (e.g. water) and gaseous products (e.g. hydrogen and oxygen gases generated at the cathode and anode, respectively). The PTLs must be electrically conductive, allowing the transport of electrons between the catalyst layers and the bipolar plates, as well as exhibiting high thermal and mechanical robustness, along with chemical stability under harsh operating environments (strongly acidic or alkaline media) [87].

On the cathode side, carbon-based PTLs are widely used either in proton [87] or anion [48] exchange membrane water electrolysers, due to their lower production compared to metallic-based PTLs [88], as well as their chemical stability under the reducing hydrogen atmosphere and low potential required at the cathode [87]. The carbon-based PTLs are commonly used in the form of carbon cloth or carbon paper. The structure of carbon cloth consists of interwoven bundles of carbon fibres organised in a uniform pattern, while in carbon papers, the fibres are stiff, straight, and randomly organised [21,89]. Moreover, carbon-based PTLs are often fabricated with a microporous layer (MPL), typically a few microns thick, composed of carbon particles and hydrophobic agents, such as polytetrafluoroethylene (PTFE) [90]. Incorporating an MPL reduces the pore size on the surface of carbon-based PTLs (Figure 15), resulting in an improved interfacial contact with the catalyst layer, leading to a decrease in the interfacial contact resistance, and an increase in catalyst utilisation [87,91]. Other commonly used materials for PTLs in anion exchange membrane water electrolysers are Ni-based materials and stainless steel [48,87].

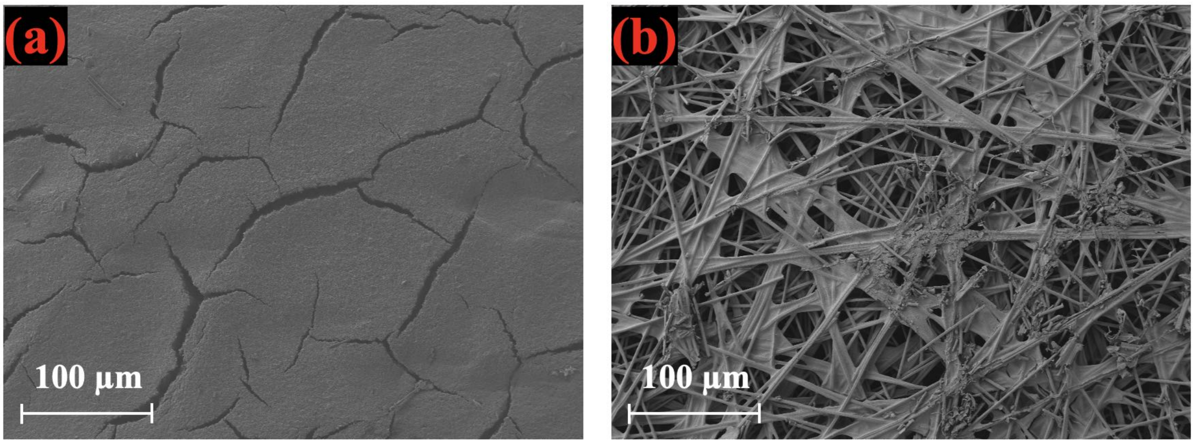

Figure 15: *Scanning electron microscope images for the top surface of two commercially available carbon paper liquid–gas diffusion layers: (a) Sigracet carbon paper (with a microporous layer) and (b) Toray carbon paper (without a microporous layer). The surface of the carbon paper with a microporous layer (MPL) has smaller pores compared to the surface of the carbon paper without an MPL.*

On the anode side, Ti-based PTLs (e.g. Ti fibre felt, Figure 16) with a Pt coating represent the state-of-the-art PLTs used in proton exchange membrane water electrolysers, owing to their high resistance to acid corrosion [87]. Titanium passivates at anodic potentials, while the Pt coating provides the necessary electrical conductivity for long-term operation, ensuring higher performance stability compared to uncoated Ti-based PTLs, albeit at the expense of increased cost [92]. In contrast, Ni-based materials are the standard choice for anion exchange membrane water electrolysers, due to the less harsh alkaline conditions. Stainless steel is another material that can be used in alkaline environment, since it passivates at anodic potentials, albeit at the expense of decreased electrical conductivity [36,48,93].

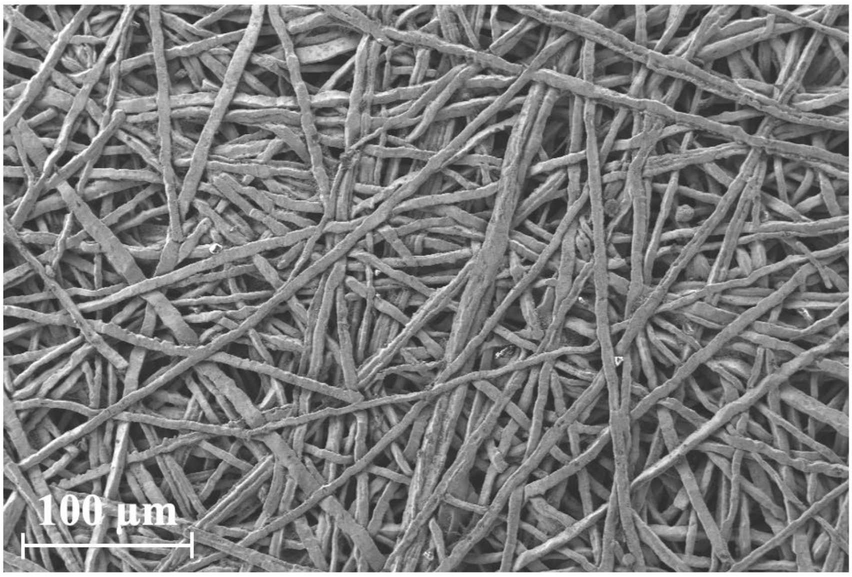

Figure 16: *Scanning electron microscope images for the top surface of a typical uncoated Ti fibre felt PTL.*

As discussed above, to improve the performance stability of water electrolysers, PTLs should be developed to show optimal mechanical robustness, thermal and chemical stability, porosity, electrical conductivity, and high surface area. These properties contribute to form an effective triple-phase boundary, where a catalyst layer, reactants, and an ion-conducting electrolyte come into contact, facilitating efficient electrons and ions transport and rapid removal of generated gases, maintaining accessible active catalyst sites [57].

1.3.2. Ion exchange membranes

Ion exchange membranes function as the electrolyte material in zero-gap water electrolysers while separating the anode and cathode sides. These membranes typically consist of a polymer backbone with anchored functional headgroups, negatively charged in proton exchange membranes and positively charged in anion exchange membranes, enabling the transport of protons and hydroxide ions, respectively.

Perfluorosulfonic acid membranes are the state-of-the-art polymer membranes used in proton exchange membrane water electrolysers. The structure of these membranes consists of a Teflon backbone and hydrophilic cationic sulfonated functional headgroups, conducting protons mainly through the Grotthuss and Vehicle mechanisms [94,95]. Both mechanisms can always coexist in the same system [96]. In hydrated membrane state, protons transported via the Grotthuss mechanism, where a proton hops from a hydronium ion (H_3O^+) to a neighbouring water molecule through hydrogen bonding, continuing along a continuous hydrogen-bond network formed by water molecules. In contrast, in the Vehicle mechanism, no proton exchange takes place between the hydronium ion and water molecule during the proton transport process. Rather, the protons are transferred in a hydrated form, driven by an electric potential difference (i.e. hydronium ion migration) [97].

Similarly, OH^- ions transport via the Grotthuss and Vehicle mechanisms through ion transport channels within the structure of anion exchange membranes. The channels within anion exchange membranes typically have anionic functional headgroups (e.g. quaternary ammonium group) tethered to the polymer backbone, facilitating the movement OH^- ions. Moreover, because of the coulombic interactions between OH^- ions and the cationic functional headgroups, OH^- ions might transport via the surface site hopping mechanism, where a OH^- ion attaches to a cationic site and then hops to the next available cationic side, continuing the hopping process across the ion transport channel [97–99].

1.4. Membrane electrode assembly preparation approaches

There are two main fabrication methods for membrane electrode assembly: catalyst-coated substrate (CCS) and catalyst-coated membrane (CCM) approaches. In the CCS approach, a catalyst layer is deposited onto a substrate (i.e. a PTL), followed by hot-pressing it with a membrane to form the CCS assembly. Several deposition techniques are adopted for fabrication the CCS assembly, including spray coating [100], magnetron sputtering [101], electrodeposition [102], and screen printing [103]. On the other hand, in the CCM approach, the catalyst layer is deposited directly, typically by spraying [48], onto the membrane surface.

Despite the fabrication simplicity of the CCS approach and the strong attachment stability of the catalyst layer onto the substrate surface, this approach primarily suffers from insufficient interfacial contact between the membrane and the catalyst layer, reducing the catalyst utilisation [21]. In contrast, the CCM approach is usually adopted for higher catalyst utilisation and stronger adhesion between the membrane the catalyst layers [104], enabling lower catalyst loading mass. Nevertheless, this approach can lead to membrane wrinkling or expansion during catalyst deposition step [105], and its more complex and precision-dependent catalyst deposition process compared to CCS may increase manufacturing costs [106].

1.5. Key evaluation parameters of electrocatalysts for water electrolysis

As above-mentioned, stable and active catalysts are required to lower the kinetic energy barriers of the sluggish kinetics of hydrogen and oxygen evolution reactions. Thus, numerous catalysts have been developed and employed in industrial water electrolysers. Despite the lack of a standardised protocol and method for evaluating and comparing oxygen and hydrogen evolution reactions catalysts [45], several key evaluation criteria have been reported in the literature, mainly overpotential, exchange current density, Tafel slope, specific activity, turnover frequency, Faradaic efficiency, and stability.

1.5.1. Overpotential, exchange current density (j_o), and Tafel slope

The thermodynamic potential (i.e. equilibrium potential) at standard conditions for the hydrogen evolution reaction is 0 V vs. SHE and for the oxygen evolution reaction is 1.23 V vs. SHE, as mentioned previously. However, in practice, additional potentials, decreasing the electrolyser efficiency, are required to drive the water electrolysis process. The overpotentials required in an electrolyser can be categorised into three main overpotentials: activation, ohmic, and concentration overpotentials, shaping a polarisation curve, a plot displaying the relationship between applied potential and current density, illustrating the current density output over a range of applied potentials [107]. A typical polarisation curve of water electrolysis is shown in Figure 17. At low current densities (~ 5 mA cm^{-2}), the activation overpotential occurs because of the kinetic barriers of the anode and cathode reactions at the electrode/electrolyte interfaces [108,109]. In contrast, at high current densities (> 800 mA cm^{-2}), concentration overpotential arises mainly from limited gas diffusion, where accumulated O_2 and H_2 bubbles block catalyst sites, reducing reaction kinetics [110–112]. In addition, at moderate current densities, ohmic overpotential occurs mainly due to the ionic resistance of the membrane and the electronic resistances of the electrolyser components and the contact resistance between these components [111].

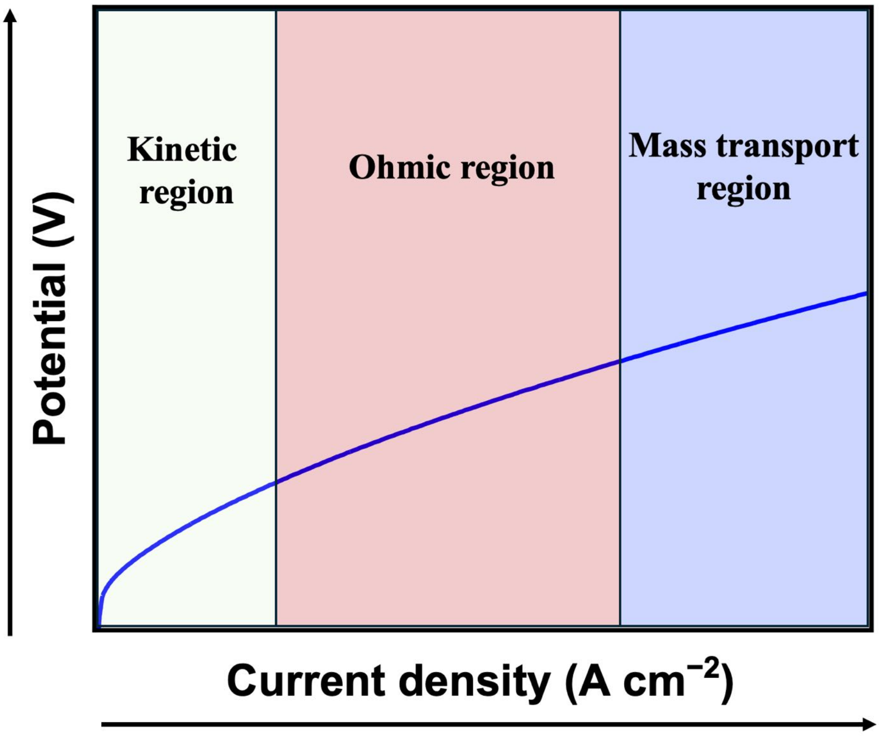

Figure 17: *Schematic of a typical polarisation curve of water electrolysis shaped by three major overpotentials: activation (in the kinetic region), ohmic (in the ohmic region), and concentration (in the mass transport region) overpotentials.*

The total overpotential can be calculated by taking the difference between the equilibrium potential and the actual operational potential required to obtain a particular current density, the most reported current density being 10 mA cm^{-2} [32], as shown in equation 24.

$$\eta = E_{measured} - E_{eq} \qquad (24)$$

where η represents the overpotential and $E_{measured}$ and E_{eq} represent the total actual operational and equilibrium potentials, respectively.

In terms of comparing the intrinsic catalytic activity of different catalysts accurately, an ohmic or iR drop correction should be applied to the activation overpotential, whereby the ohmic overpotential is excluded from the operational potential, as described in equation 25 [27].

$$\eta = (E_{measured} - iR_{cell}) - E_{eq} \qquad (25)$$

where η represents the overpotential, $E_{measured}$ and E_{eq} are the total actual and equilibrium potentials, respectively, i is the current flow through the circuit, and R_{cell} is the total ohmic resistance of the system, including the resistance of the membrane, electrodes, gaseous bubbles, and the connection wires [113].

The exchange current density (j_o) is a crucial kinetic parameter for evaluating the activity of a catalyst, reflecting the intrinsic rates of electron transfer between an analyte and the electrode at equilibrium (i.e. when anodic and cathodic reactions occur at equal rates). It is defined as the current density achieved at equilibrium potential, assuming η equals zero [27]. A higher exchange current density reflects faster reaction rate, indicating higher catalyst activity [114].

A Tafel plot is another important analytical method for investigating the reaction rate and mechanism. It can be used to relate the logarithmic overpotential and current density and measure the exchange current density, whereby the x-intercept value depicts the exchange current density, as demonstrated by equation 26.

$$\eta = a + b \log j \qquad (26)$$

where b is the Tafel slope, a is the x-intercept (where $\eta = 0$), and j is the current density.

The Tafel slope is a widely used kinetic parameter representing the potential required (in mV) to increase current by 10-fold. It is typically expressed in mV per decade (mV dec^{-1}). A smaller Tafel slope indicates higher catalyst activity, since smaller overpotential is required to achieve higher current density [115]. The Tafel slope can be obtained from potentiodynamic techniques, such as linear sweep voltammetry and cyclic voltammetry. Nevertheless, such techniques do not allow the catalytic interface to rest at a specific potential for sufficient time to achieve a steady-state response, leading to inaccurate values of the Tafel slope and exchange current density. Therefore, for reliable values, chronoamperometry or chronopotentiometry should be used, as these are electroanalytical techniques that allow the steady-state performance of a catalyst to be probed [116].

1.5.2. Specific activity

It is common to compare the intrinsic activities of various catalysts using overpotential and Tafel slope derived from polarisation curves normalised to the geometric surface area of an electrode [117]. However, using the geometric surface area normalisation is an inaccurate approach to evaluate the intrinsic activity of a catalyst, since the overpotential and Tafel slope are catalyst loading mass-dependent parameters changing with varying mass loading. Anantharaj *et al.* confirmed the catalytic performance dependency on a catalyst's mass loading, whereby NiO was investigated as a well-studied oxygen evolution reaction catalyst in 1 M KOH using five different mass loadings [118]. The overpotential normalised to geometric electrode surface area and Tafel slope (derived from iR-compensated polarisation curves) was influenced by the change in mass loading, whereby a reduction in overpotential and Tafel slope values was observed as mass loading increased (Figure 18). Therefore, overpotential and Tafel slope parameters obtained by geometric electrode surface area normalisation may not accurately reflect the intrinsic activities of different catalysts (but they can reflect the overall electrode performance), because this approach ignores the actual catalyst active sites.

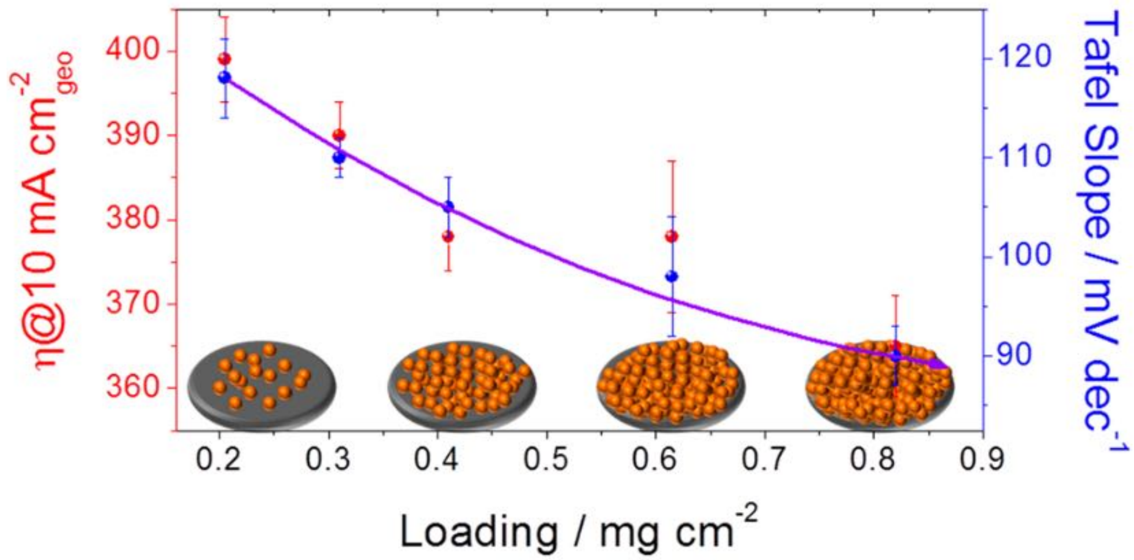

Figure 18: *A plot showing the dependency of the overpotential normalised to the geometric electrode surface area (η@10 mA* $cm^{-2}{}_{geo}$*) and Tafel slope (derived from iR-compensated polarisation curves) on a catalyst's mass loading. Reprinted with permission from [118]. Copyright [2017] American Chemical Society. https://doi.org/10.1021/acsenergylett.9b00686.*

The overpotential normalised to the electrochemical surface area (ECSA) of a catalyst, known as the specific activity, is a more reliable alternative approach for evaluating the intrinsic activity of a catalyst, measuring the number of the catalyst active sites exposed to the electrolyte. The specific activity is a mass loading-independent parameter, whereby the ECSA-normalised overpotential remains constant regardless of the catalyst mass loading used [119]. Moreover, since the Tafel slope is a mass loading-dependent parameter, it is recommended to report Tafel slopes derived from ECSA-normalised iR-compensated polarisation curves to exclude any catalyst mass loading and mass transport effects. However, optimising the mass loading of a catalyst is crucial since any mass loading beyond the surface coverage (θ) of 100% (i.e. complete monolayer coverage [120]) might lead to false interpretation. In other words, at large mass loadings ($\theta > 100\%$), an increase in charge transfer resistance arising from a partial self-masking of catalytic sites might occur [118].

1.5.3. Turnover frequency (TOF)

Turnover frequency (TOF) is another useful parameter reflecting the intrinsic activity of catalysts since it is a mass loading-independent parameter like the specific activity. It is defined as the number of products generated per catalyst site per second at a specific overpotential; it can be calculated by equation 27 [121].

$$\text{Turnover frequency (TOF)} = \frac{j \times N_A}{n \times F \times \Gamma} \qquad (27)$$

where j represents current density, N_A is the Avogadro constant, F is Faraday constant, and Γ represents the total number of catalytic active sites participating in the reaction [113].

Although this parameter is mass loading-independent, it is important to optimise the mass loading mass of a catalyst, like the specific activity, whereby the surface coverage (θ) of 100% should not be exceeded to avoid the self-masking effect [118]. The Γ value can be calculated by integrating the area under the redox peak derived from cyclic voltammetry [117]. However, it is difficult to determine the surface active sites (Γ) in the case that multiple redox peaks participate in a reaction or the redox peak is incomplete. In addition, the method used for determining Γ does vary based on the catalyst material and type employed [32]. Thus, an ideal catalyst model can be used, assuming a single-crystal catalyst with smooth surface [118,119].

1.5.4. Faradaic efficiency

Faradaic efficiency is a crucial quantitative analysis useful for investigating the selectivity for a particular product obtained from an electrochemical process. In terms of water electrolysis, it is defined as the ratio between the experimentally produced volume of hydrogen or oxygen gas and theoretically calculated volume of hydrogen or oxygen gas; it can be calculated using equation 28 [122]. If the Faradaic efficiency equals 100%, then it indicates ideal selectivity of the catalysts towards generating the product.

$$\text{Faradaic efficiency} = \frac{n \times a \times \mathrm{F}}{Q} \times 100 \qquad (28)$$

where n, a, F, and Q represent the mole number of a specified product, the number of electrons transferred based on the relevant balanced equation, the Faraday constant (96485.3 C mol^{-1}), and the total charge passed during the electrochemical process, respectively.

1.5.5. Stability

The long-term stability of catalysts is one of the most important key parameters for catalyst evaluation, especially for industrial applications. There are two main approaches to evaluate the stability of a catalyst. First, chronopotentiometry can be used, wherein a constant current density is applied for a period. The variation in the potential required to maintain the applied current density during the chronopotentiometry test is calculated, whereby the starting and end potentials are compared. Second, performing cyclic voltammetry for many cycles can be used to accelerate the degradation of the catalyst. A negligible variation over time, in both methods, indicates a stable catalyst [114,123].

In an industrial scale, testing the durability of water electrolyser devices under several thousands of hours of continuous operational conditions is required for hydrogen mass production, increasing the durability evaluation expenses of these devices [35]. Accelerated stress tests (ASTs) can be implemented to reduce the high costs associated with the lengthy conventional stability tests by accelerating the ageing processes of water electrolyser components through the adaptation of various stressors (i.e. operating parameters) during stability characterisation [35,124]. In an AST study, either a specific component of the electrolyser (e.g. a catalyst, a PTL, or a membrane) or the entire system is exposed to certain conditions accelerating the degradation process, enabling for a quicker durability evaluation [125]. Dynamic load cycling is a widely adopted technique used for investigating the durability of water electrolyser devices. In this technique, current density or potential is varied over repetitive cycles of intermittent operation to simulate the fluctuating power supply from the renewable sources (e.g. solar panels) coupled to water electrolysers, helping in understanding the degradation mechanism under different conditions [126–128]. In a study conducted by Li *et al.,* the impact of the load cycling AST was investigated by comparing two dynamic load profiles of 0 – 0.5 A cm^{-2} and 1.2 – 2 A cm^{-2} with a constant load test at 1 A cm^{-2} [129]. Each test configuration was conducted for 350 h (1035 cycles for dynamic tests) at 60 °C. The degradation rates observed were 51.4 $\mu V\ h^{-1}$ for low current density and 55.8 $\mu V\ h^{-1}$ for high current density dynamic load modes, while only 29.8 $\mu V\ h^{-1}$ was observed for constant current density load mode. The increased degradation rate for the dynamic load modes was attributed to the faster carbon support corrosion and Pt nanoparticles agglomeration at low current densities, as well as accelerated anode catalyst degradation at high current densities [130,131]. To achieve a coherent comparison among durability tests, standardised AST protocols should be adopted. For, example, EU-harmonised AST protocols for evaluating the durability of proton exchange membrane, anion exchange membrane, and alkaline water electrolysers were reported [127]. These protocols were developed through a joint effort involving industry partners and research institutions engaged in several projects funded by the Fuel Cell and Hydrogen Joint Undertaking (FCH JU).

1.6. Conclusions

As discussed in this Chapter, the production of green hydrogen through water electrolyser technologies is a promising environmentally friendly method to mitigate the carbon dioxide and other pollutants emissions. However, water electrolysis process suffers from low efficiency, mainly due to the sluggish oxygen and hydrogen evolution reactions, demanding the development of high active and robust electrocatalysts. Evaluating HER and OER catalysts (and other electrolyser components) in conventional lab-scaled three-electrode cells (e.g. H-cell) is practically insufficient, due to the lab-scaled testing conditions that do not reflect the industrial operating conditions of water electrolysers (e.g. testing the stability of a component at ≥ 1 A cm^{-2}). In a recent study, 1T′-$MoTe_2$ film was deposited on a carbon cloth support through chemical vapor deposition (CVD) and tested in a three-electrode and PEM flow single-cell configurations as an HER catalyst having the same mass loading of 0.6 mg cm^{-2} [100]. In galvanostatic electrolysis tests at 60 °C, 1T′-$MoTe_2$ achieved only 150 mA cm^{-2} at 2.0 V in the three-electrode setup compared to > 800 mA cm^{-2} achieved in the PEM electrolyser, suggesting that certain factor hindered the performance of 1T′-$MoTe_2$ in the three-electrode cell. Another work showing the discrepancy between evaluating catalysts in thee-electrode systems and zero-gap water electrolysers was conducted by Browne *et al.*, where a range of transition metal oxides were tested as OER catalysts in a three-electrode cell and an electrolyser [132]. Although the experimental results obtained by linear sweep voltammetry tests were iR corrected (eliminating the effect of ohmic resistance on performance), the OER catalysts showed different performance in the two configurations, where the same catalysts considerably underperformed in the three-electrode cell. Thus, it is crucial to evaluate the catalysts (or any other water electrolysis components) in a water electrolyser, reflecting more accurately the performance and durability of these materials under conditions more relevant (compared to the H-cell configuration) to the industrial operating conditions.

To allow more reliably and consistent evaluation of the water electrolyser materials, a standardised baseline should be developed, allowing for meaningful comparisons between various materials or operating conditions. The main part of my work is to develop and optimise an anion exchange membrane water electrolyser to be used as a testbed cell for evaluating novel water electrolyser materials, due to the absence of a universally-accepted standardised system. To facilitate the adoption of my standardised system by others, I managed to publish an open access paper, including an assemble and operation protocol in detail, and 3D drawings of the flow cell components. Additionally, several flow cells of this standardised design were mass machined by an industrial party to be distributed and used by other colleagues. Furthermore, I managed to use this flow cell design as an anion exchange membrane water electrolyser and a proton exchange membrane water electrolyser as well to evaluate and compare varied materials, including different proton exchange and anion exchange membranes. To test and compare different proton exchange membranes (Chapter 4), a standardised procedure for preparing and spraying IrO_2 ink (as the OER catalyst) was developed.

References

[1] W. Grochala, First there was hydrogen, Nat. Chem. 7 (2015) 264, https://doi.org/10.1038/nchem.2186.

[2] J. Yan, C. Zhou, Z. Rong, H. Wang, H. Li, X. Hu, Simulation of the dynamic characteristics of a PEMFC system in fluctuating operating conditions, Energies 13 (2020) 3596, https://doi.org/10.3390/en13143596.

[3] M.G. Rasul, M.A. Hazrat, M.A. Sattar, M.I. Jahirul, M.J. Shearer, The future of hydrogen: Challenges on production, storage and applications, Energy Convers. Manag. 272 (2022) 116326, https://doi.org/10.1016/j.enconman.2022.116326.

[4] D. Bessarabov, P. Millet, PEM Water Electrolysis, Eleisver, 1st ed, London, 2018, https://doi.org/10.1016/b978-0-12-811145-1.00011-3.

[5] Q. Qin, M. Oschatz, Overcoming Chemical Inertness under Ambient Conditions: A Critical View on Recent Developments in Ammonia Synthesis via Electrochemical N_2 Reduction by Asking Five Questions, ChemElectroChem 7 (2020) 878–889, https://doi.org/10.1002/celc.201901970.

[6] P.J. McHugh, A.D. Stergiou, M.D. Symes, Decoupled Electrochemical Water Splitting: From Fundamentals to Applications, Adv. Energy Mater. 10 (2020) 2002453, https://doi.org/10.1002/aenm.202002453.

[7] I. Roger, M.A. Shipman, M.D. Symes, Earth-abundant catalysts for electrochemical and photoelectrochemical water splitting, Nat. Rev. Chem. 1 (2017) 0003, https://doi.org/10.1038/s41570-016-0003.

[8] P. Cavaliere, Water Electrolysis for Hydrogen Production, 1st ed, Springer Cham, Cham, 2023, https://doi.org/10.1007/978-3-031-37780-8.

[9] T. Smolinka, H. Bergmann, J. Garche, M. Kusnezoff, The history of water electrolysis from its beginnings to the present, in: Electrochemical Power Sources: Fundamentals, Systems, and Applications: Hydrogen Production by Water Electrolysis, Elsevier B.V., Amsterdam, 2021, pp. 83-164, https://doi.org/10.1016/B978-0-12-819424-9.00010-00.

[10] E. Katz, Electrochemical contributions: William Nicholson (1753–1815), Electrochem. Sci. Adv. 2021 1 (2021) e2160003, https://doi.org/10.1002/elsa.202160003.

[11] J. Hou, M. Yang, Green Hydrogen Production by Water Electrolysis, CRC Press, 1st ed, Boca Raton, 2024, https://doi.org/10.1201/9781003368939.

[12] W. T. Grubb, US 2913511A, 1959.

[13] D.J. Connolly, W. Frank, D. Nemours, US 3282875, 1966.

[14] Keith Scott, Electrochemical Methods for Hydrogen Production, Royal Society of Chemistry, Cambridge, 2019, https://doi.org/10.1039/9781788016049.

[15] P. Millet, Fundamentals of Water Electrolysis, in: Hydrogen Production: Electrolysis, Wiley, Weinheim, 2015, pp. 33–62, https://doi.org/10.1002/9783527676507.ch2.

[16] K. Śpiewak, Electrochemical Water Electrolysis Fundamentals and Technologies, CRC Press, 1st ed, Boca Raton, 2020, https://doi.org/10.1201/9780429447884.

[17] M. Chatenet, B.G. Pollet, D.R. Dekel, F. Dionigi, J. Deseure, P. Millet, R.D. Braatz, M.Z. Bazant, M. Eikerling, I. Staffell, P. Balcombe, Y. Shao-horn, H. Scha¨fer, Water electrolysis-from textbook knowledge to the latest scientific strategies and industrial developments, Chem. Soc. Rev. 51 (2022) 4583–4762, https://doi.org/10.1039/d0cs01079k.

[18] P. Aggarwal, D. Sarkar, K. Awasthi, P.W. Menezes, Functional role of single-atom catalysts in electrocatalytic hydrogen evolution: Current developments and future challenges, Coord. Chem. Rev. 452 (2022) 214289, https://doi.org/10.1016/j.ccr.2021.214289.

[19] A. Raveendran, M. Chandran, R. Dhanusuraman, A comprehensive review on the electrochemical parameters and recent material development of electrochemical water splitting electrocatalysts, RSC. Adv. 13 (2023) 3843–3876, https://doi.org/10.1039/d2ra07642j.

[20] H.F. Araújo, J.A. Gómez, D.M.F. Santos, Proton-Exchange Membrane Electrolysis for Green Hydrogen Production: Fundamentals, Cost Breakdown, and Strategies to

Minimize Platinum-Group Metal Content in Hydrogen Evolution Reaction Electrocatalysts, Catalysts 14 (2024) 845, https://doi.org/10.3390/catal14120845.

[21] L. Wan, Z. Xu, Q. Xu, M. Pang, D. Lin, J. Liu, B. Wang, Key components and design strategy of the membrane electrode assembly for alkaline water electrolysis, Energy Environ Sci 16 (2023) 1384–1430, https://doi.org/10.1039/d3ee00142c.

[22] Z. Feng, C. Dai, P. Shi, X. Lei, R. Guo, B. Wang, X. Liu, J. You, Seven mechanisms of oxygen evolution reaction proposed recently: A mini review, J. Chem. Eng. 485 (2024) 149992, https://doi.org/10.1016/j.cej.2024.149992.

[23] B.D. Fahlman, Recent progress and perspective for oxygen evolution reaction under acidic environments, Mater. Chem. Front. (2023) 986–1014, https://doi.org/10.1007/978-1-4020-6120-2.

[24] M. Erden, M. Karakilcik, Experimental investigation of hydrogen production performance of various salts with a chlor-alkali method, Int. J. Hydrogen Energy 52 (2024) 546–560, https://doi.org/10.1016/j.ijhydene.2023.08.049.

[25] H. Tüysüz, Alkaline Water Electrolysis for Green Hydrogen Production, Acc. Chem. Res. (2023), https://doi.org/10.1021/acs.accounts.3c00709.

[26] S.A. Grigoriev, V.N. Fateev, D.G. Bessarabov, P. Millet, Current status, research trends, and challenges in water electrolysis science and technology, Int. J. Hydrogen Energy 45 (2020) 26036–26058, https://doi.org/10.1016/j.ijhydene.2020.03.109.

[27] A.L. Hoang, S. Balakrishnan, A. Hodges, G. Tsekouras, A. Al-Musawi, K. Wagner, C.Y. Lee, G.F. Swiegers, G.G. Wallace, High-performing catalysts for energy-efficient commercial alkaline water electrolysis, Sustain. Energy Fuels 7 (2022) 31–60, https://doi.org/10.1039/d2se01197b.

[28] A.H. Faqeeh, M.D. Symes, Zero-gap bipolar membrane water electrolyzers: Principles, challenges and practical insights, Electrochim. Acta 493 (2024) 144345, https://doi.org/10.1016/j.electacta.2024.144345.

[29] S. Sebbahi, A. Assila, A. Alaoui Belghiti, S. Laasri, S. Kaya, E.K. Hlil, S. Rachidi, A. Hajjaji, A comprehensive review of recent advances in alkaline water electrolysis for

hydrogen production, Int. J. Hydrogen Energy 82 (2024) 583–599, https://doi.org/10.1016/j.ijhydene.2024.07.428.

[30] T. Kou, S. Wang, Y. Li, Perspective on High-Rate Alkaline Water Splitting, ACS Mater. Lett. 3 (2021) 224–234, https://doi.org/10.1021/acsmaterialslett.0c00536.

[31] Y. Zuo, S. Bellani, G. Saleh, M. Ferri, D. V. Shinde, M.I. Zappia, J. Buha, R. Brescia, M. Prato, R. Pascazio, A. Annamalai, D.O. de Souza, L. De Trizio, I. Infante, F. Bonaccorso, L. Manna, Ru-Cu Nanoheterostructures for Efficient Hydrogen Evolution Reaction in Alkaline Water Electrolyzers, J. Am. Chem. Soc. 145 (2023) 21419–21431, https://doi.org/10.1021/jacs.3c06726.

[32] S. Anantharaj, S.R. Ede, K. Karthick, S. Sam Sankar, K. Sangeetha, P.E. Karthik, S. Kundu, Precision and correctness in the evaluation of electrocatalytic water splitting: Revisiting activity parameters with a critical assessment, Energy Environ. Sci. 11 (2018) 744–771, https://doi.org/10.1039/c7ee03457a.

[33] Y. Zuo, S. Bellani, M. Ferri, G. Saleh, D. V. Shinde, M.I. Zappia, R. Brescia, M. Prato, L. De Trizio, I. Infante, F. Bonaccorso, L. Manna, High-performance alkaline water electrolyzers based on Ru-perturbed Cu nanoplatelets cathode, Nat. Commun. 14 (2023) 4680, https://doi.org/10.1038/s41467-023-40319-5.

[34] H. Osgood, S. V. Devaguptapu, H. Xu, J. Cho, G. Wu, Transition metal (Fe, Co, Ni, and Mn) oxides for oxygen reduction and evolution bifunctional catalysts in alkaline media, Nano Today 11 (2016) 601–625, https://doi.org/10.1016/j.nantod.2016.09.001.

[35] N. Du, C. Roy, R. Peach, M. Turnbull, S. Thiele, C. Bock, Anion-Exchange Membrane Water Electrolyzers, Chem. Rev. 122 (2022) 11830–11895, https://doi.org/10.1021/acs.chemrev.1c00854.

[36] A.H. Faqeeh, M.D. Symes, A standard electrolyzer test cell design for evaluating catalysts and cell components for anion exchange membrane water electrolysis, Electrochim. Acta 444 (2023) 142030, https://doi.org/10.1016/j.electacta.2023.142030.

[37] M. Carmo, D.L. Fritz, J. Mergel, D. Stolten, A comprehensive review on PEM water electrolysis, Int. J. Hydrogen Energy 38 (2013) 4901–4934, https://doi.org/10.1016/j.ijhydene.2013.01.151.

[38] X. Lin, J.Z.Y. Seow, Z.J. Xu, A brief introduction of electrode fabrication for proton exchange membrane water electrolyzers, JPhys. Energy 5 (2023) 034003, https://doi.org/10.1088/2515-7655/acccb1.

[39] K. Zhang, R. Zou, Advanced Transition Metal-Based OER Electrocatalysts: Current Status, Opportunities, and Challenges, Small 17 (2021) 2100129, https://doi.org/10.1002/smll.202100129.

[40] Q. Fu, J. Han, X. Wang, P. Xu, T. Yao, J. Zhong, W. Zhong, S. Liu, T. Gao, Z. Zhang, L. Xu, B. Song, 2D Transition Metal Dichalcogenides: Design, Modulation, and Challenges in Electrocatalysis, Adv. Mater. 33 (2021) 1907818, https://doi.org/10.1002/adma.201907818.

[41] P. Sabatier, La catalyse en chimie organique, Librairie Polytechnique, Paris et Lie`ge, 1920.

[42] S. Trasatti, Work function, electronegativity, and electrochemical behaviour of metals: III. Electrolytic hydrogen evolution in acid solutions, J. Electroanal. Chem. Interf. Electrochem. 39 (1972) 163–184, https://doi.org/10.1016/S0022-0728(72)80485-6.

[43] J.K. Nørskov, T. Bligaard, A. Logadottir, J.R. Kitchin, J.G. Chen, S. Pandelov, U. Stimming, 173 Trends in the Exchange Current for Hydrogen Evolution, J. Electrochem. Soc. 152 (2005) J23, https://doi.org/10.1149/1.1856988.

[44] H. Wendt, E. V. Spinacé, A. Oliveira Neto, M. Linardi, Electrocatalysis and electrocatalysts for low temperature fuel cells: Fundamentals, state of the art, research and development, Quim. Nova 28 (2005) 1066–1075, https://doi.org/10.1590/S0100-40422005000600023.

[45] M. Ďurovič, J. Hnát, K. Bouzek, Electrocatalysts for the hydrogen evolution reaction in alkaline and neutral media. A comparative review, J. Power Sources 493 (2021) 229708, https://doi.org/10.1016/j.jpowsour.2021.229708.

[46] S. Shaik, J. Kundu, Y. Yuan, W. Chung, D. Han, U. Lee, H. Huang, S. Il Choi, Recent Progress and Perspective in Pure Water-Fed Anion Exchange Membrane Water Electrolyzers, Adv. Energy Mater. 14 (2024) 2401956, https://doi.org/10.1002/aenm.202401956.

[47] A.M.I. Noor Azam, T. Ragunathan, N.N. Zulkefli, M.S. Masdar, E.H. Majlan, R. Mohamad Yunus, N.S. Shamsul, T. Husaini, S.N.A. Shaffee, Investigation of Performance of Anion Exchange Membrane (AEM) Electrolysis with Different Operating Conditions, Polymers 15 (2023) 1301, https://doi.org/10.3390/polym15051301.

[48] H.A. Miller, K. Bouzek, J. Hnat, S. Loos, C.I. Bernäcker, T. Weißgärber, L. Röntzsch, J. Meier-Haack, Green hydrogen from anion exchange membrane water electrolysis: a review of recent developments in critical materials and operating conditions, Sustain. Energy Fuels 4 (2020) 2114–2133, https://doi.org/10.1039/c9se01240k.

[49] E. Medina-Martos, J.L. Gálvez-Martos, J. Almarza, C. Lirio, D. Iribarren, A. Valente, J. Dufour, Environmental and economic performance of carbon capture with sodium hydroxide, J. CO2 UTIL 60 (2022) 101991, https://doi.org/10.1016/j.jcou.2022.101991.

[50] J. Guo, Y. Zheng, Z. Hu, C. Zheng, J. Mao, K. Du, M. Jaroniec, S.Z. Qiao, T. Ling, Direct seawater electrolysis by adjusting the local reaction environment of a catalyst, Nat. Energy 8 (2023) 264–272, https://doi.org/10.1038/s41560-023-01195-x.

[51] L.S. Darken, H.F. Meier, Conductances of Aqueous Solutions of the Hydroxides of Lithium, Sodium and Potassium at 25°, J. Am. Chem. Soc. 64 (1942) 621–623, https://doi.org/10.1021/ja01255a046.

[52] M. Schalenbach, A.R. Zeradjanin, O. Kasian, S. Cherevko, K.J.J. Mayrhofer, A perspective on low-temperature water electrolysis - Challenges in alkaline and acidic technology, Int. J. Electrochem Sci. 13 (2018) 1173–1226, https://doi.org/10.20964/2018.02.26.

[53] E. Barbara, Ullmann's encyclopedia of industrial chemistry, Wiley-VCH, Weinheim, 2000, https://doi.org/10.1002/14356007.

[54] G.A. Lindquist, Q. Xu, S.Z. Oener, S.W. Boettcher, Membrane Electrolyzers for Impure-Water Splitting, Joule 4 (2020) 2549–2561, https://doi.org/10.1016/j.joule.2020.09.020.

[55] W. Li, Z. Yin, Z. Gao, G. Wang, Z. Li, F. Wei, X. Wei, H. Peng, X. Hu, L. Xiao, J. Lu, L. Zhuang, Bifunctional ionomers for efficient co-electrolysis of CO_2 and pure water

towards ethylene production at industrial-scale current densities, Nat. Energy 7 (2022) 835–843, https://doi.org/10.1038/s41560-022-01092-9.

[56] W. Lai, Y. Qiao, Y. Wang, H. Huang, Stability Issues in Electrochemical CO_2 Reduction: Recent Advances in Fundamental Understanding and Design Strategies, Adv. Mater. 35 (2023) 2306288, https://doi.org/10.1002/adma.202306288.

[57] S. Yuan, C. Zhao, L. Luo, C. Fu, H. Li, L. An, X. Cheng, S. Shen, J. Yin, X. Yan, J. Zhang, Revealing the Role of the Ionomer at the Triple-Phase Boundary in a Proton-Exchange Membrane Water Electrolyzer, J. Phys. Chem. Lett. 15 (2024) 5223–5230, https://doi.org/10.1021/acs.jpclett.4c00851.

[58] J. Liu, Z. Kang, D. Li, M. Pak, S.M. Alia, C. Fujimoto, G. Bender, Y.S. Kim, A.Z. Weber, Elucidating the Role of Hydroxide Electrolyte on Anion-Exchange-Membrane Water Electrolyzer Performance, J. Electrochem. Soc. 168 (2021) 054522, https://doi.org/10.1149/1945-7111/ac0019.

[59] D. Xu, M.B. Stevens, M.R. Cosby, S.Z. Oener, A.M. Smith, L.J. Enman, K.E. Ayers, C.B. Capuano, J.N. Renner, N. Danilovic, Y. Li, H. Wang, Q. Zhang, S.W. Boettcher, Earth-Abundant Oxygen Electrocatalysts for Alkaline Anion-Exchange-Membrane Water Electrolysis: Effects of Catalyst Conductivity and Comparison with Performance in Three-Electrode Cells, ACS Catal. 9 (2019) 7–15, https://doi.org/10.1021/acscatal.8b04001.

[60] R. Pärnamäe, S. Mareev, V. Nikonenko, S. Melnikov, N. Sheldeshov, V. Zabolotskii, H.V.M. Hamelers, M. Tedesco, Bipolar membranes: A review on principles, latest developments, and applications, J. Memb. Sci. 617 (2021) 118538, https://doi.org/10.1016/j.memsci.2020.118538.

[61] H. Strathmann, J.J. Krol, H.J. Rapp, G. Eigenberger, Limiting current density and water dissociation in bipolar membranes, J. Memb. Sci. 125 (1997) 123–142, https://doi.org/10.1016/S0376-7388(96)00185-8.

[62] D.A. Vermaas, S. Wiegman, T. Nagaki, W.A. Smith, Ion transport mechanisms in bipolar membranes for (photo)electrochemical water splitting, Sustain. Energy Fuels 2 (2018) 2006–2015, https://doi.org/10.1039/c8se00118a.

[63] N.M. Vargas-Barbosa, G.M. Geise, M.A. Hickner, T.E. Mallouk, Assessing the utility of bipolar membranes for use in photoelectrochemical water-splitting cells, ChemSusChem 7 (2014) 3017–3020, https://doi.org/10.1002/cssc.201402535.

[64] Y. Ding, P. Cai, Z. Wen, Electrochemical neutralization energy: from concept to devices, Chem. Soc. Rev. 50 (2021) 1495–1511, https://doi.org/10.1039/d0cs01239d.

[65] V. Kaiser, S.T. Bramwell, P.C.W. Holdsworth, R. Moessner, Onsager's Wien effect on a lattice, Nat. Mater. 12 (2013) 1033–1037, https://doi.org/10.1038/nmat3729.

[66] J. Cai, E. Griffin, V.H. Guarochico-Moreira, D. Barry, B. Xin, M. Yagmurcukardes, S. Zhang, A.K. Geim, F.M. Peeters, M. Lozada-Hidalgo, Wien effect in interfacial water dissociation through proton-permeable graphene electrodes, Nat. Commun. 13 (2022) 5776, https://doi.org/10.1038/s41467-022-33451-1.

[67] L. Onsager, Deviations from Ohm's law in weak electrolytes, J. Chem. Phys. 2 (1934) 599–615, https://doi.org/10.1063/1.1749541.

[68] Z. Yan, L. Zhu, Y.C. Li, R.J. Wycisk, P.N. Pintauro, M.A. Hickner, T.E. Mallouk, The balance of electric field and interfacial catalysis in promoting water dissociation in bipolar membranes, Energy Environ. Sci. 11 (2018) 2235–2245, https://doi.org/10.1039/c8ee01192c.

[69] Y. Jeon, V.D.C. Tinh, V.D. Thuc, D. Kim, Ether-free polymer based bipolar electrolyte membranes without an interlayer catalyst for water electrolysis with durability at a high current density, J. Chem. Eng. 459 (2023) 141467, https://doi.org/10.1016/j.cej.2023.141467.

[70] R. Simons, Strong electric field effects on proton transfer between membrane bound amines and water, Nature 280 (1979) 824–826, https://doi.org/10.1038/280824a0.

[71] V.I. Zabolotskii, N. V Shel'deshov, N.P. Gnusin, Dissociation of Water Molecules in Systems with Ion-exchange Membranes, Russ. Chem. Rev. 57 (1988) 801–808, https://doi.org/10.1070/rc1988v057n08abeh003389.

[72] Y. Chen, J.A. Wrubel, W.E. Klein, S. Kabir, W.A. Smith, K.C. Neyerlin, T.G. Deutsch, High-Performance Bipolar Membrane Development for Improved Water Dissociation,

ACS Appl. Polym. Mater. 2 (2020) 4559−4569, https://doi.org/10.1021/acsapm.0c00653.

[73] J. Li, S.T. Morthensen, J. Zhu, S. Yuan, J. Wang, A. Volodine, J. Lin, J. Shen, B. Van der Bruggen, Exfoliated MoS_2 nanosheets loaded on bipolar exchange membranes interfaces as advanced catalysts for water dissociation, Sep. Purif. Technol. 194 (2018) 416–424, https://doi.org/10.1016/j.seppur.2017.11.065.

[74] S.Z. Oener, M.J. Foster, S.W. Boettcher, Accelerating water dissociation in bipolar membranes and for electrocatalysis, Science 369 (2020) 1099–1103.

[75] A.W. Tricker, J.K. Lee, F. Babbe, J.R. Shin, A.Z. Weber, X. Peng, Engineering Bipolar Interfaces for Water Electrolysis Using Earth-Abundant Anodes, ACS Energy Lett. 8 (2023) 5275–5280, https://doi.org/10.1021/acsenergylett.3c02351.

[76] E.A. Hernández-Pagán, N.M. Vargas-Barbosa, T. Wang, Y. Zhao, E.S. Smotkin, T.E. Mallouk, Resistance and polarization losses in aqueous buffer–membrane electrolytes for water-splitting photoelectrochemical cells, Energy Environ. Sci. 5 (2012) 7582–7589, https://doi.org/10.1039/c2ee03422k.

[77] L. Chen, Q. Xu, S.Z. Oener, K. Fabrizio, S.W. Boettcher, Design principles for water dissociation catalysts in high-performance bipolar membranes, Nat. Commun. 13 (2022) 3846, https://doi.org/10.1038/s41467-022-31429-7.

[78] M.A. Blommaert, J.A.H. Verdonk, H.C.B. Blommaert, W.A. Smith, D.A. Vermaas, Reduced Ion Crossover in Bipolar Membrane Electrolysis via Increased Current Density, Molecular Size, and Valence, ACS Appl. Energy Mater. 3 (2020) 5804–5812, https://doi.org/10.1021/acsaem.0c00687.

[79] B. Mayerhöfer, D. McLaughlin, T. Böhm, M. Hegelheimer, D. Seeberger, S. Thiele, Bipolar Membrane Electrode Assemblies for Water Electrolysis, ACS Appl. Energy Mater. 3 (2020) 9635–9644, https://doi.org/10.1021/acsaem.0c01127.

[80] M.A. Blommaert, D. Aili, R.A. Tufa, Q. Li, W.A. Smith, D.A. Vermaas, Insights and Challenges for Applying Bipolar Membranes in Advanced Electrochemical Energy Systems, ACS Energy Lett. 6 (2021) 2539–2548, https://doi.org/10.1021/acsenergylett.1c00618.

[81] P.K. Giesbrecht, M.S. Freund, Recent Advances in Bipolar Membrane Design and Applications, Chem. Mater. 32 (2020) 8060–8090, https://doi.org/10.1021/acs.chemmater.0c02829.

[82] E. Al-Dhubhani, R. Pärnamäe, J.W. Post, M. Saakes, M. Tedesco, Performance of five commercial bipolar membranes under forward and reverse bias conditions for acid-base flow battery applications, J. Memb. Sci. 640 (2021) 119748, https://doi.org/10.1016/j.memsci.2021.119748.

[83] J. Yang, M.J. Jang, X. Zeng, Y.S. Park, J. Lee, S.M. Choi, Y. Yin, Non-precious electrocatalysts for oxygen evolution reaction in anion exchange membrane water electrolysis: A mini review, Electrochem. Commun. 131 (2021) 107118, https://doi.org/10.1016/j.elecom.2021.107118.

[84] Z. Zakaria, S.K. Kamarudin, A review of alkaline solid polymer membrane in the application of AEM electrolyzer: Materials and characterization, Int. J. Energy Res. 45 (2021) 18337–1835, https://doi.org/10.1002/er.6983.

[85] D. Aili, M.R. Kraglund, S.C. Rajappan, D. Serhiichuk, Y. Xia, V. Deimede, J. Kallitsis, C. Bae, P. Jannasch, D. Henkensmeier, J.O. Jensen, Electrode Separators for the Next-Generation Alkaline Water Electrolyzers, ACS Energy Lett. 8 (2023) 1900–1910, https://doi.org/10.1021/acsenergylett.3c00185.

[86] R. Vinodh, T. Palanivel, S.S. Kalanur, B.G. Pollet, Recent advancements in catalyst coated membranes for water electrolysis: a critical review, Energy Advances 3 (2024) 1144–1166, https://doi.org/10.1039/d4ya00143e.

[87] N. Hensle, J. Hoffmann, Z. Najafianashrafi, T. Smolinka, P.Y. Abel Chuang, A. Weber, Understanding the use of carbon-based porous transport layers at the cathode in PEM water electrolysis, J. Power Sources 236913 (2025), https://doi.org/10.1016/j.jpowsour.2025.236913.

[88] J. Hemauer, S. Rehfeldt, H. Klein, A. Peschel, Performance and cost modelling taking into account the uncertainties and sensitivities of current and next-generation PEM water electrolysis technology, Int. J. Hydrogen Energy 48 (2023) 25619–25634, https://doi.org/10.1016/j.ijhydene.2023.03.050.

[89] Y. Wang, C.Y. Wang, K.S. Chen, Elucidating differences between carbon paper and carbon cloth in polymer electrolyte fuel cells, Electrochim. Acta 52 (2007) 3965–3975, https://doi.org/10.1016/j.electacta.2006.11.012.

[90] S.M. Mahnama, M. Khayat, Three dimensional investigation of the effect of MPL characteristics on water saturation in PEM fuel cells, J. Renew. Sustain. Energy. 9 (2017) 014301, https://doi.org/10.1063/1.4974339.

[91] Z. Kang, G. Yang, J. Mo, S. Yu, D.A. Cullen, S.T. Retterer, T.J. Toops, M.P. Brady, G. Bender, B.S. Pivovar, J.B. Green, F.Y. Zhang, Developing titanium micro/nano porous layers on planar thin/tunable LGDLs for high-efficiency hydrogen production, Int. J. Hydrogen Energy 43 (2018) 14618–14628, https://doi.org/10.1016/j.ijhydene.2018.05.139.

[92] C. Rakousky, U. Reimer, K. Wippermann, M. Carmo, W. Lueke, D. Stolten, An analysis of degradation phenomena in polymer electrolyte membrane water electrolysis, J. Power Sources 326 (2016) 120–128, https://doi.org/10.1016/j.jpowsour.2016.06.082.

[93] B. Chen, A.L.G. Biancolli, C.L. Radford, S. Holdcroft, Stainless Steel Felt as a Combined OER Electrocatalyst/Porous Transport Layer for Investigating Anion-Exchange Membranes in Water Electrolysis, ACS Energy Lett. 8 (2023) 2661–2667, https://doi.org/10.1021/acsenergylett.3c00878.

[94] M. Maier, K. Smith, J. Dodwell, G. Hinds, P.R. Shearing, D.J.L. Brett, Mass transport in PEM water electrolysers: A review, Int. J. Hydrogen Energy 47 (2022) 30–56, https://doi.org/10.1016/j.ijhydene.2021.10.013.

[95] G. Wang, Z. Liu, C. Liu, W. Chen, Molecular Study of Nonequilibrium Transport Mechanism for Proton and Water in Porous Proton Exchange Membranes, Int. J. Energy Res. 2023 (2023), https://doi.org/10.1155/2023/1138198.

[96] H.A. Elwan, M. Mamlouk, K. Scott, A review of proton exchange membranes based on protic ionic liquid/polymer blends for polymer electrolyte membrane fuel cells, J. Power Sources 484 (2021) 229197, https://doi.org/10.1016/j.jpowsour.2020.229197.

[97] W. Wang, Y. Sun, X. Liu, M. Wei, C. Zhao, K.G. Zhou, M. Wu, Hydroxide exchange membranes towards water electrolysis and fuel cells: A review on the recent advances,

challenges and opportunities, Adv. Membr. 4 (2024) 100111, https://doi.org/10.1016/j.advmem.2024.100111.

[98] W. Zheng, L. He, T. Tang, R. Ren, H. Lee, G. Ding, L. Wang, L. Sun, Poly(Dibenzothiophene-Terphenyl Piperidinium) for High-Performance Anion Exchange Membrane Water Electrolysis, Angew. Chem. Int. Ed. 63 (2024) e202405738, https://doi.org/10.1002/anie.202405738.

[99] K.N. Grew, W.K.S. Chiu, A Dusty Fluid Model for Predicting Hydroxyl Anion Conductivity in Alkaline Anion Exchange Membranes, J. Electrochem. Soc. 157 (2010) B327, https://doi.org/10.1149/1.3273200.

[100] A.K. Samuel, A.H. Faqeeh, W. Li, Z. Ertekin, Y. Wang, J. Zhang, N. Gadegaard, D.A.J. Moran, M.D. Symes, A.Y. Ganin, Assessing Challenges of 2D-Molybdenum Ditelluride for Efficient Hydrogen Generation in a Full-Scale Proton Exchange Membrane (PEM) Water Electrolyzer, ACS Sustainable Chem. 12 (2024) 1276–1285, https://doi.org/10.1021/acssuschemeng.3c06616.

[101] A. Villamayor, A. Alba, L. V. Barrio, S. Rojas, E. Gutierrez-Berasategui, Magnetron Sputtered Low-Platinum Loading Electrode as HER Catalyst for PEM Electrolysis, Coatings 14 (2024) 868, https://doi.org/10.3390/coatings14070868.

[102] A. Lim, J. Kim, H.J. Lee, H.-J. Kim, S.J. Yoo, J.H. Jang, H. Young Park, Y.-E. Sung, H.S. Park, Low-loading IrO_2 supported on Pt for catalysis of PEM water electrolysis and regenerative fuel cells, Appl. Cata.l B 272 (2020) 118955, https://doi.org/10.1016/j.apcatb.2020.118955.

[103] W. Wang, S. Chen, J. Li, W. Wang, Fabrication of catalyst coated membrane with screen printing method in a proton exchange membrane fuel cell, Int. J. Hydrogen Energy 40 (2015) 4649–4658, https://doi.org/10.1016/j.ijhydene.2015.02.027.

[104] J. Hnát, M. Plevova, R.A. Tufa, J. Zitka, M. Paidar, K. Bouzek, Development and testing of a novel catalyst-coated membrane with platinum-free catalysts for alkaline water electrolysis, Int. J. Hydrogen Energy 44 (2019) 17493–17504, https://doi.org/10.1016/j.ijhydene.2019.05.054.

[105] N. Chen, S.Y. Paek, J.Y. Lee, J.H. Park, S.Y. Lee, Y.M. Lee, High-performance anion exchange membrane water electrolyzers with a current density of 7.68 A cm^{-2} and a durability of 1000 hours, Energy Environ. Sci. 14 (2021) 6338–6348, https://doi.org/10.1039/d1ee02642a.

[106] J.K. Lee, J.H. Seo, J. Lim, S. Park, H.W. Jang, Best Practices in Membrane Electrode Assembly for Water Electrolysis, ACS Mater. Lett. (2024) 2757–2786, https://doi.org/10.1021/acsmaterialslett.4c00699.

[107] L. Peng, Z. Wei, Catalyst Engineering for Electrochemical Energy Conversion from Water to Water: Water Electrolysis and the Hydrogen Fuel Cell, Engineering 6 (2020) 653–679, https://doi.org/10.1016/j.eng.2019.07.028.

[108] K. Denk, R. Kodým, J. Hnát, M. Paidar, T. Turek, K. Bouzek, Mass transfer limitation phenomena across the separator in a zero-gap alkaline water electrolysis stack: Anion-selective polymer electrolyte membrane vs. ZirfonTM Perl UTP 500 case study, J. Chem. Eng. 479 (2024) 147354, https://doi.org/10.1016/j.cej.2023.147354.

[109] E. Kuhnert, M. Heidinger, D. Sandu, V. Hacker, M. Bodner, Analysis of PEM Water Electrolyzer Failure Due to Induced Hydrogen Crossover in Catalyst-Coated PFSA Membranes, Membranes 13 (2023) 348, https://doi.org/10.3390/membranes13030348.

[110] K. Yassin, R. Attias, Y. Tsur, D.R. Dekel, Identifying and Quantifying Loss Sources in Anion-Exchange Membrane Water Electrolyzers, ACS Electrochem. 1 (2025) 655–666, https://doi.org/10.1021/acselectrochem.4c00156.

[111] E. Amores, M. Sánchez, N. Rojas, M. Sánchez-Molina, 9 - Renewable hydrogen production by water electrolysis, in: Sustainable Fuel Technologies Handbook, Elsevier B.V., Amsterdam, 2021, pp. 271–313, https://doi.org/10.1016/B978-0-12-822989-7.00010-X.

[112] S. Niroula, C. Chaudhary, A. Subedi, B.S. Thapa, Parametric Modelling and Optimization of Alkaline Electrolyzer for the Production of Green Hydrogen, IOP Conf. Ser. Mater. Sci. Eng. 1279 (2023) 012005, https://doi.org/10.1088/1757-899x/1279/1/012005.

[113] K. Zouhri, S.Y. Lee, Evaluation and optimization of the alkaline water electrolysis ohmic polarization: Exergy study, Int. J. Hydrogen Energy 41 (2016) 7253–7263, https://doi.org/10.1016/j.ijhydene.2016.03.119.

[114] Y. Li, L. Zhou, S. Guo, Noble metal-free electrocatalytic materials for water splitting in alkaline electrolyte, EnergyChem 3 (2021) 100053, https://doi.org/10.1016/j.enchem.2021.100053.

[115] O. van der Heijden, S. Park, R.E. Vos, J.J.J. Eggebeen, M.T.M. Koper, Tafel Slope Plot as a Tool to Analyze Electrocatalytic Reactions, ACS Energy Lett. 9 (2024) 1871–1879, https://doi.org/10.1021/acsenergylett.4c00266.

[116] S. Anantharaj, S. Noda, M. Driess, P.W. Menezes, The Pitfalls of Using Potentiodynamic Polarization Curves for Tafel Analysis in Electrocatalytic Water Splitting, ACS Energy Lett. 6 (2021) 1607–1611, https://doi.org/10.1021/acsenergylett.1c00608.

[117] M. Nazari, M. Ghaemmaghami, Approach to Evaluation of Electrocatalytic Water Splitting Parameters, Reflecting Intrinsic Activity: Toward the Right Pathway, ChemSusChem 16 (2023) e202202126, https://doi.org/10.1002/cssc.202202126.

[118] S. Anantharaj, S. Kundu, Do the Evaluation Parameters Reflect Intrinsic Activity of Electrocatalysts in Electrochemical Water Splitting?, ACS Energy Lett. 4 (2019) 1260–1264, https://doi.org/10.1021/acsenergylett.9b00686.

[119] M. Liu, L.Y.S. Lee, K. Wong, Highly Efficient Electrocatalytic Water Splitting, in: Handbook of Nanomaterials and Nanocomposites for Energy and Environmental Applications, Springer Cham, Cham, 2021, pp. 1335–1367, https://doi.org/10.1007/978-3-030-36268-3_131.

[120] P. Atkins, J. De Paula, Peter Atkins, in: J. Keeler, Atkins' Physical Chemistry, Oxford University Press, 12th ed, Oxford, 2022.

[121] Y. Zhang, R. Yan, X. Xu, C. He, M. Zhou, Z. Zeng, T. Ma, Next Generation Noble Metal-Engineered Catalysts : From Structure Evolution to Structure-Reactivity Correlation in Water Splitting, Adv. Funct. Mater. 34 (2024) 2308813, https://doi.org/10.1002/adfm.202308813.

[122] H.L.A. Dickinson, M.D. Symes, NiCuAg: An electrochemically-synthesised trimetallic stack for CO_2 reduction, Electrochim. Acta 493 (2024) 144355, https://doi.org/10.1016/j.electacta.2024.144355.

[123] M.R. Ram, S. Heidari, A. Vergara, M. Villican, P. Preuss, B. Camarada, A. Fischer, Rhenium-Based Electrocatalysts for Water Splitting, ACS Mater. Au (2023), https://doi.org/10.1021/acsmaterialsau.2c00077.

[124] Q. Feng, X.Z. Yuan, G. Liu, B. Wei, Z. Zhang, H. Li, H. Wang, A review of proton exchange membrane water electrolysis on degradation mechanisms and mitigation strategies, J. Power Sources 366 (2017) 33–55, https://doi.org/10.1016/j.jpowsour.2017.09.006.

[125] U.O. Nwabara, M.P. de Heer, E.R. Cofell, S. Verma, E. Negro, P.J.A. Kenis, Towards accelerated durability testing protocols for CO_2 electrolysis, J. Mater. Chem. A 8 (2020) 22557–22571, https://doi.org/10.1039/D0TA08695A.

[126] E. Urbano, E. Pahon, N. Yousfi-Steiner, M. Guillou, Accelerated stress testing in proton exchange membrane water electrolysis - critical review, J. Power Sources 623 (2024) 235451, https://doi.org/10.1016/j.jpowsour.2024.235451.

[127] G. Tsotridis and A. Pilenga, EU harmonized protocols for testing of low temperature water electrolysis, Publications Office of the EU, 2021, https://doi.org/10.2760/58880.

[128] E. Kuhnert, V. Hacker, M. Bodner, A Review of Accelerated Stress Tests for Enhancing MEA Durability in PEM Water Electrolysis Cells, Int. J. Energy Res. 2023 (2023) 1–23, https://doi.org/10.1155/2023/3183108.

[129] N. Li, S.S. Araya, S.K. Kær, Investigating low and high load cycling tests as accelerated stress tests for proton exchange membrane water electrolysis, Electrochim. Acta 370 (2021) 137748, https://doi.org/10.1016/j.electacta.2021.137748.

[130] P. Aßmann, A.S. Gago, P. Gazdzicki, K.A. Friedrich, M. Wark, Toward developing accelerated stress tests for proton exchange membrane electrolyzers, Curr. Opin. Electrochem. 21 (2020) 225–233, https://doi.org/10.1016/j.coelec.2020.02.024.

[131] P. Lettenmeier, R. Wang, R. Abouatallah, S. Helmly, T. Morawietz, R. Hiesgen, S. Kolb, F. Burggraf, J. Kallo, A.S. Gago, K.A. Friedrich, Durable Membrane Electrode Assemblies for Proton Exchange Membrane Electrolyzer Systems Operating at High Current Densities, Electrochim. Acta 210 (2016) 502–511, https://doi.org/10.1016/j.electacta.2016.04.164.

[132] M.P. Browne, J. Dodwell, F. Novotny, S. Jaśkaniec, P.R. Shearing, V. Nicolosi, D.J.L. Brett, M. Pumera, Oxygen evolution catalysts under proton exchange membrane conditions in a conventional three electrode cellvs.electrolyser device: a comparison study and a 3D-printed electrolyser for academic labs, J. Mater. Chem. A 9 (2021) 9113–9123, https://doi.org/10.1039/d1ta00633a.

Chapter 2: Experimental Techniques

Abstract

In this Chapter, the main experimental techniques (electrochemical and analytical) used in Chapters 3 to 5 will be explained, as well as providing theoretical background about each technique.

2.1. Electrochemical characterisation techniques

Electrochemical characterisation techniques are methods employed to investigate chemical reactions involving electron transfer at an electrolyte/electrode interface, where the electrochemical double layer is formed, and ion movement through the electrolyte, maintaining the overall charge balance across the electrolyte. These electrochemical reactions are considered as reduction-oxidation reactions (i.e. redox reactions), whereby species lose electrons and other species accept these electrons, and these reactions take place in an electrochemical cell. Electrochemical cells are devices composed of two electrodes (anode and cathode, whereat oxidation and reduction reactions take place, respectively) submerged in an electrolyte placed in a single chamber. These two electrodes can be submerged in two different electrolytes placed in two chambers (H-cell configuration), which are separated by a non-electronic conductive barrier (membrane or diaphragm) preventing the mixing of the catholyte and anolyte but allowing the permeation of ions.

In broad terms, electrochemical characterisation techniques can be divided into three primary categories: potential-controlled (e.g. linear sweep voltammetry and chronoamperometry), current-controlled (e.g. chronopotentiometry), and impedance analysis (e.g. electrochemical impedance spectroscopy) techniques. In this section, a brief explanation of the electrochemical methods used throughout this thesis is provided, with an emphasis on their experimental setups and the type of experimental results each technique can yield.

2.1.1. Linear sweep voltammetry

Linear sweep voltammetry is the most widely used electroanalytical technique due to its simplicity and high speed for producing preliminary results about the overall performance of three-electrode electrochemical cells and two-electrode electrochemical cells [1] (the latter only having working and counter electrodes, and no reference electrode). This technique is a potential-controlled electroanalytical technique for studying redox reactions. In this technique, a potential is applied to the working electrode, and it is swept linearly over time in a single direction (either toward a more negative or a more positive potential) at a constant scan rate. The resulting current is measured as a function of the applied potential [2]. The current measured in response to the applied potential is illustrated as a polarisation curve (i.e. I-V curve), which is called a voltammogram. Linear sweep voltammetry can be used to assess different electrocatalysts in a water electrolyser. For example, a voltammogram (Figure 1) generated in an experiment describes the overall water electrolysis process, where the oxygen evolution reaction occurred on an RuO_2 surface, and the hydrogen evolution reaction took place on the surface of either Pt/C or $MoTe_2$. The current density reflects the amount of charge obtained per time divided by the area of the electrode surface, indicating the performance of each electrocatalyst towards the hydrogen evolution reaction. Thus, Pt/C is considered an electrocatalyst with higher activity towards hydrogen evolution reaction compared to $MoTe_2$, as higher current density was generated when 2.0 V was applied to Pt/C.

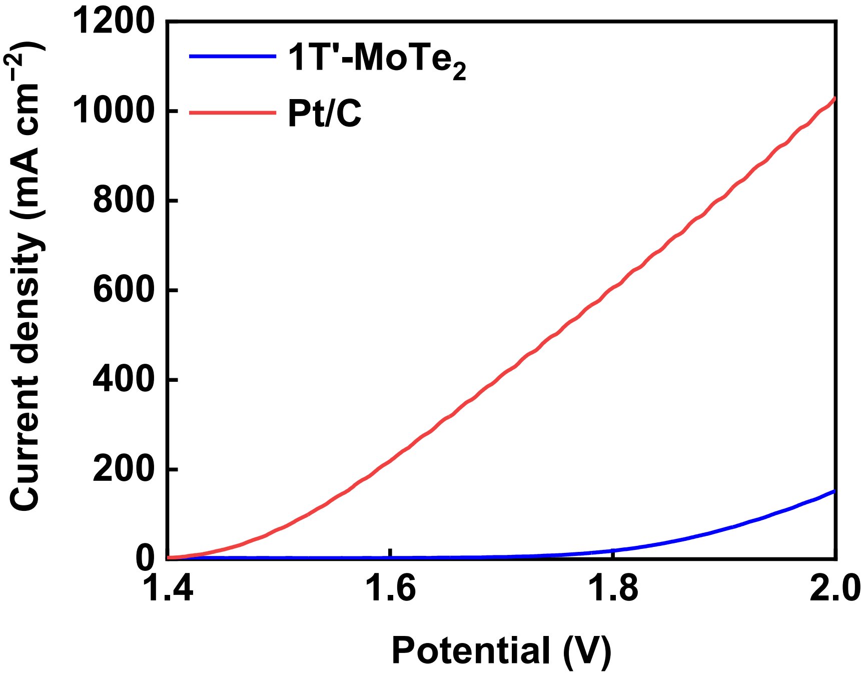

Figure 1: *The polarisation curve for water electrolysis process performed in a water electrolyser, where 1.5 mg* cm^{-2} *RuO_2 was employed as an oxygen evolution reaction catalyst and either 0.5 mg* cm^{-2} *Pt/C or 6 mg* cm^{-2} *$MoTe_2$ was employed as the hydrogen evolution reaction catalyst.*

However, linear sweep voltammetry is a transient polarisation technique providing overestimated performance of electrocatalysts because as the electrocatalytic interface does not stay at a specific potential for enough time to obtain a steady-state condition [3]. Therefore, steady-state techniques, such as chronoamperometry or chronopotentiometry should be used for accurate evaluation of electrocatalysts' performance and stability as well as that (as will be discussed later) of other water electrolyser components.

2.1.2. Electrolysis (chronoamperometry and chronopotentiometry)

Electrolysis is an electrochemical technique wherein an external driving force is applied to a system, allowing nonspontaneous redox reactions to take place. This technique is widely employed in numerous applications, such as electrosynthesis, electrodeposition, and electrometallurgy. It can be broadly classified into two categories dependent on the controlling variable in the process, whereby potential and current cannot be controlled concurrently: chronopotentiometry and chronoamperometry.

In chronoamperometry, a precise fixed potential is applied to the working electrode and the resultant current output, generated from faradaic reactions, is recorded simultaneously with respect to time [4]. In evaluating the performance of a water electrolyser, this technique provides information about the change in a reaction rate over time, whereby an increasing current measured as a function of time at a fixed applied potential generally signifies an increase in reaction kinetics over time. However, the decrease of the resultant current at a fixed potential might reflect the depletion of electroactive species near the electrode/electrolyte interface (either by reduction or oxidation), in which the drop of current to 0 A (theoretically speaking) is an indication of electrolysis completion [4]. An example of this chronoamperometric analysis using a constant potential of 2.0 V (40 °C) in an anion exchange membrane water electrolyser consisting of a stainless steel fibre paper used as an anode is shown in Figure 2. The plot shows two distinct stages. In the initial stage, which is known as the transient period, there is a rapid increase in current density occurs due to changes in the concentration of reactants at the electrode surface [5]. Subsequently, the system enters the steady-state period, during which the current levels out and remains constant over time [6].

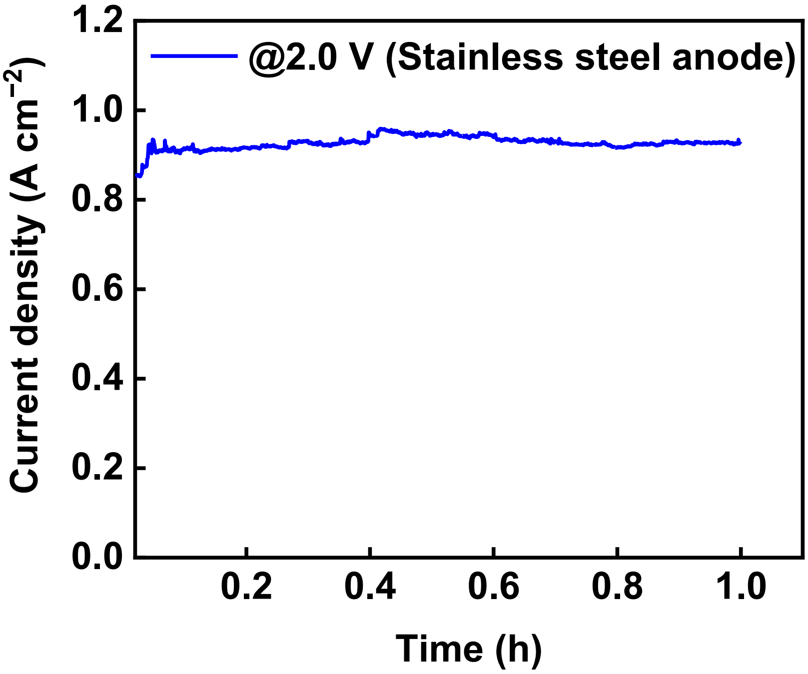

Figure 2: *The electrochemical activation of a stainless steel fibre paper, which was used as the anode catalyst in a water electrolyser, at 2.0 V. A Sustainion membrane and 0.5 mg cm*$^{-2}$ *Pt/C deposited on Sigracet carbon paper were employed as anion exchange membrane and hydrogen evolution reaction catalysts, respectively.*

In contrast, chronopotentiometry is a current-controlled technique in which a fixed current is applied to the working electrode to measure the corresponding potential as a function of time. The variation of potential can reflect the steady-state performance and durability of water electrolyser components at a fixed current during water electrolysis process. For instance, in case of assessing a water electrolyser using this technique (Figure 3), an increase in the potential (i.e. higher overpotential) required to maintain a specific current throughout electrolysis indicates a drop in performance or durability of this electrolyser. However, it is not feasible to make a comprehensive characterisation of the water electrolyser components by using this technique solely. Therefore, other techniques, such as electrochemical impedance spectroscopy, scanning electron microscopy, and inductively coupled plasma optical emission spectroscopy should be used.

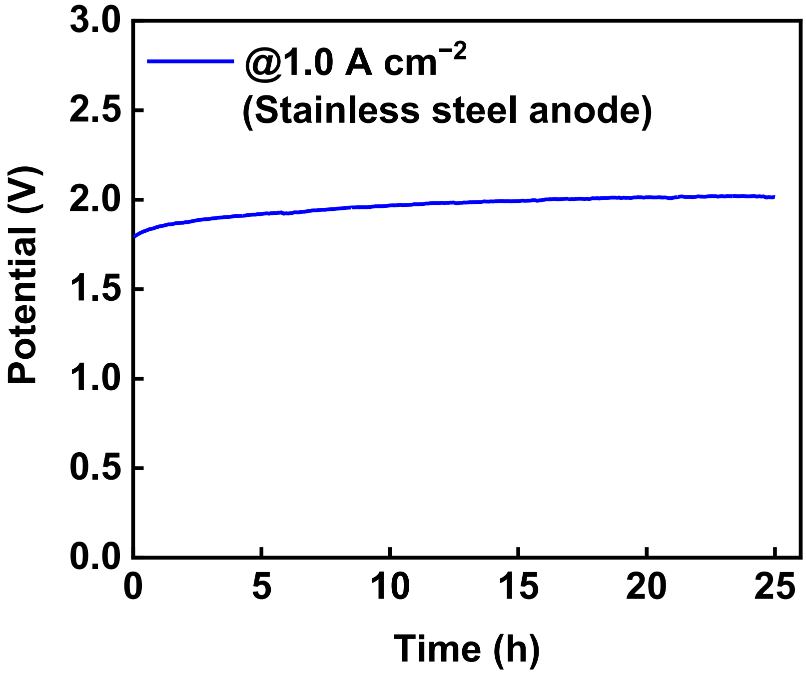

Figure 3: *The chronopotentiometric evaluation of a water electrolyser at 1.0 A cm^{-2} using a Sustainion membrane, stainless steel fibre paper as the anode, and 0.5 mg cm^{-2} Pt/C deposited on Sigracet carbon paper as the cathode [7].*

2.1.3. Electrochemical impedance spectroscopy

Electrochemical impedance spectroscopy is a powerful, versatile, and non-invasive diagnostic technique for measuring the impedances (i.e. frequency-dependent resistances to the flow of electrical current) within various electrochemical systems. Ohm's law (equation 1) describes resistance as to the ratio between potential and current.

$$R = \frac{E}{I} \qquad (1)$$

where R, E, and I depict the resistance, potential, and current, respectively.

However, the use of this law is limited to only an ideal resistor, having numerous simplified properties. An ideal resistor assumes that the resultant AC current signal and AC applied potential signal are in the same phase, yet there is a phase shift between the resultant current and applied potential in the real world, as shown in Figure 4. Thus, impedance is used in practice, whereby more circuit elements displaying much more complex behaviour are considered.

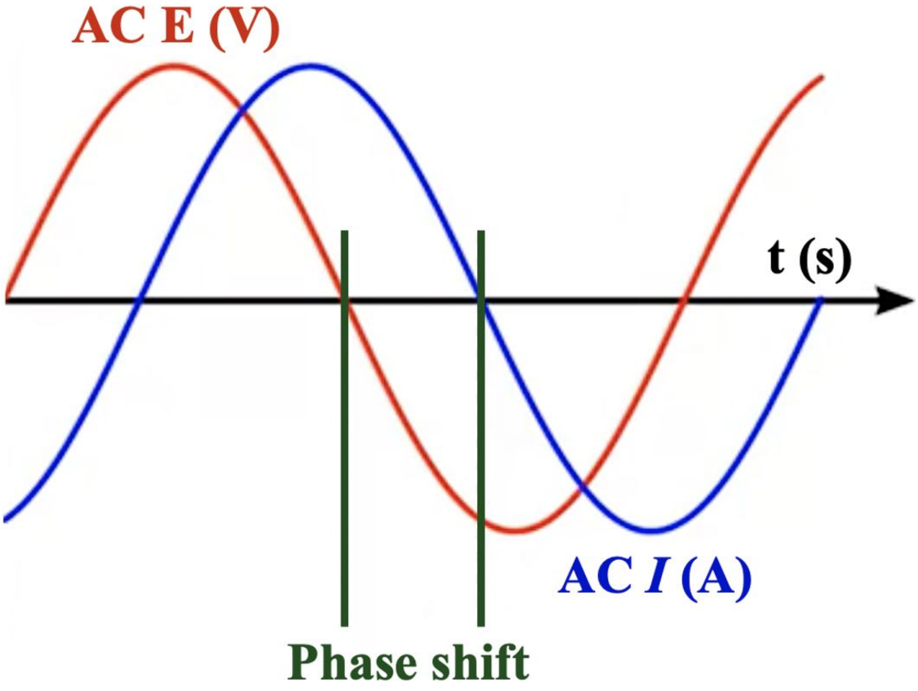

Figure 4: *The AC E signal, expressed as a function of time, for the applied potential and the resultant AC I signal through a resistor, with a phase shift separating the two waves.*

The impedance is measured by applying a sinusoidal potential perturbation, either AC potential (i.e. potentiostatic mode) or AC current (i.e. galvanostatic mode), over a broad range of different frequencies, then observing the corresponding AC current signal or AC potential signal, respectively [8]. In terms of water electrolysis, electrochemical impedance spectroscopy provides valuable insights into several processes taking place within an electrolyser, including mass transport phenomena (e.g. bubble formation), charge transfer kinetics, and ohmic resistance. The Nyquist plot is the most common way to present electrochemical impedance spectroscopy results in the water electrolysis field. In this plot, the x-axis depicts the positive real part of the impedance, whereas the y-axis depicts the imaginary part of the impedance. The system's response over a range of different frequencies is represented in semicircular arcs, with each point corresponding to a specific frequency [9]. A typical Nyquist plot obtained from testing a water electrolyser is shown in Figure 5, wherein the data collected at high frequency and low frequency are shown on the left and right sides of the plot, respectively. The impedance measured at high frequency, the x-axis intercept, represents the ohmic resistance, while the difference between the x-axis intercept and lower frequency intercept represents the charge transfer resistances (or polarisation resistances), attributing to the hydrogen and oxygen evolution reactions' kinetics. The first smaller arc in the left side of the plot represents the cathodic charge transfer resistance, while the bigger arc in the right side represents the anodic charge transfer resistance [7,9,10]. Since the oxygen evolution reaction involves the transfer of four electrons to two electrons for the hydrogen evolution reaction, its arc is bigger, indicating a larger resistance, and thus slower electrochemical kinetic rate compared to that of the hydrogen evolution reaction.

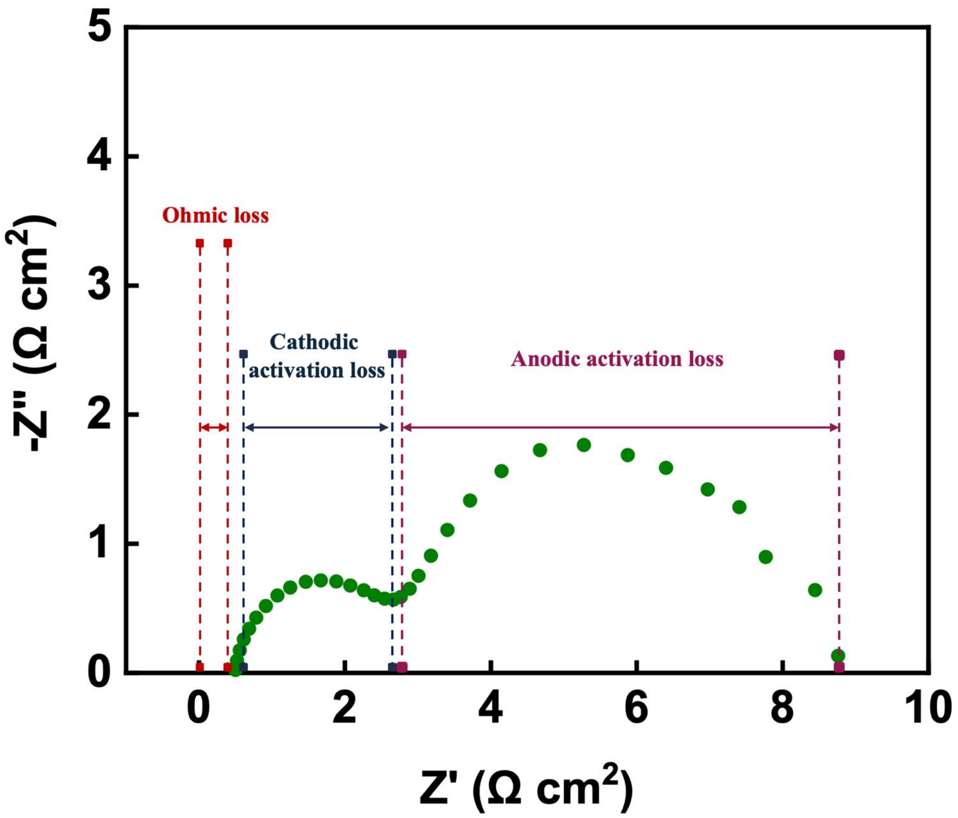

Figure 5: *Nyquist plot (at 1.8 V and 25 °C) of a water electrolyser using Nafion 117 as a proton exchange membrane and Ti fibre felt and 0.2 mg cm^{-2} Pt/C deposited carbon cloth as anode and cathode gas diffusion layers, respectively.*

The interpretation of electrochemical impedance spectroscopy experimental data can be achieved by fitting the impedance data by using an equivalent electrical circuit model resembling the electrochemical system. For example, the following equivalent electrical circuit (Figure 6) represents the various resistances within a water electrolyser under operation. In the equivalent circuit, L1 is the inductor representing the connector components and cables used for obtaining the impedance measurements, R1 refers to the ohmic resistance of the electrolyser components, and R2 and R3 represent the cathodic and anodic polarisation resistances, respectively. Additionally, Q2 and Q3 depict the constant phase elements of the cathodic and anodic processes, respectively. Constant phase elements are used to represent the double layer capacity due to the non-ideal capacitive behaviour of the electrochemical double layer, which is formed at the electrode/electrolyte interface, which arises from the inhomogeneous surface of solid electrodes (e.g. its roughness or porosity) [11]. In other words, they are circuit elements used to fit the experimental data, derived from electrochemical impedance spectroscopy measurements obtained during electrochemical processes, which deviate from an ideal capacitor behaviour [12].

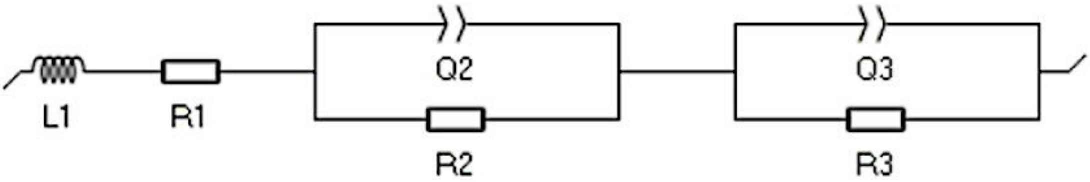

Figure 6: *An equivalent circuit model used for interpreting electrochemical impedance spectroscopy experimental data obtained from the overall water electrolysis process.*

2.2. Other characterisation techniques

2.2.1. Inductively coupled plasma atomic emission spectroscopy

Inductively coupled plasma optical emission spectrometry (ICP-OES) is a well-established analytical technique for elemental analysis at a concentration ranging from part per billion (ppb) to part per million (ppm). The fundamental principle of ICP-OES is based on the ability of atoms to absorb energy to transfer electrons from the ground state to an excited state, then releasing photons at specific wavelength as they move back to a lower energy level. The source of energy is heat generated from an argon plasma operating at 6,000–10,000 K. A typical ICP-OES instrument and its components are illustrated in Figure 7. The analyte is introduced by a peristaltic pump into the nebuliser, where the liquid analyte is converted into a fine aerosol, which is then transferred by a carrier gas (usually argon) into the plasma torch. There are two primary types of nebulisers: pneumatic, where a negative pressure is established by the flow of the carrier gas, converting the liquid into fine droplets, and ultrasonic, where fine droplets are generated by vibration at ultrasonic frequency [13]. The fine aerosol is carried by the carrier gas through the spray chamber to the inductively coupled plasma torch. The spray chamber only allows 1-5% of the aerosol to reach the plasma torch, whereby only the droplets with a diameter of approximately 10 μm pass into the torch, while the remaining larger droplets are disposed into a disposal container. The plasma torch is the energy source for breaking the analyte into atoms or ions and exciting their electrons temporarily by a heated argon gas, transferring these electrons to a higher energy state. The plasma is generated and maintained by the radio frequency generator, whereby a high-frequency electromagnetic field is generated in a metal coil, producing an output power in range of 700 to 1500 W [14]. Afterwards, the excited electrons decay back to the lower energy state, emitting radiation, at specific wavelengths (reflecting the type of elements or ions) with particular intensity (reflecting the concentration of elements or ions). The emitted radiation is directed by mirrors and other optical components to a detector that measures the photons of light at various wavelengths. The detector is coupled to a data processor (i.e. a computer), where the signals are shown as a graph displaying wavelengths on the x-axis and the emission intensity on the y-axis.

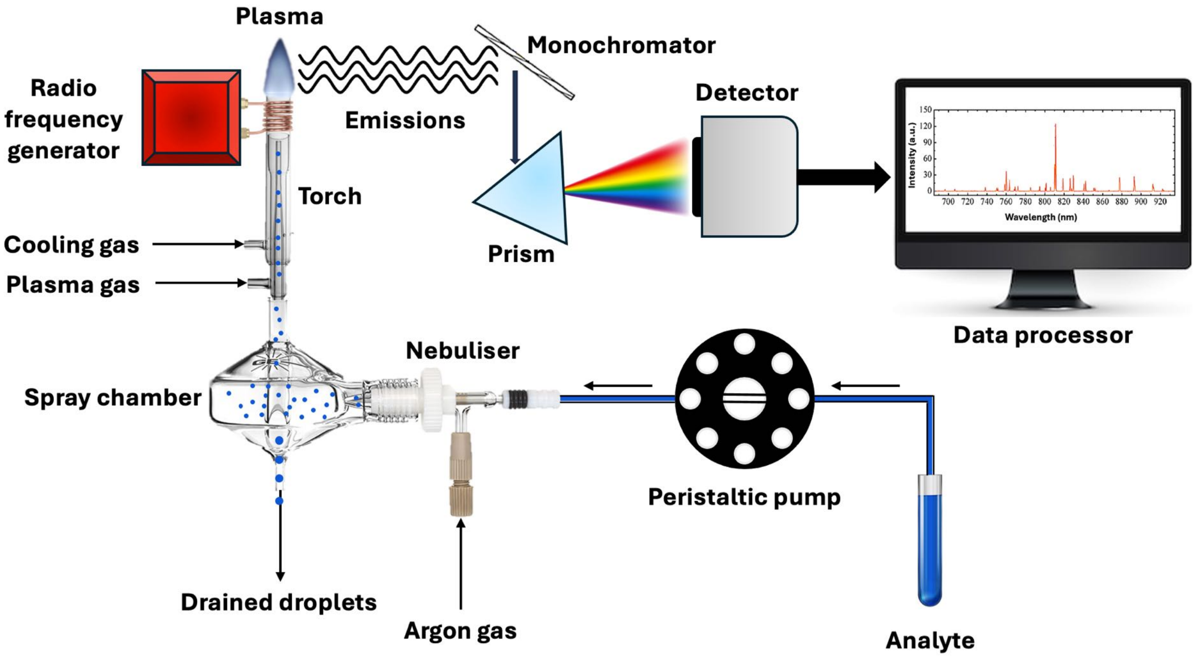

Figure 7: *Schematic illustration of a typical inductively coupled plasma optical emission spectrometer.*

2.2.2. Gas chromatography

Gas chromatography is an analytical technique for separating and analysing molecules by passing vaporised compounds (or a gas) through a column comprising a material impeding certain molecules more than others based on their volatility, whereby the most volatile pass first [15]. A typical gas chromatography instrument consists of the following components: carrier gas, an injector, a column, a column oven, a detector, a data processor (Figure 8).

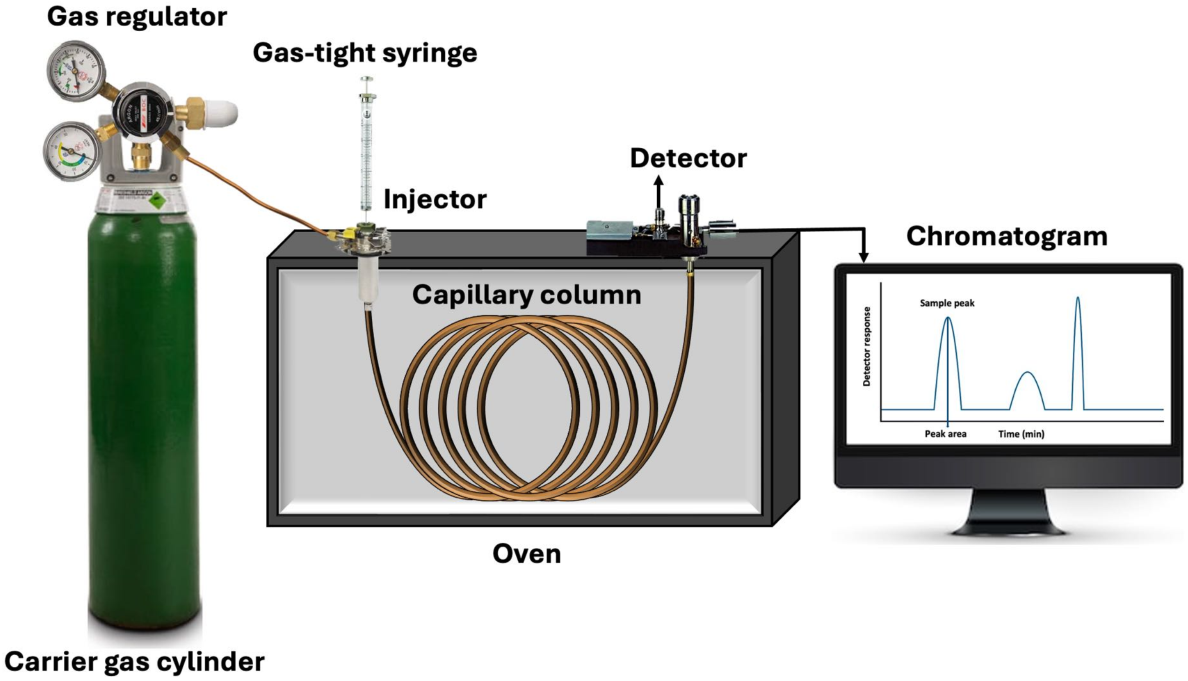

Figure 8: *Schematic illustration of a typical gas chromatography system.*

The carrier gas is supplied by using a high-pressure gas cylinder equipped with a pressure regulator. Inert gases, including argon, ultrapure helium, or nitrogen are mostly employed as carrier gases acting as the mobile phase carrying the analytes through the instrument. In the case of measuring hydrogen production using a water electrolyser, a gas-tight microsyringe can be used to collect a sample from the headspace of the liquid electrolyte reservoir. The sample is then injected into the injection port, where it is moved by the carrier gas across a column housed in a temperature-controlled oven. The stationary phase, where the compounds or gases are separated, is located on the inner surface of the column, either as a thin layer of an adsorbent material or a thin film of a highly viscous liquid. The separation of compounds or gases is based on their interaction strengths with the stationary phase, which is affected by many parameters, such as polarity, molecular size, and volatility[15] . Hence, the weaker the interaction is, the shorter the molecule interacts with the stationary phase, meaning the shorter time it takes to elute from the column (i.e. shorter retention time). Other factors, including carrier gas flow rate and column temperature and length can also affect the retention time [16]. The molecules eluting from the column reach the detector, wherein they produce electric signals as a function of time. These signals are sent by the detector to the data processor, where they are recorded as peaks with specific area (reflecting the amount of the molecule or gas in the analyte) at specific retention times; such a plot is called a “chromatogram”.

2.2.3. Fourier-Transform infrared (FT-IR) spectroscopy

The Fourier-Transform infrared spectroscopy is an analytical technique based on the infrared spectroscopy, wherein molecular compositions can be identified through the absorption of light by a sample within the infrared range (between 780 nm and 1 mm) of the electromagnetic spectrum [17]. The absorption causes atomic vibrations, such as stretching (a change in covalent bond length) and bending (a change in covalent bond angle), corresponding to specific functional groups in the sample [18]. A typical Fourier-Transform infrared spectrometer operates by directing infrared radiation (IR) into an interferometer, an optical device (Figure 9). Inside the interferometer, a beamsplitter divides the IR beam into two separate beams, which are then directed to two mirrors, a moveable mirror and a stationary mirror. These two mirrors reflect the two beams back to recombine, with the moveable mirror varying the travel distances of beams, creating phase difference between the beams when they interfere. This difference in travel distance allows the spectrometer to measure all the IR frequencies simultaneously, considerably increasing the measurement speed compared to analysing each frequency individually. After recombining the two interfering beams, the resultant beam is directed to the sample and then a detector, producing a signal called an interferogram, which is transformed mathematically into an IR spectrum [19].

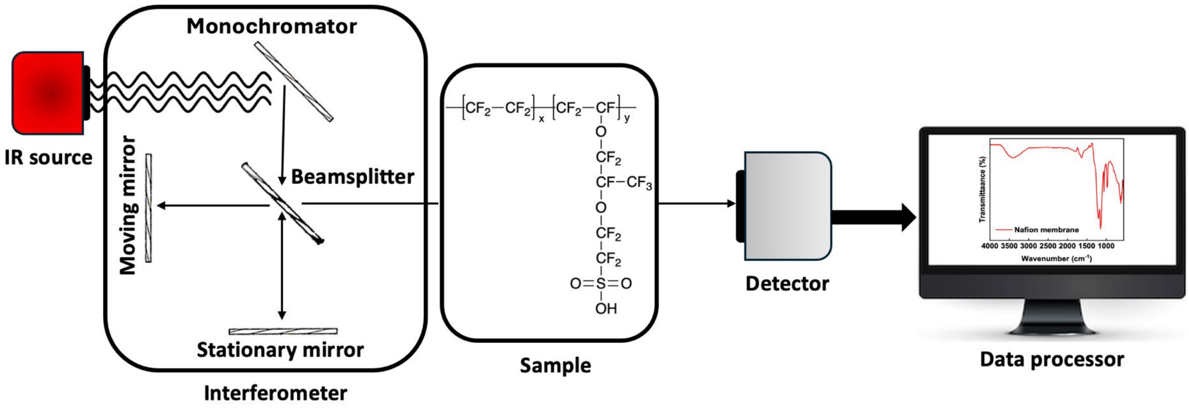

Figure 9: Schematic illustration of a typical Fourier-Transform infrared spectrometer.

2.2.4. Scanning electron microscopy

To obtain morphological and topological information of the surface of a sample (e.g. a polymer membrane), the scanning electron microscopy imaging technique can be used, radiating the sample with a focused beam of electrons. Inside a scanning electron microscope (Figure 10), an electron beam is generated by heating a filament of a high-melting point metal (e.g. tungsten) under high-vacuum conditions to protect the electrons from being scattered or absorbed by the air [20]. The electron beam is attracted by a positively charged anode plate and passed through numerous lenses and apertures condensing and concentrating the stream into a precise beam directed as parallel lines over the sample's surface by a magnetic device [21]. Upon hitting the sample's surface with the electron beam, several signals are produced, such as backscattered electrons ejected from the metal-coated (e.g. by Au or Pd) sample after interacting with the electron beam, secondary electrons emitted from exited atoms in the sample, and x-rays. The detection of these signals provides the scanned images [22].

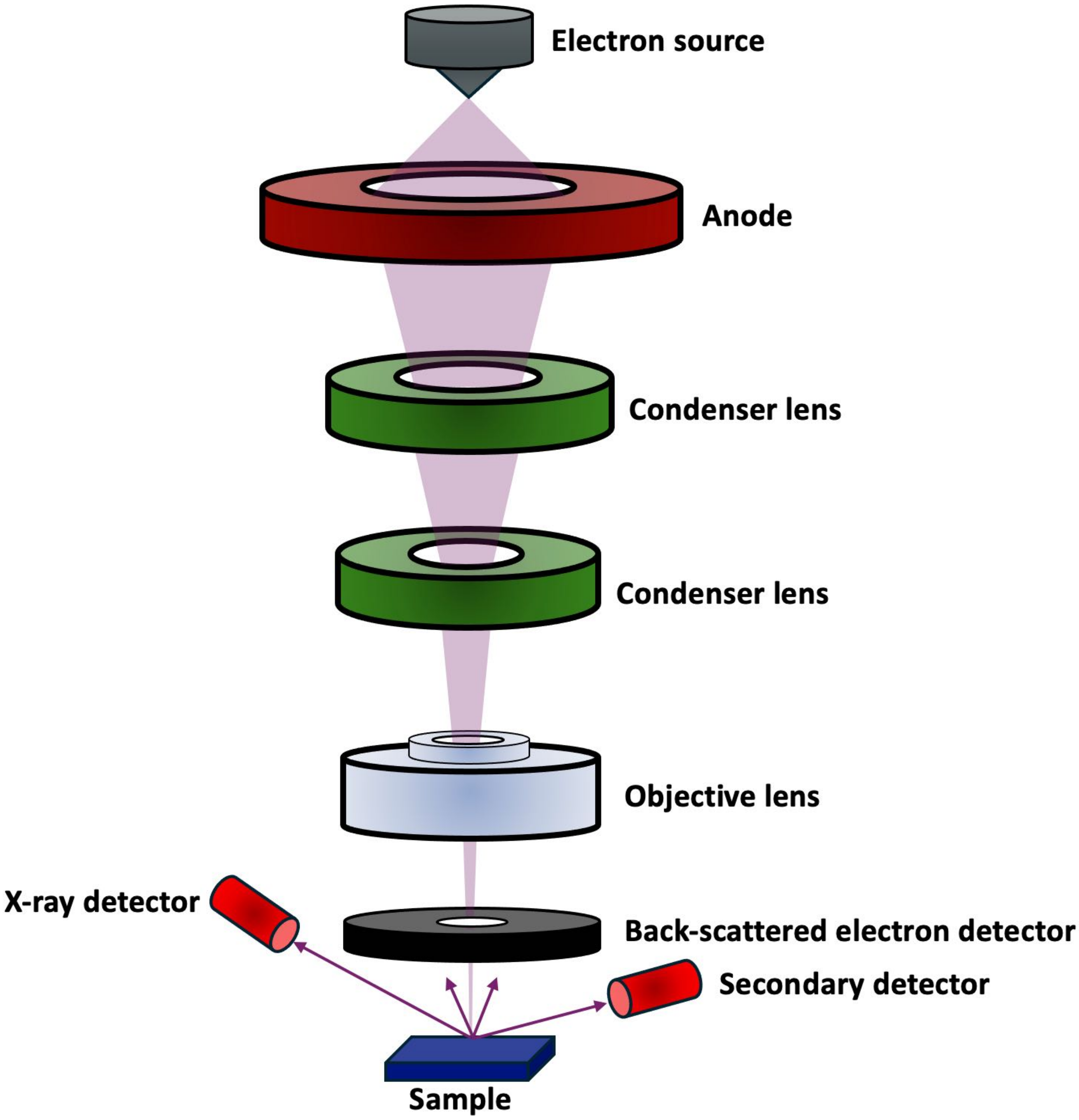

Figure 10: *Schematic illustration of a typical scanning electron microscope.*

References

[1] G. Bontempelli, N. Dossi, R. Toniolo, Linear Sweep and Cyclic, in: Reference Module in Chemistry, Molecular Sciences and Chemical Engineering, Elsevier Inc., Udine, 2016, pp. 1–10, https://doi.org/10.1016/b978-0-12-409547-2.12200-0.

[2] Inamuddin, R. Boddula, A.M. Asiri, Methods for Electrocatalysis Advanced Materials and Allied Applications, Springer Cham., 1st ed., Gewerbestraße, 2021, https://doi.org/10.1007/978-3-030-27161-9.

[3] S. Anantharaj, S. Kundu, S. Noda, Worrisome Exaggeration of Activity of Electrocatalysts Destined for Steady-State Water Electrolysis by Polarization Curves from Transient Techniques, J. Electrochem. Soc. 169 (2022) 014508, https://doi.org/10.1149/1945-7111/ac47ec.

[4] A.J. Bard, L.R. Faulkner, H.S. White, Electrochemical Methods: Fundamentals and Applications, Wiley, 3rd ed., New York, 2022.

[5] T.U. Haq, Y. Haik, Electrochemical Water Splitting Fundamentals, Challenges and Advances, Springer Singapore, 1st ed., Singapore, 2024, https://doi.org/10.1007/978-981-99-9860-9.

[6] P.J. Lingane, Chronopotentiometry and Chronoamperometry with Unshielded Planar Electrodes, Anal. Chem. 36 (1964) 1723–1726, https://doi.org/10.1021/ac60215a010.

[7] A.H. Faqeeh, M.D. Symes, A standard electrolyzer test cell design for evaluating catalysts and cell components for anion exchange membrane water electrolysis, Electrochim Acta 444 (2023) 142030, https://doi.org/10.1016/j.electacta.2023.142030.

[8] A.C. Lazanas, M.I. Prodromidis, Electrochemical Impedance Spectroscopy─A Tutorial, ACS Meas. Sci. Au 3 (2023) 162–193, https://doi.org/10.1021/acsmeasuresciau.2c00070.

[9] I. Vincent, E.C. Lee, H.M. Kim, Comprehensive impedance investigation of low-cost anion exchange membrane electrolysis for large-scale hydrogen production, Sci. Rep. 11 (2021) 293, https://doi.org/10.1038/s41598-020-80683-6.

[10] S. Siracusano, S. Trocino, N. Briguglio, V. Baglio, A.S. Aricò, Electrochemical impedance spectroscopy as a diagnostic tool in polymer electrolyte membrane electrolysis, Materials 11 (2018) 1368, https://doi.org/10.3390/ma11081368.

[11] P. Córdoba-Torres, T.J. Mesquita, O. Devos, B. Tribollet, V. Roche, R.P. Nogueira, On the intrinsic coupling between constant-phase element parameters α and Q in electrochemical impedance spectroscopy, Electrochim. Acta 72 (2012) 172–178, https://doi.org/10.1016/j.electacta.2012.04.020.

[12] S.M. Gateman, O. Gharbi, H. Gomes de Melo, K. Ngo, M. Turmine, V. Vivier, On the use of a constant phase element (CPE) in electrochemistry, Curr. Opin. Electrochem. 36 (2022) 101133.

[13] J. Nölte, ICP Emission Spectrometry: A Practical Guide, Wiley, 2nd ed., Weinheim, 2021, https://doi.org/10.1002/9783527823635.

[14] S.R. Khan, B. Sharma, P.A. Chawla, R. Bhatia, Inductively Coupled Plasma Optical Emission Spectrometry (ICP-OES): a Powerful Analytical Technique for Elemental Analysis, Food Anal. Methods 15 (2022) 666–688, https://doi.org/10.1007/s12161-021-02148-4.

[15] K. Dettmer-Wilde, W. Engewald, Practical Gas Chromatography: A Comprehensive Reference, Springer Berlin, 1st ed., Heidelberg, 2014, https://doi.org/10.1007/978-3-642-54640-2.

[16] M.H. Gordon, Principles of gas chromatography, Principles and Applications of Gas Chromatography in Food Analysis, in: Ellis Horwood Series in Food Science and Technology, Springer, Boston, 1990, pp. 11–58, https://doi.org/10.1007/978-1-4613-0681-8_1.

[17] S.M. Jafari, A. Faridi Esfanjani, I. Katouzian, E. Assadpour, Release, Characterization, and Safety of Nanoencapsulated Food Ingredients, in: Nanoencapsulation of Food Bioactive Ingredients, Elsevier Inc., Amsterdam, 2017, pp. 401-453, https://doi.org/10.1016/B978-0-12-809740-3.00010-6.

[18] M.O. Guerrero-Pérez, G.S. Patience, Experimental methods in chemical engineering: Fourier transform infrared spectroscopy—FTIR, Can. J. Chem. Eng. 98 (2020) 25–33, https://doi.org/10.1002/cjce.23664.

[19] A. Dutta, Fourier Transform Infrared Spectroscopy, in: Spectroscopic Methods for Nanomaterials Characterization, Elsevier Inc., Amsterdam, 2017, pp. 73-93, https://doi.org/10.1016/B978-0-323-46140-5.00004-2.

[20] M. Omidi, A. Fatehinya, M. Farahani, Z. Akbari, S. Shahmoradi, F. Yazdian, M. Tahriri, K. Moharamzadeh, L. Tayebi, D. Vashaee, Characterization of biomaterials, in: Biomaterials for Oral and Dental Tissue Engineering, Elsevier, Duxford, 2017 pp. 97–115, https://doi.org/10.1016/B978-0-08-100961-1.00007-4.

[21] A. Moropoulou, E. Zendri, P. Ortiz, E.T. Delegou, I. Ntoutsi, E. Balliana, J. Becerra, R. Ortiz, Scanning Microscopy Techniques as an Assessment Tool of Materials and Interventions for the Protection of Built Cultural Heritage, Scanning 2019 (2019), https://doi.org/10.1155/2019/5376214.

[22] J.G. Burr, Tools of the Cell Biologist, in: Medical Cell Biology, Elsevier, Burlington, 2008: pp. 1–26, https://doi.org/10.1016/B978-0-12-370458-0.50006-2.

Chapter 3: A Standard Electrolyser Test Cell Design for Evaluating Catalysts and Cell Components for Anion Exchange Membrane Water Electrolysis

Adopted from "A.H. Faqeeh, M.D. Symes, A standard electrolyser test cell design for evaluating catalysts and cell components for anion exchange membrane water electrolysis, Electrochim. Acta 444 (2023) 142030, https://doi.org/10.1016/j.electacta.2023.142030". Reproduced here with permission from Elsevier.

Acknowledgements and declarations

I express my appreciation to Brendon McGill, affiliated with School of Physics & Astronomy, University of Glasgow, for his valuable contribution and guidance in preparing the 3D drawings of the flow cell components. I am thankful to Rabiya Javad Awan, a visitor PhD researcher from Lahore University of Management Sciences, Pakistan, for providing the scanning electron microscope image of the stainless steel fibre paper anode gas diffusion layer (Figure 13), which

was taken in the Geoanalytical Electron Microscopy and Spectroscopy (GEMS) facility at the University of Glasgow.

All the experimental data and the data analysis and interpretation of the data in this Chapter are entirely my own work. I wrote the draft paper, then my supervisor edited the manuscript for publication.

Abstract

Anion exchange membrane water electrolysis technology is an environmentally friendly method for hydrogen production without carbon dioxide emissions. The development of this technology is hindered by the sluggish rates of the hydrogen and oxygen evolution reactions, demanding the rational design of electrocatalysts for these processes. Although numerous hydrogen and oxygen evolution electrocatalysts are reported in the literature, there is currently no standard set of conditions or cell design under which they can be tested; variance in testing conditions and water electrolyser components from one study to another therefore hampers a full and coherent comparison of novel electrocatalysts for anion exchange membrane water electrolysis. Herein, a standard water electrolyser test cell was designed and optimised, such that this test cell can be adopted as a universal framework for evaluating novel electrocatalysts (and indeed other cell components) for anion exchange membrane water electrolysis. The performance of this water electrolyser was evaluated using a commercial Pt/C hydrogen evolution reaction electrocatalyst, with an optimised cell found to deliver current densities of 1.41 A $\mathrm{cm^{-2}}$ and 2.74 A $\mathrm{cm^{-2}}$ at cell voltages of 2.0 V and at 60 °C using Fumasep FAA-3-50 and Sustainion® X37-50 membranes, respectively. Guidance for assembling and operating the water electrolyser is provided, along with computer-aided design drawings of the electrolyser and its components to allow others to construct their own identical cells for benchmarking catalysts and other cell components for anion exchange membrane water electrolysis.

3.1. Introduction

Water electrolysers operating at temperatures below 100 °C and at ambient pressure can be divided into zero-gap and finite-gap water electrolysers [1,2]. The terms finite-gap and zero-gap relate to the distance between the membrane/diaphragm separating the cathode and anode electrodes. Zero-gap water electrolysis systems (where the anode and cathode catalysts are in direct contact with the membrane separator, with no interstitial liquid electrolyte between the catalysts) outperform finite-gap water electrolysis systems in terms of performance. For example, at 60 – 80 °C, finite-gap alkaline water electrolysers generally achieve maximal current densities on the order of 0.2 – 0.4 A cm^{-2} compared to zero-gap anion exchange membrane water electrolysers (0.2 – 1.0 A cm^{-2}) and zero-gap proton exchange membrane water electrolysers (0.6 – 2 A cm^{-2}) [3]. The superior performance of zero-gap designs is due in large part to the much lower internal resistance inherent in such cells, which in turn is due to the considerably shorter anode-cathode distances than those found in finite-gap designs. Zero-gap electrolyser designs are therefore seen as a most promising approach for mass production of hydrogen [1,2].

The deployment of anion exchange membrane water electrolysers is seen as especially attractive since nonprecious materials, such as Ni and Fe, can be used due to the less corrosive alkaline environment compared to that found in proton exchange membrane water electrolysers (the latter generally requiring expensive precious metal catalysts) [4]. Nevertheless, the rational design of stable electrocatalysts with high activity towards hydrogen evolution reaction (HER) and oxygen evolution reaction (OER) is still critical due to the sluggish electrode reactions (particularly the OER), which in turn results in a high overpotential requirement. Thus, numerous HER and OER electrocatalysts have been investigated in anion exchange membrane water electrolysers; however, studies to date have operated diverse water electrolysers, with diverse components and with different operating conditions [3]. Consequently, the systematic comparison of different electrocatalysts or other cell components such as membranes and gas diffusion layers is hampered, as there is no universally-accepted benchmark anion exchange membrane electrolyser device to act as a starting point for innovation, with each study instead suggesting its own baseline (where the other cell components beyond those specifically under test may or may not be comparable to those in other studies) [5,6]. Thus, constructing and characterising a benchmark water electrolyser to be adopted in anion exchange membrane water electrolysis research for investigating novel electrocatalysts and other cell components is crucial.

In this study, an anion exchange membrane water electrolyser system was built (Figure 1) using different configurations consisting of stainless steel fibre paper as an anode gas diffusion layer/anode catalyst and two cathode gas diffusion layers, and Fumasep FAA-3-50 or Sustainion® X37-50 Grade RT as the anion exchange membranes. These different configurations were investigated by electrochemical techniques using 1 M KOH, and the performance of the electrolyser was evaluated using a commercial HER (Pt/C) electrocatalyst and using FAA-3-50 and Sustainion X37-50 membranes. Through these efforts, a system consisting of affordable, available, and durable materials was developed as a benchmark anion exchange membrane water electrolyser, to be used as a universal basis for testing electrocatalysts and other cell components, allowing a coherent comparison and evaluation of new anion exchange membrane water electrolyser components. Moreover, the designs of the cell components developed in this study are available as open access computer-aided design (CAD) files, which can be downloaded and modified by the reader from the University of Glasgow's open access data repository. To simplify the design of the standardised flow cell system, two key concessions were made. Although adding ionomer to the anode GDL commonly improves OH^- conductivity through the anode GDL to the catalyst surface and the triple-phase boundary [7,8], this additional step was omitted here to allow direct use of the commercial GDL without further preparation. Moreover, the standardised electrolyser setup lacks a reference electrode, and thus it cannot separate the electrocatalytic activity of the anode and cathode responses. I deliberately avoided the use of a reference electrode in this zero-gap cell, as to do so would considerably complicate the cell design, when my main aim was to offer the community a reliable and accessible test-bed for testing new cell components. Additionally, comparisons between different components (e.g. novel membranes) are still valid since all other cell materials and operating conditions can be kept constant.

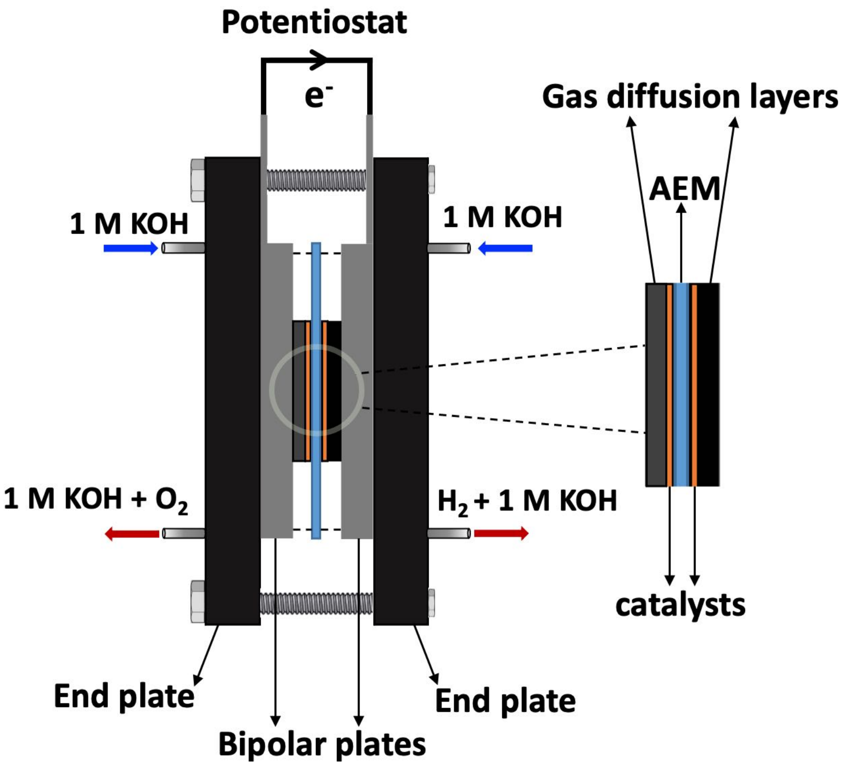

Figure 1: *A schematic illustration of the anion exchange membrane water electrolyser developed in this study. "AEM" = anion exchange membrane.*

3.2. Experimental

3.2.1. Water electrolyser components, setup, and assembly

A flow cell with an active area of 13 cm^2 (3.6 cm × 3.6 cm, although the gas diffusion layers were cut to a size of 3.7 cm × 3.7 cm, to prevent any possible leakage) was assembled as follows with compression force of 5.65 Nm on each bolt. A lower compression force (3.95 Nm) was used, leading to a leakage from the middle of the flow cell, while higher compression forces (7.34 Nm) caused mechanical damage to the membrane. The dimensions of the gas diffusion layers before conducting experiments were confirmed using a digital calliper and a ruler. A pair of titanium plates (thickness: 3 mm) were used as current collectors, each with a serpentine flow design containing six channels through which the electrolytes were supplied to the water electrolyser (and through which the gases evolved were removed). Deionised water (resistivity = 15 MΩ-cm) was used across all experiments for making 1 M KOH solution. This 1 M KOH was supplied to both the anode and the cathode sides simultaneously using two MasterFlex$^{@}$ L/S peristaltic pumps (Cole-Parmer, UK) equipped with two pump heads (Masterflex Easy Load II pump head 77201-60), both using a flow rate of 40 mL min^{-1}. Two commercial membranes, Fumasep FAA-3-50 (supplied by FuelCellStore) and Sustainion® X37-50 Grade RT (supplied by Dioxide Materials) were used as anionic exchange membranes. Stainless steel fibre paper was used as an anode gas diffusion layer. At the cathode, 60% Pt on Vulcan carbon with Nafion dispersion - PTFE-treated (5 wt%) deposited on carbon cloth (W1S1011) or 60% Pt on Vulcan carbon with Nafion dispersion - PTFE-treated (5 wt%) deposited on Sigracet 22 BB carbon paper were used as cathode gas diffusion layers. The Pt loading mass on the carbon-based gas diffusion layers was 0.5 mg cm^{-2}. All the cathode gas diffusion layers were purchased pre-coated with Pt/C catalyst from FuelCellStore, while the stainless steel fibre paper was purchased from Dioxide Materials. The gas diffusion layers can be found on the suppliers' websites as follows: carbon paper (SKU: 11060024) and carbon cloth (SKU: 11060059). Polytetrafluoroethylene (PTFE) gaskets (FuelCellStore) with different thicknesses (0.127 mm, 0.254 mm, and 0.508 mm) were used to prevent liquid electrolyte leakage and any possible direct contact of the bipolar plates. The temperature inside the flow cell was controlled by heating the water reservoirs using hot plates. The internal cell temperature was measured using K-type thermocouples inserted into the outlet and inlet of the cathodic and anodic sides using T-pipe fittings (Stainless steel Swagelok tube fitting, female branch T, 9.53 mm tube outer diameter × 9.53 mm tube outer diameter × 6.35 mm female national pipe thread (NPT)). Temperature measurements were monitored by a Pico TC-08 data logger and PicoLog software. A photography of the water electrolyser setup is shown in Figure 2.

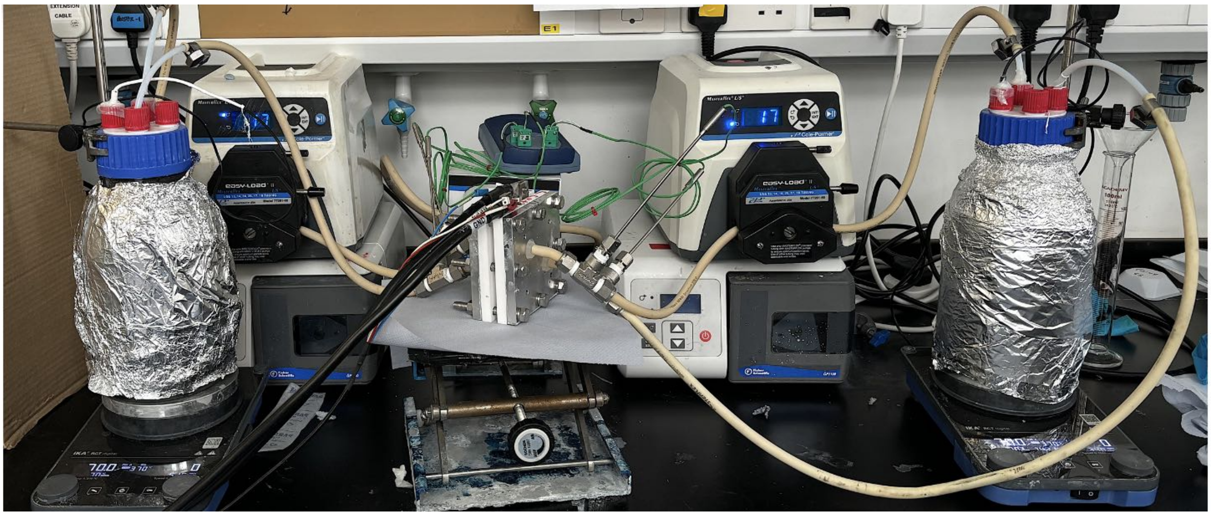

Figure 2: *A photograph of the water electrolyser setup, wherein the supplied 1 M KOH solution (flow rate of 40 mL min^{-1}), placed in two electrolyte reservoirs, was heated using two hotplates (IKA Plate, RCT digital).*

Guidance for assembling and operating the flow cell are shown in the Figure 3 – 8, and the technical specifications of the gas diffusion layers and membranes are provided in Table 1.

Table 1: *The technical specifications of the cathode and anode gas diffusion layers and anion exchange membranes, as given by the manufacturers.*

	Sigracet 22 BB carbon paper	**Carbon Cloth (W1S1011)**	**Stainless steel fibre paper**	**Fumasep FAA-3-50**	**Sustainion X37-50**
Material Type	Fibre paper	Cloth	Fibre paper	Polymer	Polymer
Thickness	0.215 +/- 0.02 mm	0.410 +/- 0.015 mm	0.67 mm	45 - 55 µm	50 µm
Electrical Resistivity	< 10 mΩcm^2	< 13 mΩcm^2	NA	NA	NA
PTFE Treatment	5%	5%	No	No	No
Microporous Layer (MPL)	Yes, on one side	Yes, on one side	No	NA	NA

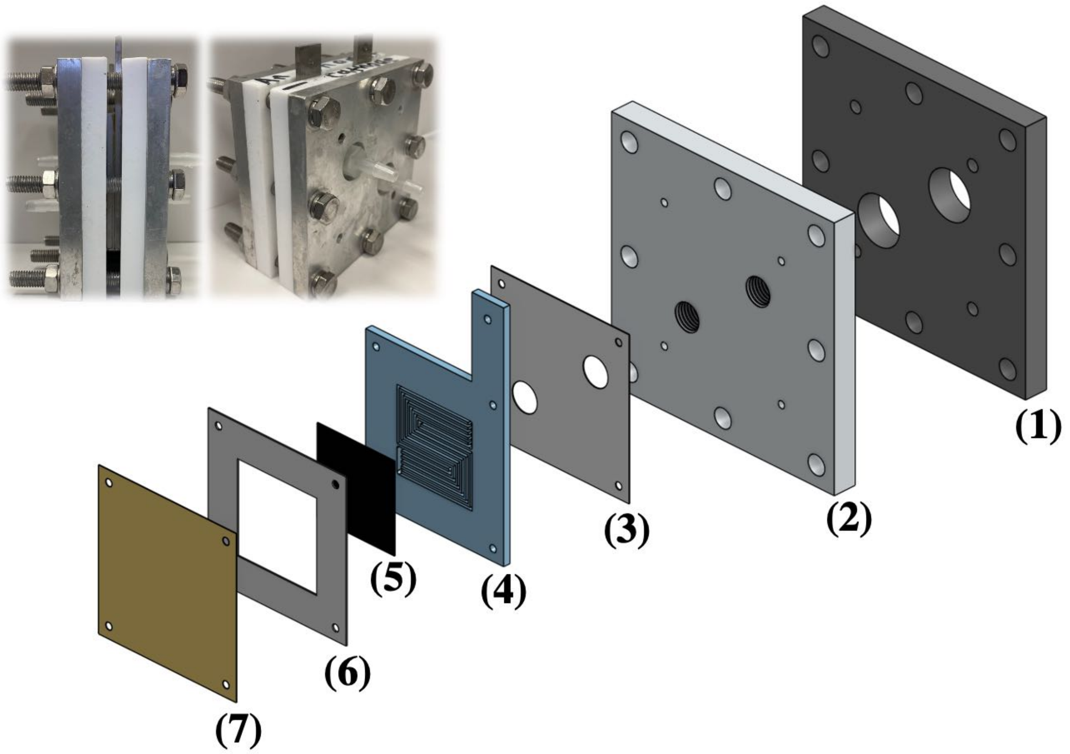

***Figure 3:** The components of one side of the flow cell: (1) aluminium end plate, (2) polytetrafluoroethylene (PTFE) insulating plate, (3) PTFE insulating gasket, (4) Ti (Grade 2) bipolar plate, (5) gas diffusion layer, (6) other PTFE gasket, (7) anion exchange membrane. Assemble the flow cell components following the order shown in Figure 6, ensuring the inlets and outlets are properly aligned. Use gaskets that are 25 – 40% thinner than the gas diffusion layers to ensure good contact with the membrane and to prevent leakage: stainless steel fibre paper (gasket thickness: 0.508 mm), carbon cloth (gasket thickness: 0.254 mm), and Sigracet carbon paper (gasket thickness: 0.127 mm). The assembly sequence is as follows: (1) end plate, (2) insulating plate, (3) gasket (between insulating and bipolar plates), (4) bipolar plate, (5) gasket (between bipolar plate and membrane), (6) gas diffusion layer, (7) membrane, (8) gas diffusion layer, (9) gasket (between bipolar plate and membrane), (10) bipolar plate, (11) gasket (between bipolar and insulating plates), (12) insulating plate, and (13) end plate. Gaskets can be printed using CAD files (#3 and #5) or manually cut using templates (#8 and #9).*

***Figure 4:** Wrapping PTFE tape on four polypropylene hose barbs/fittings (Masterflex fitting, polypropylene, straight, hose barb to threads; size: 6.35 mm inner diameter × 6.35 mm national pipe thread (NPT) (M)).*

***Figure 5:** Attaching the four tube fittings into four PTFE insulating plate.*

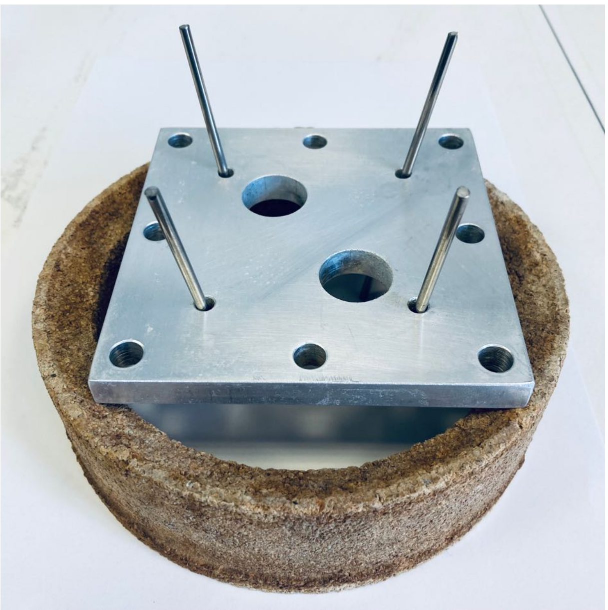

Figure 6: *Placing an end plate on a cork ring and 4 guide rods for assembly, avoiding the displacement of the flow cell components, which might otherwise cause leakage during operation.*

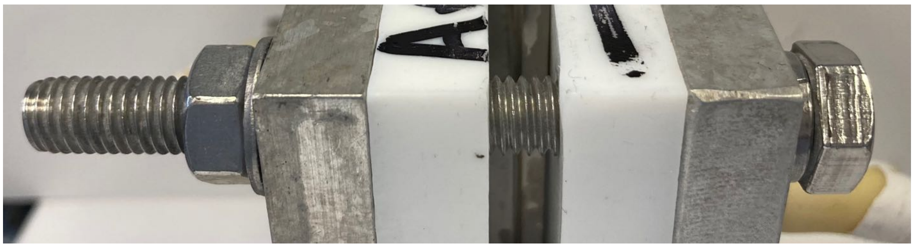

Figure 7: *Placing washers on eight M8 (8 mm × 75 mm) hex bolts (fully threaded setscrew) and put them in position around the cell. At the end of each bolt, place another washer and a nut. Ensure that the torque wrench is set to 5.65 Nm and attach the size 13 fitting. Use a spanner and torque wrench to tighten each bolt. The wrench will click when each bolt is torque-tightened to 5.65 Nm.*

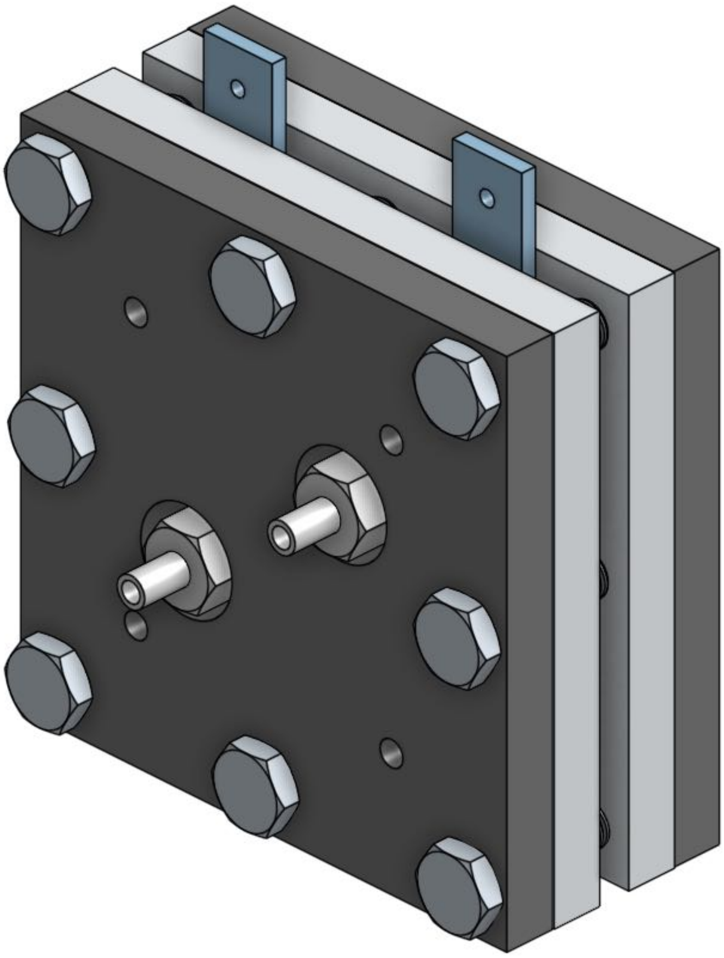

***Figure 8:** A diagram of the fully-assembled flow cell developed in this work.*

Furthermore, computer-aided design (CAD) drawing files of the water electrolyser components were generated to allow other researchers to manufacture an identical water electrolyser. These are available for open access download at https://researchdata.gla.ac.uk/1672/. The dimensions (in mm) of the three major flow cell components (end, insulating, and bipolar plates) modelled by computer-aided design are provided in the following 2D line drawings (Figure 9 – 11), so that these measurements can be used for manufacturing these parts. The thickness of these components is not as critical as the dimensions that are shown. In this work, the thicknesses of these components were as follows: the thickness of both end plates and PTFE insulating plates is 10 mm, whereas the thickness of the bipolar plates is 3 mm.

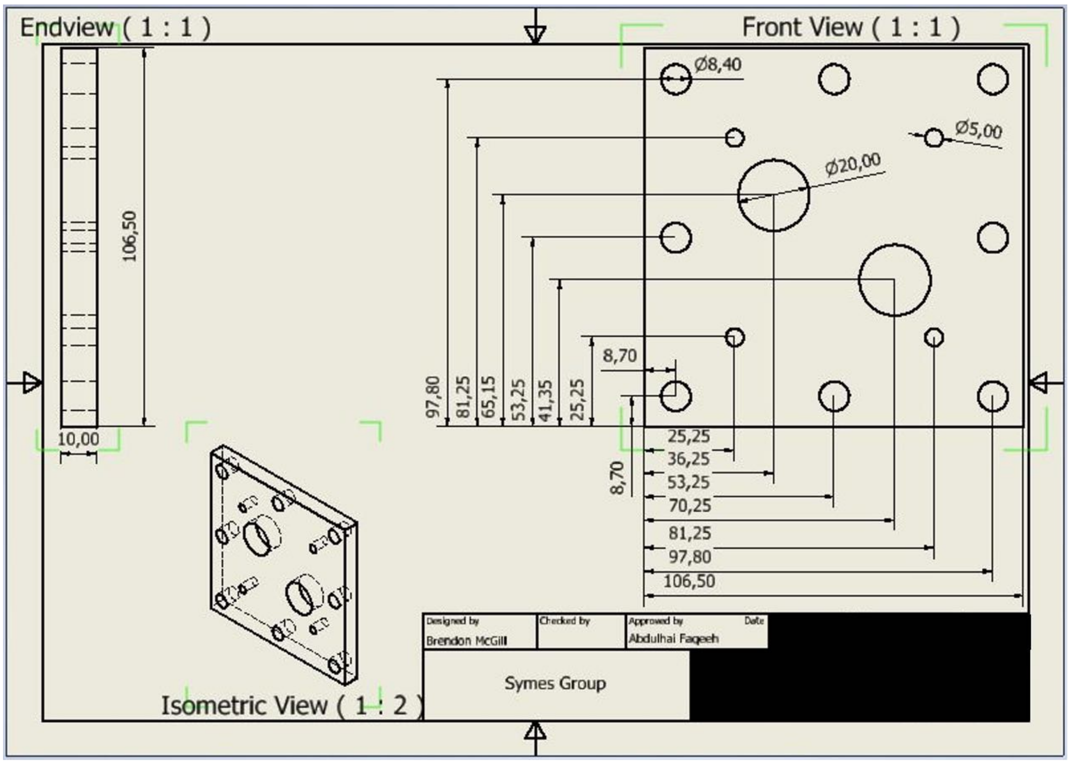

Figure 9: *The dimensions of the aluminium end plate.*

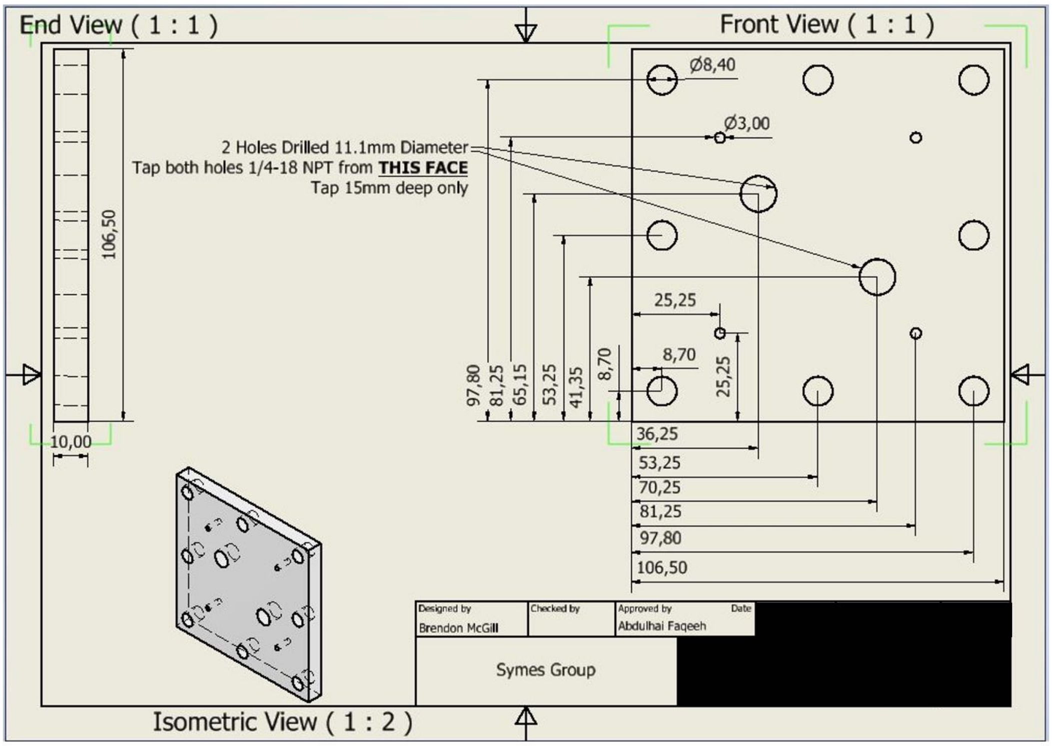

Figure 10: *The dimensions of the PTFE insulating plate.*

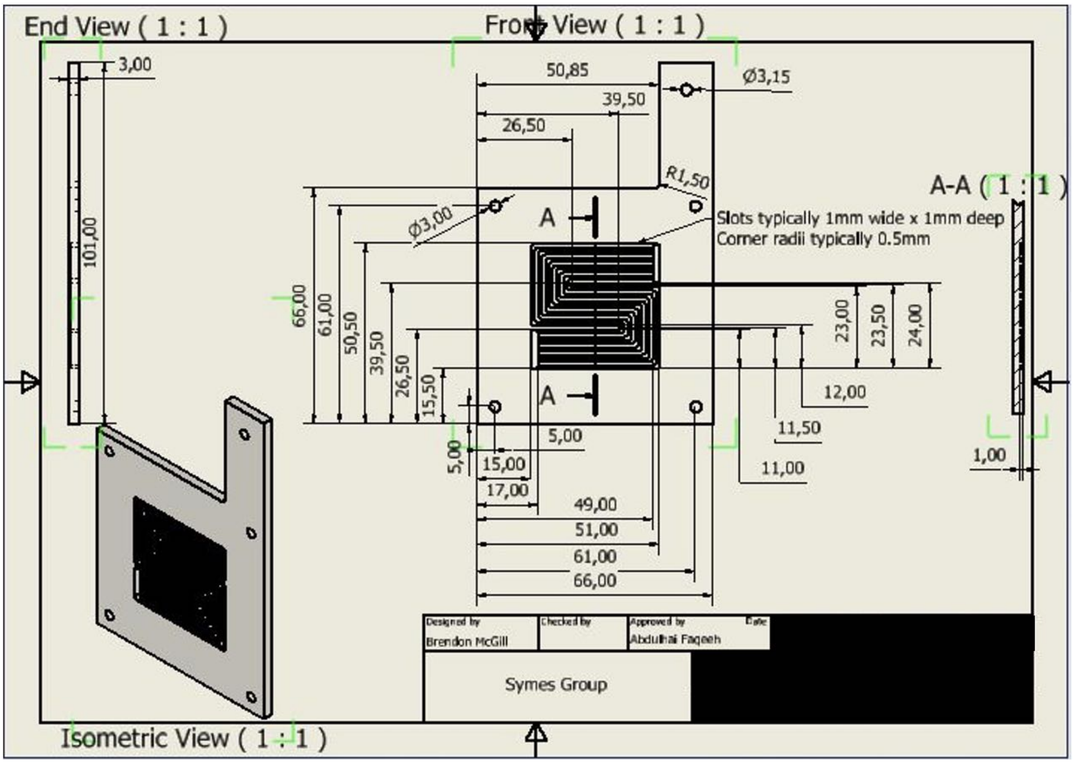

Figure 11: *The dimensions of the Ti (Grade 2) bipolar plate.*

3.2.2. Electrolyte characterisation

Any leached metal residuals were detected in the electrolyte reservoirs using inductively coupled plasma optical emission spectroscopy (ICP-OES) after each stability test; after neutralising the 1 M KOH electrolytes with HNO_3 and diluting them 5-fold with 5% HNO_3. The ICP-OES samples were collected from the catholyte and anolyte with volumes of 0.85 L and 0.6 L circulating in the cell, respectively. The ICP-OES was performed using an Agilent 5900 ICP-OES, equipped with an Agilent SPS4 autosampler.

3.2.3. Anion Exchange Membrane Preparation

The Fumasep FAA-3-50 and Sustainion X37-50 membranes were delivered in a dry form and were pre-treated before use, following the manufacturers' instructions. The membranes were submerged in 1 M KOH at room temperature (around 20 °C) for at least 24 h to convert them into the OH-form. They were stored under 1 M KOH in closed containers to prevent dryness and CO_2 contamination, in which CO_3^{2-} formation might influence the ionic conductivity.

3.2.4. Electrochemical characterisation

All the electrochemical tests were conducted using the above-mentioned flow cell at 60 °C (unless otherwise mentioned), with a flow rate of 40 mL min^{-1}, using a BioLogic SP-150 potentiostat with an 80 A booster. The data were acquired and analysed using EC-Lab$^{@}$ software (version 11.43). In addition, the assembled flow cell and components were subject to a pre-treatment prior to collecting data on each membrane electrode assembly configuration by applying a fixed potential of 2.0 V for 1 h at 40 °C.

The polarisation curves were measured over a potential range of 0 V to 2.0 V at a scan rate of 10 mV s^{-1}, and the chronopotentiometric tests were performed at 1.0 A cm^{-2} at 60 °C.

The electrochemical impedance spectroscopy analysis was performed under the experimental parameters shown in Table 2. The Nyquist plots generated by the electrochemical impedance spectroscopy measurements were fitted using an equivalent circuit model (Figure 12), which was applied according to the methods developed in the literature [9–12]. In the equivalent circuit, L1 (inductor) refers to the connectors and cables used while taking measurements, R1 represents the ohmic resistance of the flow cell components, R2 and R3 depict the cathodic and anodic charge transfer resistances, respectively, and the Q2 and Q3 represent the constant phase elements of the cathodic and anodic processes, respectively.

Table 2: *The experimental parameters used in the electrochemical impedance spectroscopy.*

DC Potential (V)	2.0
AC Potential (mV rms)	100
Initial Frequency (kHz)	10
Final Frequency (mHz)	500
Points/Decade	6.0

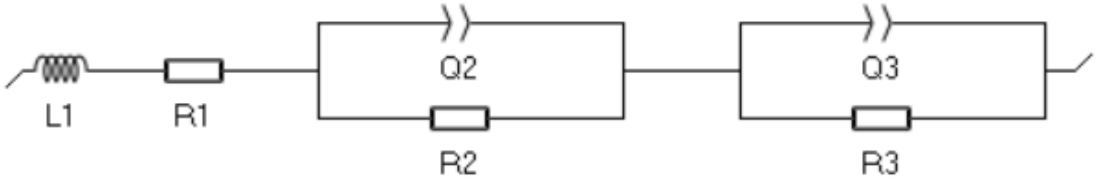

Figure 12: *The equivalent circuit model used in the electrochemical impedance spectroscopy analysis. Circuit components are defined in the main text.*

3.3. Results and discussion

3.3.1. Characterisation of the generic alkaline water electrolyser

The water electrolyser performance was evaluated using stainless steel fibre paper and 0.5 mg cm^{-2} Pt/C, with 5 wt% PTFE, 35% Vulcan carbon, and Nafion dispersion as an ionomer binder, deposited on two different cathode gas diffusion layers: carbon cloth and Sigracet carbon paper, which were both purchased pre-coated with Pt/C catalyst. The carbon-based gas diffusion layers were selected based on their broad commercial availability, both with and without Pt/C as a hydrogen evolution catalyst. This allows others to either purchase a catalyst pre-coated substrate or uncoated substrate to deposit their own catalyst onto the same commercially available substrate. Additionally, the stainless steel-based gas diffusion layer, with a high fibrous and porous structure (Figure 13), was used due to its wide commercial availability, high durability and catalytic activity towards oxygen evolution reaction [13–15]. The use of Nafion as an ionomer binder in anion exchange membrane water electrolysis has considerable precedent [16–19]. A Fumasep FAA-3-50 membrane was employed. As shown in Figure 16a, excellent overall high performance was achieved using both cathode gas diffusion layers. The Pt deposited on carbon cloth configuration (1.41 A cm^{-2} at 2.0 V cell potential and at 60 °C) outperformed the Pt deposited on Sigracet carbon paper configuration (1.24 A cm^{-2} at 2.0 V cell potential and at 60 °C). The difference in performance between the two configurations was attributed to the physical structure of the two gas diffusion layers. At high current densities, the carbon paper-based gas diffusion layers show inferior performance compared to the carbon cloth-based gas diffusion layers due to the smoother non-woven torturous structure of carbon papers when compared with the woven structure of carbon cloth (Figure 14) [20].

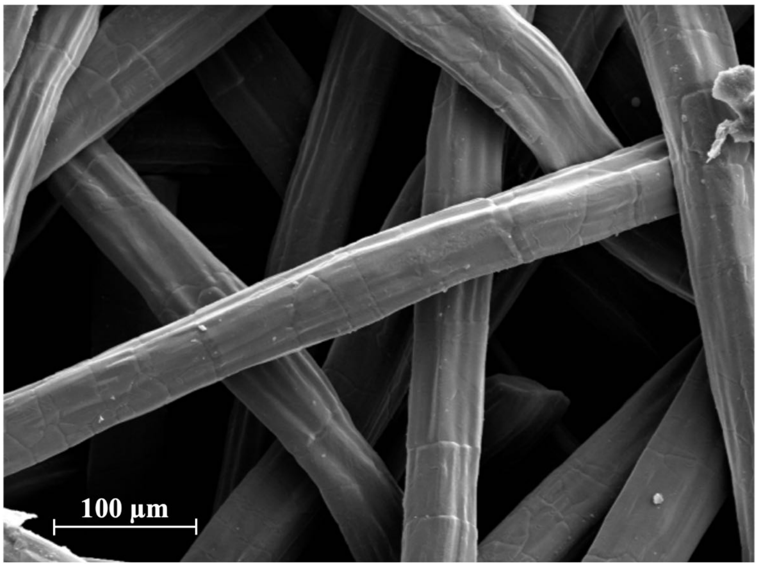

Figure 13: *Scanning electron microscope image of the top-surface of the stainless steel fibre paper anode gas diffusion layer used in this work.*

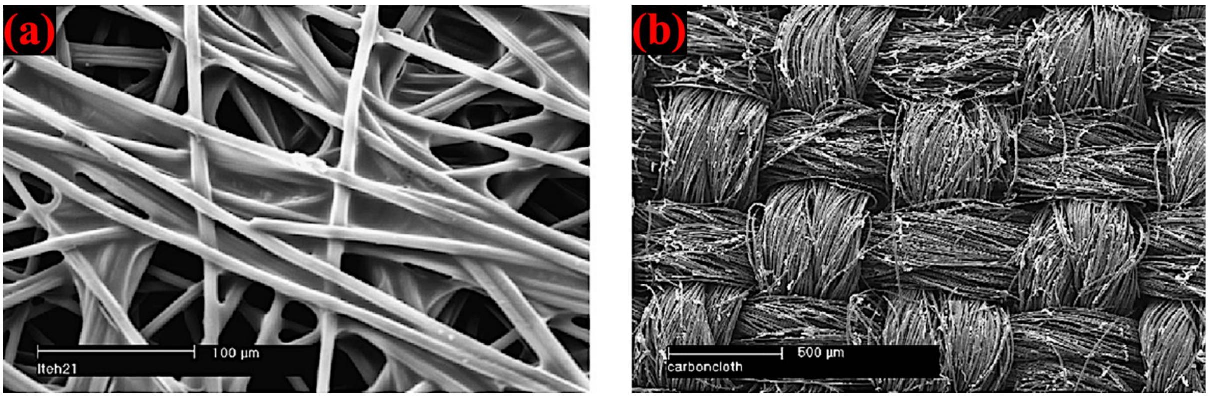

Figure 14: *Scanning electron microscope images of (a) a carbon paper and (b) a carbon cloth gas diffusion layers. Reprinted (adapted) with permission from [20]. Copyright 2007 Elsevier.*

Wang *et al.* observed larger water droplets (~ 200 µm) on the surface of a carbon paper compared to the water droplets (~ 10 µm) on the surface of carbon cloth in an operating polymer electrolyte fuel cell at 0.8 A cm^{-2} (Figure 15). The smoother and more tortuous structure of carbon paper led to more mass transport limitations due to issues with removing water and gases, leading to higher water coverage on the surface and bubble formation, blocking the catalyst active sites [20].

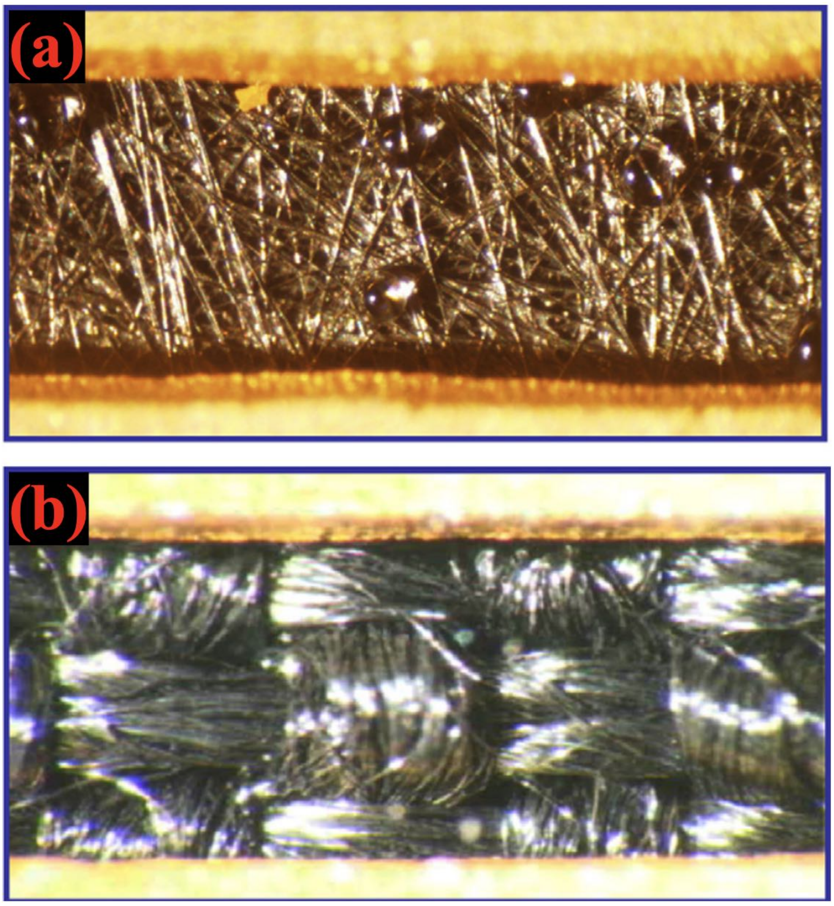

Figure 15: *In-situ images of water droplets on the surface of (a) a carbon paper and (b) a carbon cloth gas diffusion layers in an operating polymer electrolyte fuel cell at 0.8 A cm^{-2} and 60 °C. Reprinted (adapted) with permission from [20]. Copyright 2007 Elsevier.*

The electrochemical impedance spectroscopy analysis of both configurations was conducted in the potentiostatic mode at 2.0 V using a varied frequency from 10 kHz to 500 mHz (6 points per decade) with a sinusoidal excitation signal of 100 mV rms. As shown in the Nyquist plot (Figure 16b), the electrochemical impedance spectroscopy analysis agreed with the linear sweep voltammetry results. The configuration where carbon cloth was used as the cathode gas diffusion layer achieved slightly lower ohmic resistance (~ 211 mΩ cm^2) compared to the configuration using Sigracet carbon paper (~ 227 mΩ cm^2). The cathodic and anodic charge transfer resistances achieved by the configuration using carbon cloth were lower than using Sigracet carbon paper as well; 1.07 mΩ cm^2 (carbon cloth) and 1.16 mΩ cm^2 (Sigracet carbon paper), and 30.7 mΩ cm^2 (carbon cloth) and 55.3 mΩ cm^2 (Sigracet carbon paper), respectively.

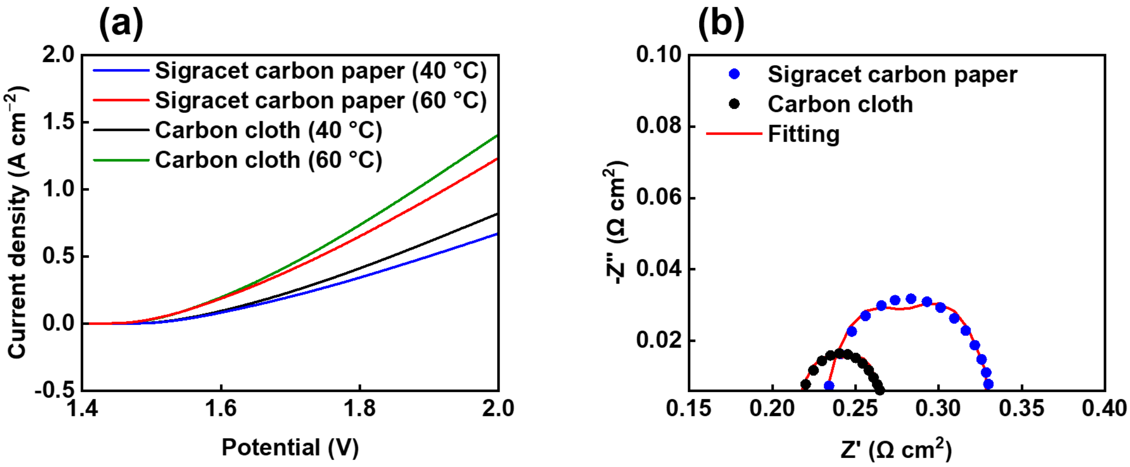

Figure 16: *(a) Polarisation curves and (b) Nyquist plots (at 60 °C only) of the water electrolyser using stainless steel fibre paper at the anode and 0.5 mg cm^{-2} Pt/C deposited on two different cathode gas diffusion layers: carbon cloth and Sigracet carbon paper. A Fumasep FAA-3-50 membrane was used.*

As discussed in Chapter 1, three major losses (i.e. overpotentials) dominate the shape of polarisation curves in water electrolysers: kinetic losses attributed to HER and OER activation overpotentials, ohmic losses due to ionic and electronic conduction, and concentration losses caused by mass transport limitations [21]. According to Figure 16a, the potentials required to achieve 1 A cm^{-2} at 60 °C for carbon cloth were 1.88 V and 1.92 V for carbon paper, before iR compensation (i.e. the ohmic losses were included). The iR-corrected potentials were obtained by subtracting the ohmic potential drops from the measured potentials using the ohmic resistances measured by EIS at 2.0 V: 0.23 Ω cm^2 (carbon paper) and 0.21 Ω cm^2 (carbon cloth). As these ohmic resistances were measured at a single potential of 2.0 V, it was assumed that the ohmic resistances remain approximately constant at potentials near 2.0 V. The potential difference between the two substrates reduced from ~ 40 mV, before iR compensation, to ~ 20 mV, after iR compensation, reflecting a portion of potential difference between the two substrates was attributed to the ohmic resistance. The remaining difference was likely due to intrinsic performance variations associated with structural factors affecting the mass transport, where higher mass transport loss was generated for carbon paper due to its higher tortuosity [20].

The stability of the water electrolyser was evaluated by a galvanostatic electrolysis at 1.0 A cm^{-2} for 25 h at 60 °C (Figure 17). An increase in the required cell potential from 1.97 V to 2.14 V (Sigracet carbon paper) and from 1.92 V to 2.07 V (carbon cloth) was observed. The increase in the required cell potential most likely occurred due to a passivation layer formed on the stainless steel gas diffusion layer surface over time. This layer decreased the electrical conductivity of the interface between the stainless steel fibre paper and the membrane (i.e. the electrolyte) [22], as confirmed by an electrochemical impedance spectroscopy measurement taken before and after testing Sustainion X37-50 membrane (Figure 20).

Effects on the cell's performance by more extensive corrosion of the stainless steel was excluded since consistently low Fe content (0.009 – 0.012 mg cm^{-2}) were detected by ICP-OES in the anolyte streams of all the various configurations, with no detectable Ni content in these anolytes. No Pt content was detected in the catholytes, indicating the excellent stability of Pt attachment to the carbon cloth and Sigracet carbon paper. The exact metal contents detected in the electrolyte solutions are shown in Table 3, where the ICP-OES samples were collected from the catholyte and anolyte with volumes of 0.85 L and 0.6 L circulating in the cell, respectively.

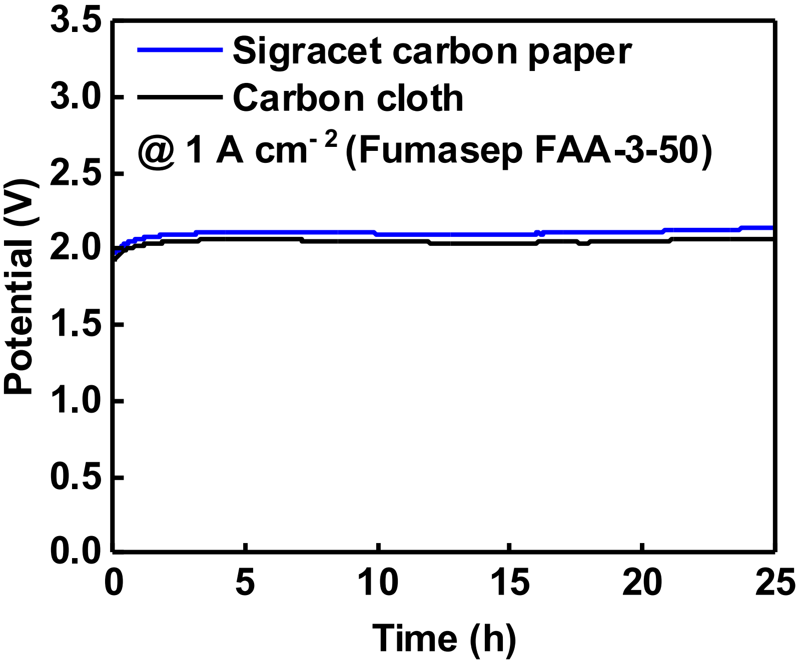

Figure 17: *The chronopotentiometric evaluation of the water electrolyser at 1.0 A cm*$^{-2}$ *using stainless steel fibre paper as the anode catalyst and 0.5 mg cm*$^{-2}$ *Pt/C deposited on two different gas diffusion layers at the cathode at 60 °C. A Fumasep FAA-3-50 membrane was used.*

3.3.2. The effect of the membrane on the water electrolyser

The performance of the water electrolyser with a different membrane was evaluated employing the same aforementioned two configurations but using the Sustainion X37-50 membrane instead of Fumasep FAA-3-50 as the anion exchange membrane. As shown in the polarisation curves (Figure 18a), the performance of the configuration using Pt deposited on carbon cloth (2.74 A cm^{-2} at 2.0 V cell potential and at 60 °C) gave superior performance compared to that obtained using the Pt deposited on Sigracet carbon paper (2.13 A cm^{-2} at 2.0 V cell potential and at 60 °C).

As shown in the Nyquist plot (Figure 18b), lower ohmic resistance was obtained by using the carbon cloth configuration (~ 124 mΩ cm^2) than the Sigracet carbon paper configuration (~ 132 mΩ cm^2). The cathodic and anodic charge transfer resistances achieved were 0.84 mΩ cm^2 (carbon cloth) and 0.94 mΩ cm^2 (Sigracet carbon paper) and 17.1 mΩ cm^2 (carbon cloth) and 27.5 mΩ cm^2 (Sigracet carbon paper), respectively; agreeing with the linear sweep voltammetry results.

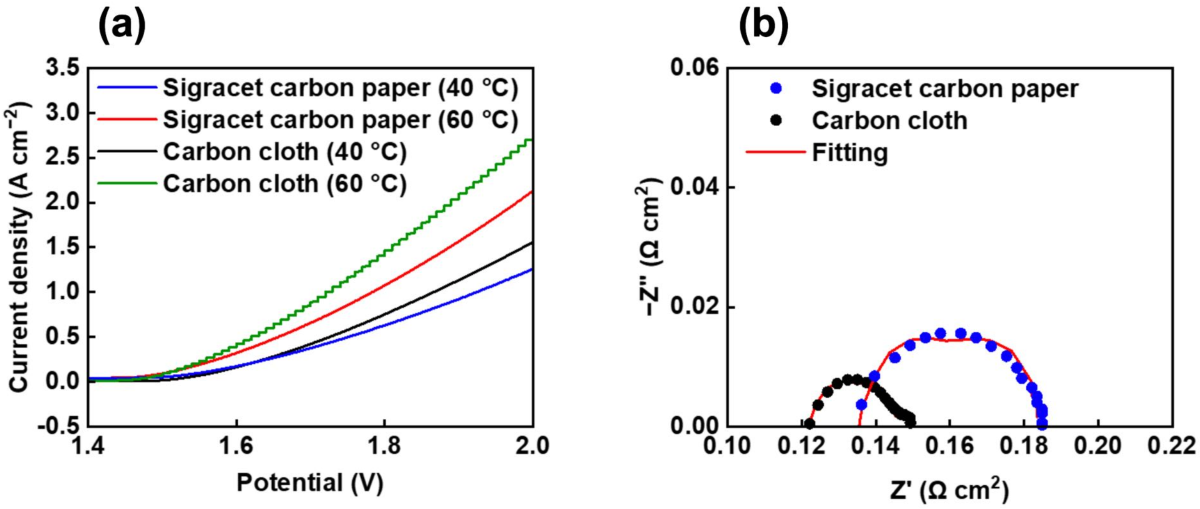

Figure 18: *(a) Polarisation curves and (b) Nyquist plots (at 60 °C only) of the water electrolyser using a Sustainion X37-50 membrane, stainless steel fibre paper at the anode and 0.5 mg cm^{-2} Pt/C deposited on two different cathode gas diffusion layers: carbon cloth and Sigracet carbon paper.*

The effect of using a Sustainion membrane on the water electrolyser's stability was investigated by a galvanostatic electrolysis at 1.0 A cm^{-2} for 25 h using the Sigracet carbon paper configuration (Figure 19a) and a longer test for 205 h using the carbon cloth configuration (Figure 19b), since this configuration achieved the best performance. Both tests were conducted at 60 °C. In the stability test of the Sigracet carbon paper configuration, the potential required cell potential to deliver 1.0 A cm^{-2} increased from an initial 1.79 V to 2.01 V at 25 h. Meanwhile, for the carbon cloth configuration, the required cell potential to deliver 1.0 A cm^{-2} increased from 1.78 V and stood at a peak of 2.10 V after 205 h. As confirmed by ICP-OES analysis of the electrolytes employed in both configurations after each stability test, the Fe content was around 0.009 – 0.015 mg cm^{-2}. The contents of Ni in the anolyte and Pt in the catholyte were below the detection limit of the ICP-OES instrument (0.02 mg L^{-1}) after the stability test of both configurations. The contents detected by the ICP-OES were like the contents detected in the cases where the FAA-3-50 membrane was used, indicating a consistent effect on the water electrolyser performance by the anode gas diffusion layer (i.e. the stainless steel fibre paper). The exact metal content detected in the electrolyte solutions are shown in Table 3.

Table 3: *The Fe and Ni content detected in the anolyte and Pt content detected in the catholyte, after stability tests for 25 h (except * for 205 h) at a fixed current density of 1.0 A* cm^{-2} *at 60 °C. The Fe values were calculated by accounting for the volume of electrolytes circulating in the cell upon sample collection (catholyte = 0.85 L and anolyte = 0.6 L), then normalised to the geometric area of the GDLs (13.7* cm^{-2}*).*

Membrane	Cathode electrode	Fe content in anolyte (mg cm^{-2})	Ni content in anolyte (mg L^{-1})	Pt content in catholyte (mg L^{-1})
Fumasep FAA-3-50	Carbon paper	0.011	< 0.02	< 0.02
Fumasep FAA-3-50	Carbon cloth	0.012	< 0.02	< 0.02
Sustainion X37-50	Carbon paper	0.009	< 0.02	< 0.02
Sustainion X37-50*	Carbon cloth*	0.015	< 0.02	< 0.02

Again, the increase in cell voltage required to maintain a current density of 1.0 A cm^{-2} can be attributed to the decrease in the electrical conductivity at the anode side caused by passivation of the stainless steel gas diffusion layer. The drop in electrical conductivity was confirmed by performing electrochemical impedance spectroscopy analysis after the stability test for 205 h (Figure 20) and comparing this to the ohmic resistance of the system before (124 mΩ cm^2) and after (232 mΩ cm^2) electrolysis. Over longer electrolysis durations, however, stainless steel substrates in alkaline media show excellent electrocatalytic activity towards OER, since such substrates develop a rich metal oxide layer composed of mixed oxides of Ni, Fe and Cr, acting as OER active sites, at high anodic potential under OER operation, as reported in the literature [14]. Consequently, the effects of passivation on the surface of stainless steel fibre paper seem to be offset somewhat over longer-term stability tests.

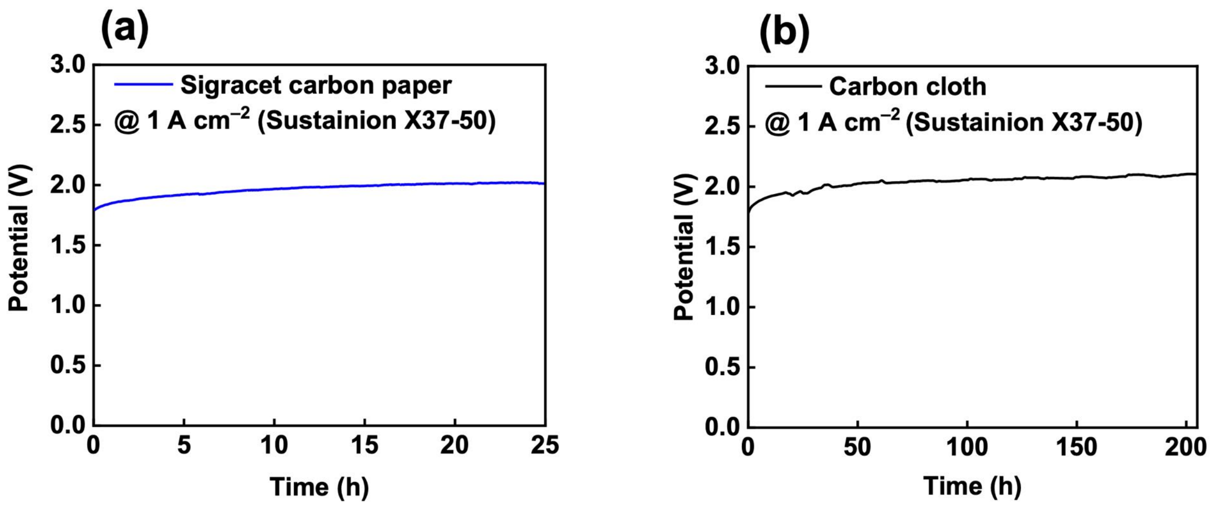

Figure 19: *The chronopotentiometric evaluation of the water electrolyser at 1.0 A* cm^{-2} *using a Sustainion X37-50 membrane, stainless steel fibre paper as the anode catalyst, and 0.5 mg* cm^{-2} *Pt/C deposited on (a) Sigracet carbon paper and (b) carbon cloth at 60 °C.*

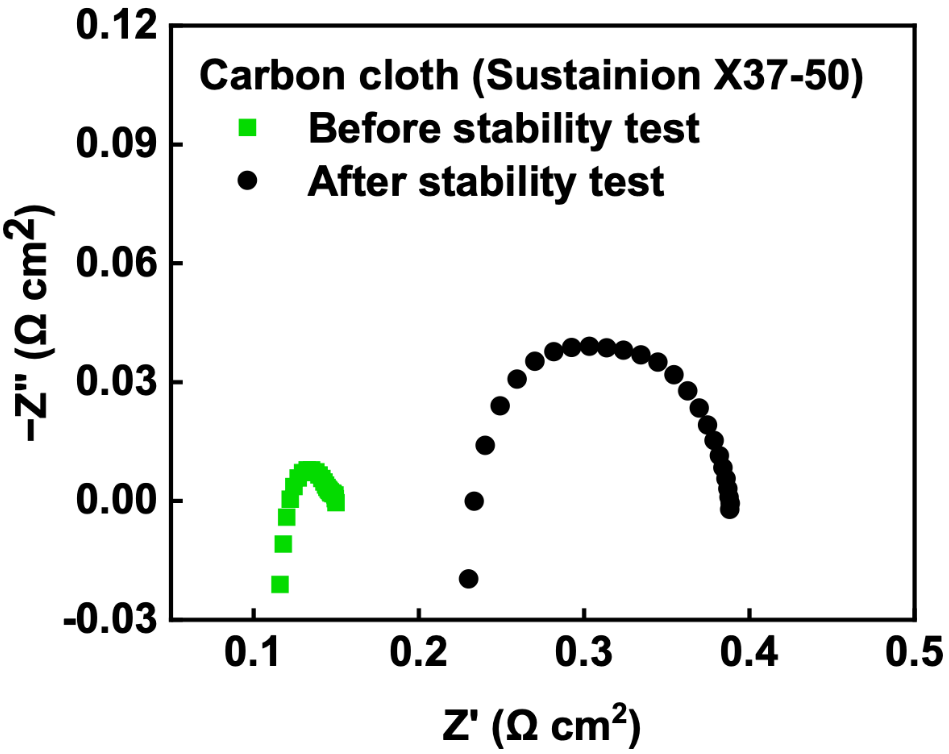

Figure 20: *Nyquist plots of the water electrolyser before and after electrolysis for 205 h at 1.0 A* cm^{-2} *and at 60 °C using a Sustainion X37-50 membrane, stainless steel fibre paper at the anode side, and 0.5 mg* cm^{-2} *Pt/C deposited on carbon cloth.*

According to the combined linear sweep voltammetry, electrochemical impedance spectroscopy, and stability tests results, using the Sustainion membrane allowed higher current densities to be achieved, with lower resistances, and longer stability. The Sustainion X37-50 membrane achieved the required combination of high current densities and stable performance. This higher performance can be attributed to the higher OH^- conductivity of the Sustainion membrane of 115 mS cm^{-1} at 60 °C compared to the OH^- conductivity of FAA-3-50 of 55 mS cm^{-1} at 100 °C [23,24]. Although higher performance was obtained using the Sustainion membrane, it must be noted that the Fumasep FAA-3-50 membrane is a cost-effective alternative for short-term tests, since the price of the FAA-3-50 membrane ($74.00 for 20 cm × 30 cm) is almost four times lower than the price of Sustainion® X37-50 membrane ($255.00 for 22 cm × 28 cm) at time of writing. However, for long-term stability tests (> 24 h), it is recommended to use the Sustainion membrane due to its superior durability [19,25].

Although the aim here was to detail the construction and characterisation of a test-bed that others can use to compare novel materials rather than reporting record performance, a comparison of performance achieved by different water electrolysers reported in Table 4 can be made. However, such comparison is not coherent due to the variety in the cell components and testing conditions adopted in these papers. For instance, 1 M KOH was used as the standard liquid electrolyte in all these papers, yet it was circulating into the water electrolysers with various flow rates, affecting the ohmic and charge transfer resistances [26]. As shown in Table 4, higher performance was achieved using IrO_2 and Pt/C catalysts and Sustainion X37-50 membrane, as expected, due to the higher catalytic activity of these precious metal catalysts and the higher OH^- conductivity of the Sustainion membrane [23]. Notably, all the catalysts reported in these papers were prepared in-house, then deposited by spray-coating technique, while the catalysts used in this work were commercially available, increasing the reproducibility.

Table 4: *Comparison of the performance of various anion exchange membrane water electrolysers at 60 °C using 1 M KOH (unless otherwise mentioned).*

Anion exchange membrane	**Anode (catalyst loading: mg cm^{-2})**	**Cathode (catalyst loading: mg cm^{-2})**	**Current density (A cm^{-2})**	**Ref**
Sustainion X37-50	Stainless steel fibre paper	Pt/C (0.5)	2.74 at 2.0 V	**This work**
FAA-3-50	Stainless steel fibre paper	Pt/C (0.5)	1.41 at 2.0 V	**This work**
FAA-3-50	IrO_2 (4)	Pt/C (0.4)	1.5 at 1.9 V *	[27]
FAA-3-50	IrO_2 (2)	Pt/C (2)	1.0 at 2.15 V	[28]
Sustainion Grade T	IrO_2 (2)	Pt/C (0.5)	1.8 at 2.0 V	[29]
Sustainion X37-50	$NiFe_2O_4$ (2)	NiFeCo (2)	1.0 at 1.9 V	[19]
Sustainion X37-50	$NiFe_2O_4$ (1.8)	Raney Ni (2.7)	0.744 at 1.8 V	[30]
Sustainion Grade T	$NiFe_2O_4$ (1.8)	Raney Ni (14.5)	0.84 at 1.8 V	[30]
Sustainion X37-50	$NiFe_2O_4$ (2)	NiFeCo (3)	1.0 at 1.9 V	[31]

Sustainion X37-50	IrO_2 (N/A)	Pt/C (N/A)	1.0 at 1.63 V	[31]

* At 70 °C.

3.4. Conclusions and future directions

Herein, an anion exchange membrane water electrolyser was constructed and optimised as a universal benchmark for testing new electrocatalysts and other cell components in a standardised fashion. When using stainless steel fibre paper as a combined anode gas diffusion layer and OER electrocatalyst and Pt/C as an HER electrocatalyst, the benchmark water electrolyser showed excellent performance of 2.74 A cm^{-2} (using Sustainion® X37-50 membrane) and 1.41 A cm^{-2} (using Fumasep FAA-3-50 membrane) at 2.0 V and at 60 °C using carbon cloth. The water electrolyser showed a moderate decline in performance over extended duration testing, which was primarily attributed to the formation of a mixed-oxide passivation layer on the stainless steel fibre paper surface over extended time under high anodic polarisation, decreasing the electrical conductivity of the stainless steel fibre paper. As a way of adopting this flow design by others, numerous flow cells of this design was mass machined by an industrial party for distribution purposes. For instance, a flow cell (with all the required materials) was sent to a research group at RWTH Aachen University, Germany. They reproduced our results, although they were unable to complete the full 205 h stability test, initially due to lack of the safety equipment (e.g. hydrogen gas sensor), and later because their potentiostat with sufficient capacity (minimum 13.7 A) became unavailable (at time of writing).

Further work to aid in the standardisation of procedures for anion exchange membrane water electrolysers that should be addressed include optimisation of electrocatalyst deposition on gas diffusion layers or membranes. Together with the present study, such standardisation will enable innovation in, and proper comparison of, anion exchange membrane water electrolysers for the mass production of hydrogen in a sustainable manner.

References

[1] N. Du, C. Roy, R. Peach, M. Turnbull, S. Thiele, C. Bock, Anion-Exchange Membrane Water Electrolyzers, Chem. Rev. 122 (2022) 11830–11895, https://doi.org/10.1021/acs.chemrev.1c00854.

[2] R. Phillips, C.W. Dunnill, Zero gap alkaline electrolysis cell design for renewable energy storage as hydrogen gas, RSC. Adv. 6 (2016) 100643–100651, https://doi.org/10.1039/c6ra22242k.

[3] H.A. Miller, K. Bouzek, J. Hnat, S. Loos, C.I. Bernäcker, T. Weißgärber, L. Röntzsch, J. Meier-Haack, Green hydrogen from anion exchange membrane water electrolysis: a review of recent developments in critical materials and operating conditions, Sustain. Energy Fuels 4 (2020) 2114–2133, https://doi.org/10.1039/c9se01240k.

[4] M. Carmo, D.L. Fritz, J. Mergel, D. Stolten, A comprehensive review on PEM water electrolysis, Int. J. Hydrogen Energy 38 (2013) 4901–4934, https://doi.org/10.1016/j.ijhydene.2013.01.151.

[5] H.A. Miller, Green hydrogen from anion exchange membrane water electrolysis, Curr. Opin. Electrochem. (2022) 101122, https://doi.org/10.1016/j.coelec.2022.101122.

[6] R.R. Raja Sulaiman, W.Y. Wong, K.S. Loh, Recent developments on transition metal–based electrocatalysts for application in anion exchange membrane water electrolysis, Int. J. Energy Res. (2021) 1–36, https://doi.org/10.1002/er.7380.

[7] N. Chen, Y.M. Lee, Anion exchange polyelectrolytes for membranes and ionomers, Prog. Polym. Sci. 113 (2021) 101345, https://doi.org/10.1016/j.progpolymsci.2020.101345.

[8] E. Cossar, F. Murphy, J. Walia, A. Weck, E.A. Baranova, Role of Ionomers in Anion Exchange Membrane Water Electrolysis: Is Aemion the Answer for Nickel-Based Anodes?, ACS Appl. Energy Mater. 5 (2022) 9938–9951, https://doi.org/10.1021/acsaem.2c01604.

[9] A.Y. Faid, A.O. Barnett, F. Seland, S. Sunde, Tuning Ni−MoO_2 Catalyst-Ionomer and Electrolyte Interaction for Water Electrolyzers with Anion Exchange Membranes, ACS Appl. Energy Mater. 4 (2021) 3327–3340, https://doi.org/10.1021/acsaem.0c03072.

[10] S. Siracusano, S. Trocino, N. Briguglio, V. Baglio, A.S. Aricò, Electrochemical impedance spectroscopy as a diagnostic tool in polymer electrolyte membrane electrolysis, Materials 11 (2018) 1368, https://doi.org/10.3390/ma11081368.

[11] S. Siracusano, V. Baglio, F. Lufrano, P. Staiti, A.S. Aricò, Electrochemical characterization of a PEM water electrolyzer based on a sulfonated polysulfone membrane, J. Memb. Sci. 448 (2013) 209–214, https://doi.org/10.1016/j.memsci.2013.07.058.

[12] X. Min, Y. Shi, Z. Lu, L. Shen, T.O. Ogundipe, P. Gupta, C. Wang, C. Guo, Z. Wang, H. Tan, S. Mukerjee, C. Yan, High performance and cost-effective supported IrOx catalyst for proton exchange membrane water electrolysis, Electrochim Acta 385 (2021) 138391, https://doi.org/10.1016/j.electacta.2021.138391.

[13] S. Anantharaj, M. Venkatesh, A.S. Salunke, T.V.S. V. Simha, V. Prabu, S. Kundu, High-Performance Oxygen Evolution Anode from Stainless Steel via Controlled Surface Oxidation and Cr Removal, ACS Sustain Chem. Eng. 5 (2017) 10072–10083, https://doi.org/10.1021/acssuschemeng.7b02090.

[14] F. Moureaux, P. Stevens, G. Toussaint, M. Chatenet, Timely-activated 316L stainless steel: A low cost, durable and active electrode for oxygen evolution reaction in concentrated alkaline environments, Appl. Catal. B 258 (2019) 117963, https://doi.org/10.1016/j.apcatb.2019.117963.

[15] B. Chen, A.L.G. Biancolli, C.L. Radford, S. Holdcroft, Stainless Steel Felt as a Combined OER Electrocatalyst/Porous Transport Layer for Investigating Anion-Exchange Membranes in Water Electrolysis, ACS Energy Lett. (2023) 2661−2667, https://doi.org/10.1021/acsenergylett.3c00878.

[16] I. V. Pushkareva, A.S. Pushkarev, S.A. Grigoriev, P. Modisha, D.G. Bessarabov, Comparative study of anion exchange membranes for low-cost water electrolysis, Int. J.

Hydrogen Energy 45 (2020) 26070–26079, https://doi.org/10.1016/j.ijhydene.2019.11.011.

[17] A.Y. Faid, A.O. Barnett, F. Seland, S. Sunde, NiCu mixed metal oxide catalyst for alkaline hydrogen evolution in anion exchange membrane water electrolysis, Electrochim. Acta 371 (2021) 137837, https://doi.org/10.1016/j.electacta.2021.137837.

[18] Y.S. Park, J. Jeong, Y. Noh, M.J. Jang, J. Lee, K.H. Lee, D.C. Lim, M.H. Seo, W.B. Kim, J. Yang, S.M. Choi, Commercial anion exchange membrane water electrolyzer stack through non-precious metal electrocatalysts, Appl. Catal. B 292 (2021) 120170, https://doi.org/10.1016/j.apcatb.2021.120170.

[19] Z. Liu, S.D. Sajjad, Y. Gao, H. Yang, J.J. Kaczur, R.I. Masel, The effect of membrane on an alkaline water electrolyzer, Int. J. Hydrogen Energy 42 (2017) 29661–29665, https://doi.org/10.1016/j.ijhydene.2017.10.050.

[20] Y. Wang, C.Y. Wang, K.S. Chen, Elucidating differences between carbon paper and carbon cloth in polymer electrolyte fuel cells, Electrochim. Acta 52 (2007) 3965–3975, https://doi.org/10.1016/j.electacta.2006.11.012.

[21] L. Peng, Z. Wei, Catalyst Engineering for Electrochemical Energy Conversion from Water to Water: Water Electrolysis and the Hydrogen Fuel Cell, Engineering 6 (2020) 653–679, https://doi.org/10.1016/j.eng.2019.07.028.

[22] P. Yi, L. Peng, T. Zhou, H. Wu, X. Lai, Development and characterization of multilayered Cr-C/a-C:Cr film on 316L stainless steel as bipolar plates for proton exchange membrane fuel cells, J. Power Sources 230 (2013) 25–31, https://doi.org/10.1016/j.jpowsour.2012.11.063.

[23] S.D. Sajjad, Y. Gao, Z. Liu, H. Yang, R. Masel, Tunable-High Performance Sustainion^{TM} Anion Exchange Membranes for Electrochemical Applications, ECS Meeting Abstracts MA2017-01 (2017) 1833–1833, https://doi.org/10.1149/ma2017-01/39/1833.

[24] A. Carbone, S.C. Zignani, I. Gatto, S. Trocino, A.S. Aricò, Assessment of the FAA3-50 polymer electrolyte in combination with a $NiMn_2O_4$ anode catalyst for anion exchange membrane water electrolysis, Int. J. Hydrogen Energy 45 (2020) 9285–9292, https://doi.org/10.1016/j.ijhydene.2020.01.150.

[25] D. Henkensmeier, M. Najibah, C. Harms, J. Žitka, J. Žitka, K. Bouzek, Overview : State-of-the Art Commercial Membranes for Anion Exchange Membrane Water Electrolysis, J. Electrochem. Energy Convers. Storage 18 (2021) 024001, https://doi.org/10.1115/1.4047963.

[26] I. Vincent, E.C. Lee, H.M. Kim, Comprehensive impedance investigation of low-cost anion exchange membrane electrolysis for large-scale hydrogen production, Sci. Rep. 11 (2021) 293, https://doi.org/10.1038/s41598-020-80683-6.

[27] J. Eun, S. Young, S. Oh, J. Kwan, M. Su, C. Ahn, Y. Cho, Y. Sung, High-performance anion-exchange membrane water electrolysis, Electrochim. Acta 295 (2019) 99–106, https://doi.org/10.1016/j.electacta.2018.10.143.

[28] L. Wan, Z. Xu, B. Wang, Green preparation of highly alkali-resistant PTFE composite membranes for advanced alkaline water electrolysis, J. Chem. Eng. 426 (2021) 131340, https://doi.org/10.1016/j.cej.2021.131340.

[29] N. Chen, S.Y. Paek, J.Y. Lee, J.H. Park, S.Y. Lee, Y.M. Lee, High-performance anion exchange membrane water electrolyzers with a current density of 7.68 A cm^{-2} and a durability of 1000 hours†, Energy Environ. Sci. 14 (2021) 6338–6348, https://doi.org/10.1039/d1ee02642a.

[30] B. Motealleh, Z. Liu, R.I. Masel, J.P. Sculley, Z. Richard Ni, L. Meroueh, Next-generation anion exchange membrane water electrolyzers operating for commercially relevant lifetimes, Int. J. Hydrogen Energy 46 (2021) 3379–3386, https://doi.org/10.1016/j.ijhydene.2020.10.244.

[31] Z. Liu, S.D. Sajjad, Y. Gao, J. Kaczur, R. Masel, An Alkaline Water Electrolyzer with Sustainion^{TM} Membranes: 1 A/cm^2 at 1.9V with Base Metal Catalysts, ECS Meeting Abstracts MA2017-01 (2017) 1413–1413, https://doi.org/10.1149/ma2017-01/30/1413.

Chapter 4: Comparing Membranes for Proton Exchange Membrane Water Electrolysis: Performance, Stability and Hydrogen Crossover

Acknowledgements and declarations

I would like to acknowledge Alex Pitman (a MSc. in chemistry alumnus, University of Glasgow) for his significant contributions to this project. I trained Alex to undertake most of the experimental work in this Chapter, which he performed under my close and constant supervision, including the preparation and spraying of the catalyst ink, as well as the electrochemical experiments. I performed the physicochemical analyses. The analysis of the data and the interpretation of the data in this Chapter are entirely my own work.

Additionally, I acknowledge the Geoanalytical Electron Microscopy and Spectroscopy (GEMS) facility at the University of Glasgow for the support and assistance with performing the scanning electron microscope imaging.

Abstract

The supply of Nafion and Aquivion proton exchange membranes is currently severely constrained, prompting a search for alternatives. In this work, a new commercial proton exchange membrane (PFSA D170-U) was evaluated and compared with two other membranes: Nafion™ N117 and Aquivion® E98-15S. The performance, stability over 100 h, and H_2 crossover characteristic of these three membranes were investigated in a flow cell electrolyser , testing each membrane type in triplicate using a fresh sample of membrane for each experimental run. At 60 °C, the three membranes showed an average performance of 1 A cm^{-2} at 2.0 V and an average degradation rate of 1.2 mV h^{-1} after stability tests for 100 h at a fixed current density of 1.0 A cm^{-2}. The three membranes showed similar metrics, suggesting that PFSA D170-U is a promising proton exchange membrane alternative to Nafion and Aquivion membranes for research purposes.

4.1. Introduction

The production of green hydrogen by electrolysis would be a pivotal process in the energy transition and the drive to reach net zero, as it provides a route by which to store renewably-generated electricity as a clean-burning fuel [1]. Proton exchange membrane (PEM) electrolysers are seen as especially promising for green hydrogen production, due to their rapid response times and high efficiency [2].

Proton exchange membrane electrolysers are “zero-gap” systems, featuring a compact design, whereby a solid membrane functions as both the electrolyte in the cell and as a separator to prevent the hydrogen and oxygen products of water electrolysis from mixing [3,4]. As shown in Figure 1, the membrane is sandwiched between two porous gas diffusion layers allowing ingress of water, egress of product gases, and providing an electrical connection for the electrochemical reactions that are occurring. Catalysts for the water splitting reactions (typically IrO_2 for the oxygen evolution reaction and Pt/C for the hydrogen evolution reaction) can be applied directly to the membrane, or sometimes they are applied to the gas diffusion layers that are in contact with the membrane [4,5]. All these components are compressed tightly together between conductive plates, ensuring an inherently low internal resistance [6–8].

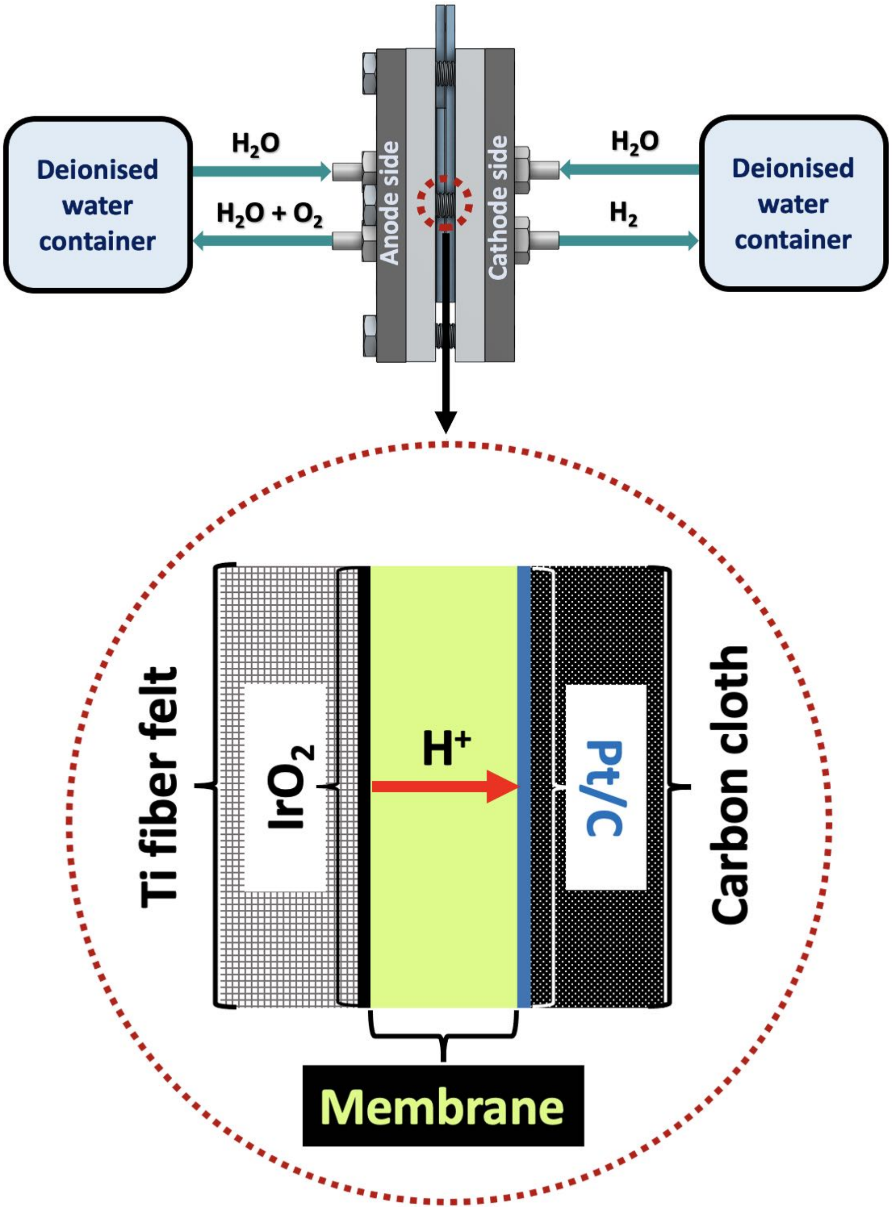

Figure 1: Schematic illustration of the inside of a single cell in a zero-gap proton exchange membrane water electrolyser.

Perfluorosulfonic acid membranes are the standard and most widely used polymer membranes in proton exchange membrane water electrolysers due to their high mechanical and chemical durability and high proton conductivity and selectivity [9]. The structure of these membranes consists of a hydrophobic Teflon backbone (providing the membranes with high thermal, mechanical, and chemical robustness due to the strong C–F bonds [10]), and hydrophilic sulfonic acid headgroups [11]. These sulfonate headgroups line hydrophilic channels through the otherwise hydrophobic membrane, allowing protons (and other small cations) and water molecules to permeate through the membrane. Proton permeation through the membrane during water electrolysis completes the electrochemical circuit.

Currently, the Nafion-based long side-chain perfluorinated membranes, first supplied by DuPont more than 60 years ago [12,13], dominate the market for most electrochemical proton exchange membrane applications [14]. A widely-available alternative perfluorinated membrane, Aquivion (developed by Solvay Specialty Polymers company), has a shorter side-chain than Nafion, as shown in Scheme 1.

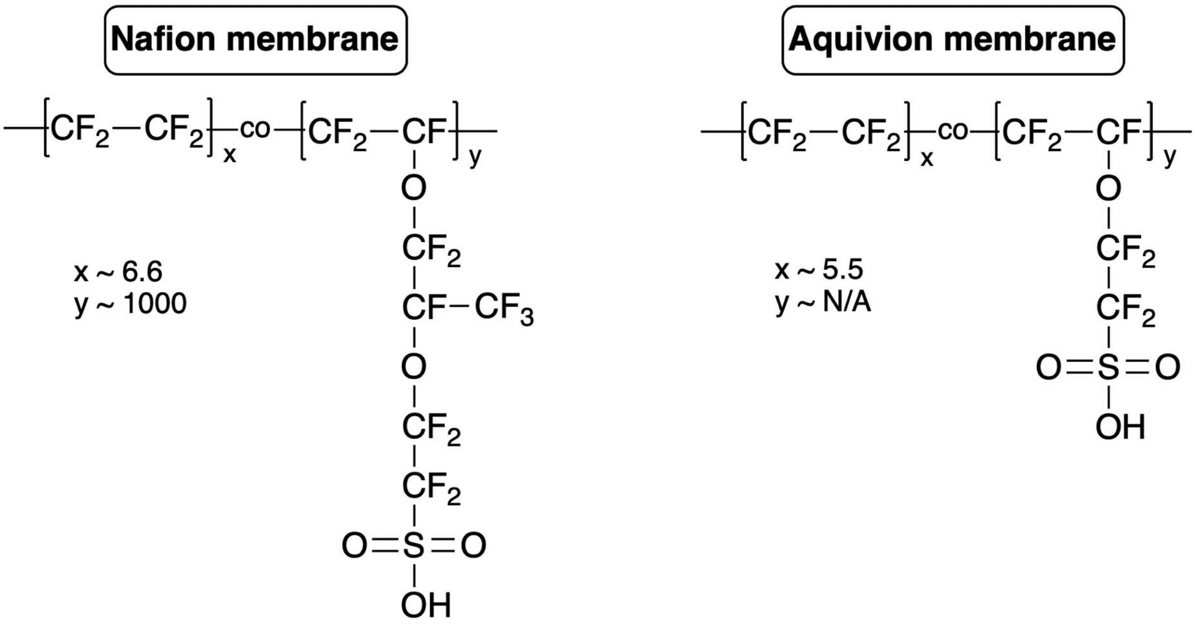

Scheme 1: *Simplified chemical structures of the protonated forms of the polymeric Nafion and Aquivion membranes.*

As many electrochemists will be aware, over the last twenty months or so, Nafion and Aquivion have been increasingly difficult to obtain, with several well-known distributors of these membranes (e.g. Merck and FuelCellStore), have discontinued supply at time of writing. Growing demand in many electrochemical applications [9,15], coupled to a limited number of manufacturers of Nafion (i.e. Chemours) and Aquivion (i.e. Solvay) could be contributing factors in this scarcity. Regardless of the precise reasons, other manufacturers are now seeking to address the unmet demand for proton exchange membranes for electrochemical devices by developing alternatives. However, as these alternative membranes are all relatively new and untested, it is not obvious as to the extent to which these are suitable for incorporation into electrochemical devices. Independent studies comparing their performance to Nafion and Aquivion are also lacking. Such investigations are crucial if the general electrochemical community is to have confidence in these membranes, and in the data collected from cells and devices constructed using these membranes.

On several occasions over the last eighteen months (at time of writing), the authors found themselves in the following quandary: "I need to assess the efficacy of catalyst X or component Y in an electrochemical cell, but I cannot obtain Nafion or Aquivion. Can I use membrane Z instead, and if so, is membrane Z sufficiently durable and robust to allow me to assess the efficacy of catalyst X or component Y with confidence?". Motivated by a desire to provide some clarity (both for ourselves and others facing the same challenge) as to what might be a suitable readily-available alternative to Nafion and Aquivion, we herein evaluated PFSA D170-U (a new perfluorinated sulfonic acid membrane supplied by FuelCellStore) as a proton exchange membrane for green hydrogen production by electrolysis. By comparing the performance of PFSA D170-U to Nafion™ N117 and Aquivion® E98-15S (in terms of current-voltage profiles, bulk electrolysis, and H_2 crossover), we show that PFSA D170-U is a competent replacement for Nafion™ N117 and Aquivion® E98-15S for electrolytic water splitting, at least over a timeframe of 100 h (suitable for initial assessment of many potential catalysts and new cell components). We hope these findings will allow research and development in proton exchange membrane electrolysis to continue despite the current scarcity of established proton exchange membranes.

4.2. Experimental

4.2.1. Flow cell components, setup, and assembly

The flow cell used in this work (active area = 13 cm^2) has previously been reported and characterised, and open access designs for this cell are available [7]. In brief, the flow cell comprised of a pair of 3 mm-thick Ti current collector/flow-field plates with six serpentine channels per plate. The cathode consisted of 0.5 mg cm^{-2} Pt/C (supported on Vulcan carbon and mixed with Nafion ionomer) deposited on a carbon cloth (W1S1011, FuelCellStore). At the anode side, a Ti fibre felt (FuelCellStore) coated with Ti microparticles (5 μm, US Nanomaterials Research, Inc.) and IrO_2 (99.9%, Sigma Aldrich) were used. These anodes were prepared in-house as follows (see also Figure 2). Firstly, in a glove box under N_2, 2.5 g of 5 μm Ti microparticles were added into a vial. Subsequently, 10 g of isopropanol and 2.5 mg of 5% alcohol-based Nafion solution (Nafion™ D520CS, Ion Power, Inc.) were added into the vial and mixed with the Ti microparticles with the aid of ultrasonication of the vial in an ice bath for 15 min. After this initial mixing, 10 g of ethylene glycol was added to this mixture, which was ultrasonicated for an additional 1 h to give a suspension. The Ti fibre felts were sprayed with this suspension and then placed in a preheated oven at 200 °C for 7 min to ensure the evaporation of the ethylene glycol before weighing. Immediately before spraying, the bottle containing the suspension was shaken vigorously, ensuring the homogenous dispersion of Ti microparticles in the suspension. When spraying, the airbrush was positioned around 15 cm away from the centre of the Ti fibre felt and the air compressor pressure was set at 2 bar. The spray process started from the centre, and was then directed towards the top edge of the felt and continued in a clockwise direction until the entire Ti fibre felt was coated; multiple spray circles were required for obtaining the desired mass loading (approximately 1 mg cm^{-2} of Ti microparticles on the surface of the fibre in this case). Subsequently, this Ti microparticle-coated Ti fibre felt was sprayed with IrO_2 ink. This ink was prepared by mixing Nafion solution, carbon black (carbon black, acetylene, 50% compressed, 99.9+%, Thermo Fisher Scientific), and IrO_2 powder in a 15:20:65 mass ratio, in addition to ~ 5 mL of isopropanol, followed by ultrasonication of this mixture in an ice bath for 2 h. After ultrasonication, this ink mixture was placed in the freezer at −20 °C for 15 min before spraying to increase its wettability. The same spraying method used for spraying the microporous layer was followed for spraying the IrO_2 catalyst, except that the air compressor pressure was set at 1.5 bar. After spraying, the Ti fibre felt (with a mass loading of 1.5 mg cm^{-2} IrO_2,) was placed in a preheated oven at 100 °C for 1 h before use. Two different AB-182 double-action suction-feed airbrushes (0.5 mm nozzle, Everything Airbrush, UK) were used for spraying the microporous Ti suspension and IrO_2 ink. The coated GDLs were tested immediately after spraying.

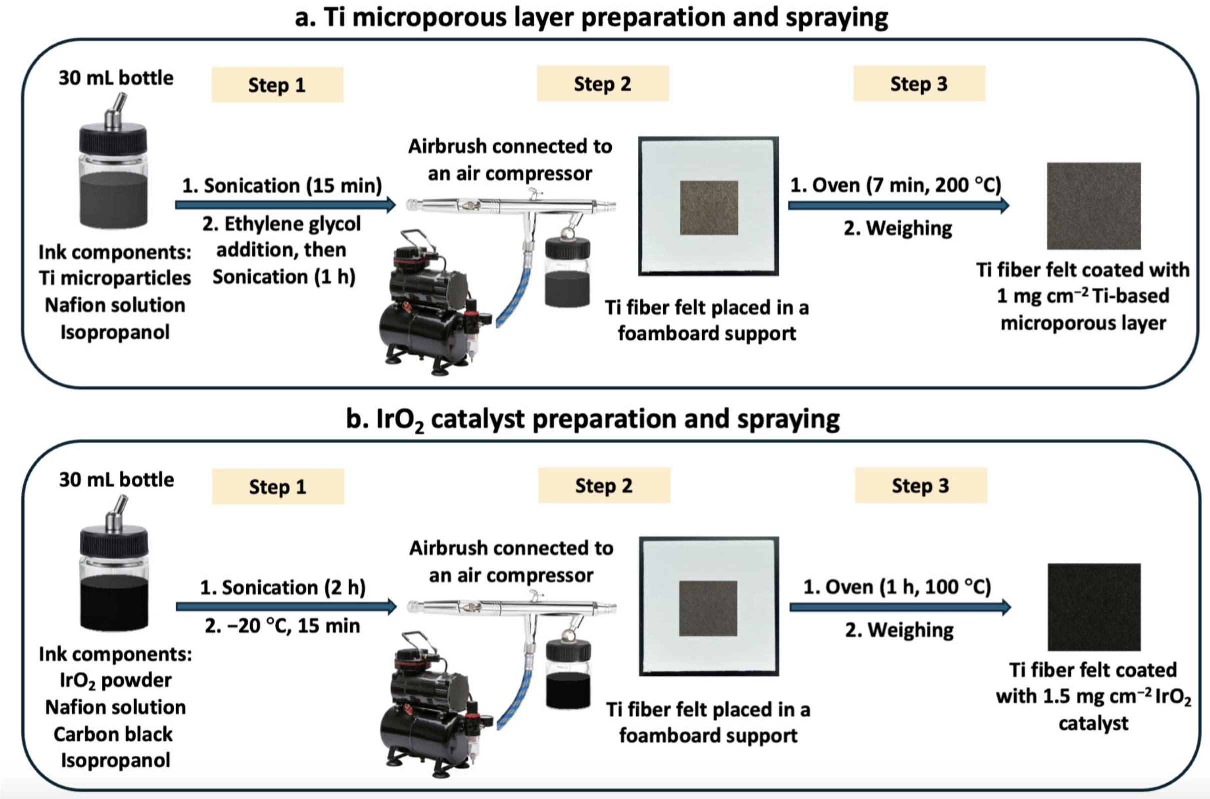

***Figure 2:** A schematic illustration of the protocols for (a) Ti microporous layer and (b) IrO_2 catalyst preparation and spraying on a Ti fibre felt.*

Three different proton exchange membranes were evaluated in flow cell set-up: Nafion™ N117 (177.8 µm, Ion Power, Inc), Aquivion® E98-15S (150 µm, FuelCellStore), and PFSA D170-U (170 µm, FuelCellStore). Polytetrafluoroethylene gaskets (FuelCellStore) with various thicknesses (0.127 mm, 0.254 mm, and 0.508 mm) were employed, preventing both leakages and direct contact of the current collector/flow-field plates. All the flow components were assembled and compressed together with a 5.65 Nm clamping force on each bolt [7]. In all experiments, deionised water (15 MΩ-cm resistivity) was fed to both the anode and cathode through Norprene tubing (Merck Life Science UK Limited) at flow rate of 40 mL min^{-1} using two Masterflex™ L/S peristaltic pumps (model 77201-60). The circulating liquid electrolyte was kept in 1 L media bottles as the electrolyte reservoirs. The temperature of both the anodic and cathodic water reservoirs was measured using K-type thermocouples placed on the outlets and inlets of the cathode and anode sides. The temperature data were monitored by a Pico TC-08 data logger (Pico Technology). A BioLogic SP-150 potentiostat equipped with an 80 A booster was used to conduct the electrochemical tests.

4.2.2. Electrolyte characterisation

Inductively coupled plasma optical emission spectroscopy (ICP-OES) analysis was conducted for detecting any leached metal residuals in the electrolyte reservoirs using an Agilent 5900 ICP-OES equipped with an Agilent SPS4 autosampler. The apparatus was calibrated with Ir and Pt reference standards. The ICP-OES samples were collected from the catholyte and anolyte circulating in the cell with volumes of 1.9 L and 0.7 L, respectively.

4.2.3. Electrochemical characterisation

Each type of membrane was assessed three times, using a fresh piece of membrane in each experimental run, and the results presented for each material are averages of these three repeats. Linear sweep voltammetry measurements were performed between 0 and 2.0 V at a scan rate of 10 mV s^{-1}. Chronopotentiometry measurements were performed at a fixed current density of 1.0 A cm^{-2} for 100 h, as stability tests. Due to the observed electro-osmotic drag [16], water was pumped back from the cathode reservoir to the anode reservoir after approximately 48 h of electrolysis.

4.2.4. Proton exchange membrane pretreatment

The proton exchange membranes were delivered in a dry form, and then were submerged in deionised water at room temperature (around 20 °C) for at least 24 h before use.

4.2.5. Gas chromatography analysis

To measure the extent of crossover of H_2 through the membrane from the cathode, an Agilent 8860 gas chromatograph system was used. All gas samples were taken from the anolyte reservoir's headspace. A flowchart mapping out all the gas samples taken (in order) for gas chromatography analysis is shown in Figure 3. Pre-electrolysis baseline gas samples were taken after purging the anolyte with Ar at 1 bar for 30 min. Additional samples were taken after applying a fixed current density of 1.0 A cm^{-2} for 1 h. Stability tests (wherein a constant current density of 1.0 A cm^{-2} was applied for 100 h) were then performed, after which further gas samples were taken subsequent to purging the anolyte again with Ar for 30 min. Subsequently, additional samples were taken after applying a fixed current density of 1.0 A cm^{-2} for another 1 h. By this method, the amount of H_2 crossover observed in the first hour of electrolysis (with a pristine membrane) could be compared to the crossover observed over a duration of 1 h with the same membrane but after 100 h of galvanostatic electrolysis, to see if the amount of crossover had increased (which would suggest some degradation of the membrane).

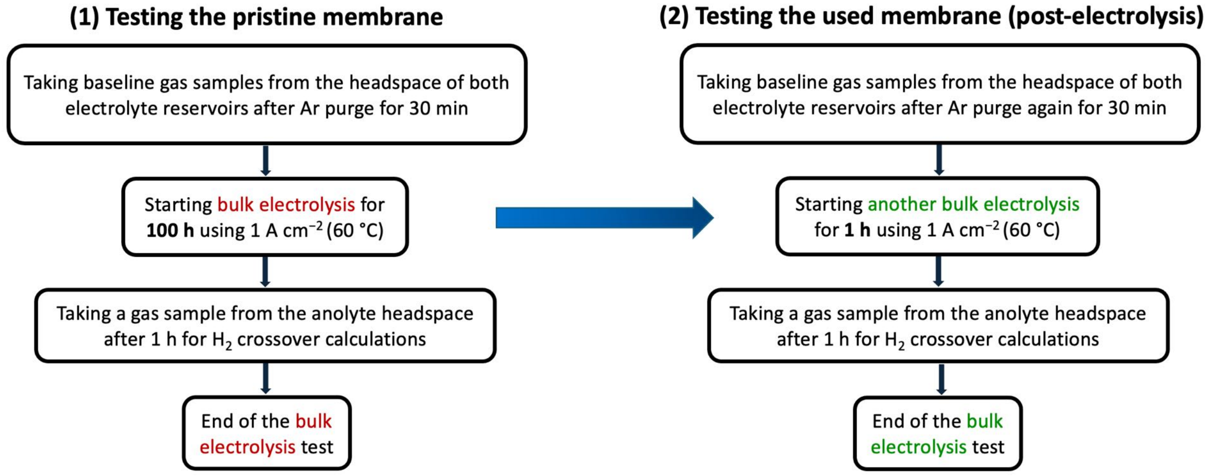

Figure 3: *A flowchart illustrating the sequential collection of gas samples from the headspace of the electrolyte reservoirs for gas chromatography analysis: (1) prior to and (2) following each stability test (bulk electrolysis at 1.0 A* cm^{-2} *for 100 h).*

A calibration curve for H_2 quantitative analysis was generated to correlate the peak areas (generated by the gas chromatography instrument) with the amount of H_2 expressed in moles. The calibration curve (Figure 4) was prepared to quantify the H_2 crossed over to the anode side by injecting four different standards of H_2 gas (1%, 2%, 3%, 5% H_2/argon standards).

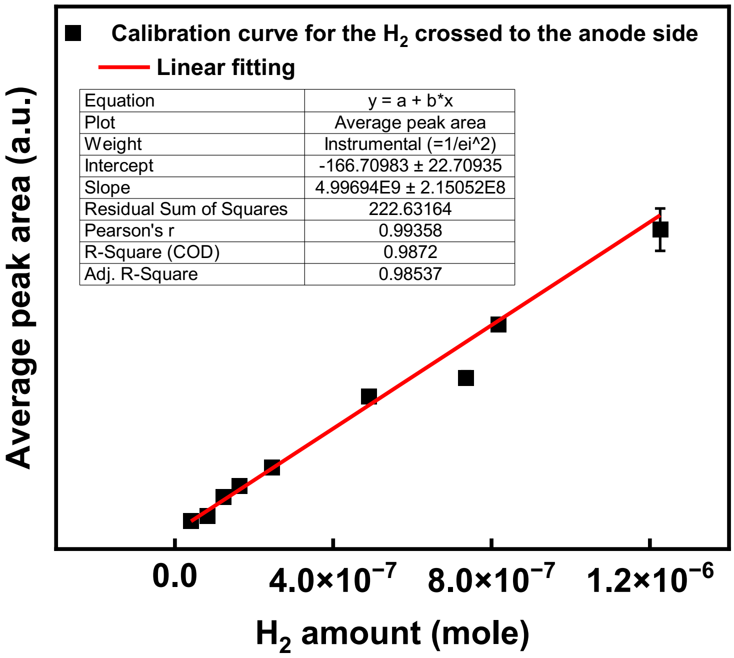

Figure 4: *A calibration curve plot generated by injecting four different standards of H_2 gas (1%, 2%, 3%, 5% H_2/argon standards) using various volumes, to quantify the H_2 crossed over to the anode side.*

All the H_2 quantity values were calculated by considering the headspace of the anolyte reservoir and the gas microsyringe volume (600 µL) used to collect the H_2 gas samples from the anolyte headspace, as shown in the following equation (equation 1).

$$The\ H_2\ quantity\ (in\ moles) = \frac{Hydrogen\ peak\ area \times headspace\ volume\ (L)}{\text{Calibration curve slope } \times 0.0006\text{ L (gas microsyringe volume)}} \qquad (1)$$

4.2.6. Scanning electron microscope imaging of the membranes

To investigate the PFSA D170-U membrane’s morphology in its pristine form and after a stability test, scanning electron microscope analysis was conducted. It was performed in the Geoanalytical Electron Microscopy and Spectroscopy (GEMS) facility at the School of Geographical and Earth Sciences, University of Glasgow, using a Zeiss Sigma variable-pressure field-emission scanning electron microscope under high vacuum conditions.

4.2.7. Fourier transform infrared (FT-IR) characterisation of the membranes

Fourier transform infrared measurements were conducted using a Jasco FT/IR-4100 infrared spectroscopy instrument. The measurements were taken before and after each stability test, using these parameters: a scan number of 128, a resolution of 4.0 cm^{-1}, and a wavenumber range of 4000 to 600 cm^{-1}.

4.3. Results and discussion

4.3.1. Performance and stability of the proton exchange membranes

The performance of the Nafion™ N117, Aquivion® E98-15S, and PFSA D170-U membranes was investigated by linear sweep voltammetry at 60 °C, as illustrated in Figure 5 and Table 1. Each membrane material was tested three times, using a fresh sample of membrane for each experimental run; the results shown for each membrane are averages of three polarisation curves runs. Within the margin of error, all three membranes exhibited essentially identical performance. Although the collective level of performance of the cells constructed using these membranes was somewhat lower than that reported for optimised commercial electrolysers (~ 2 A cm^{-2} at 2 V) [17], their performance is comparable to other laboratory systems reported recently (see Table 2). Their modest performance, compared to commercial systems, may be attributed to the catalyst-coated substrate approach used in this work (whereby IrO_2 was sprayed onto the anode, and this electrode then compressed mechanically against the membrane), which dispensed with any hot pressing as employed usually in commercial cells. Hot pressing tends to produce stronger interfacial contact between the membranes and catalyst layers and lower ohmic resistance, albeit at the expense of increased cost of the membrane electrode assembly [18,19].

The stability of the three membranes was then examined by galvanostatic electrolysis at 1.0 A cm^{-2} for 100 h at 60 °C (Figure 6). Again, within the margin of error (determined from three separate tests per membrane type), all three membranes showed similar performance (Table 1).

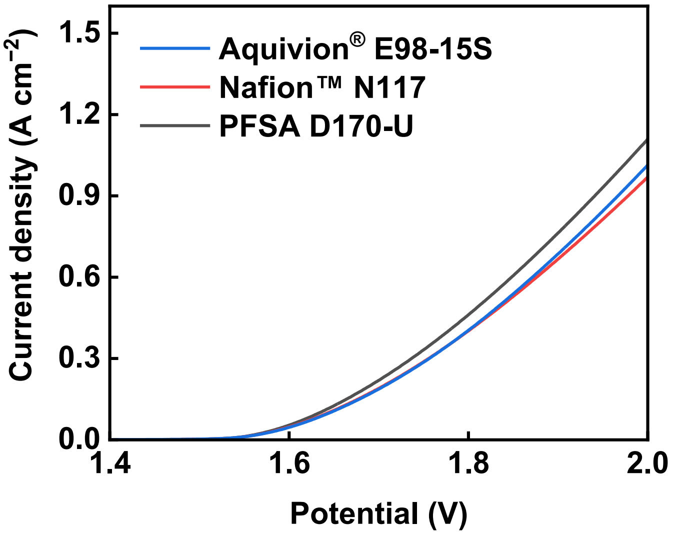

Figure 5: *Polarisation curves of the water electrolyser, derived at a scan rate of 10 mV s*$^{-1}$*, using three different proton exchange membranes, Ti fibre felts sprayed with 1.5 mg cm*$^{-2}$ IrO_2 *as the anode and 0.5 mg cm*$^{-2}$ *Pt/C deposited on carbon cloth as the cathode. The results shown here for each membrane are averages of three polarisation curves.*

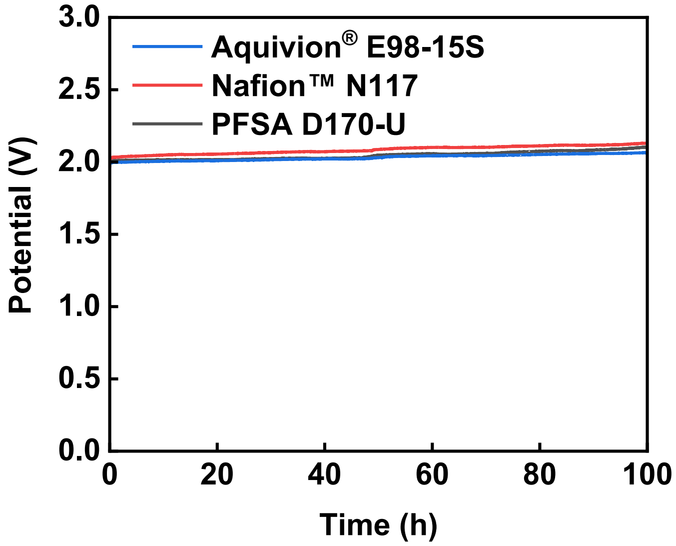

Figure 6: *The chronopotentiometric evaluation of the water electrolyser at 1.0 A cm*$^{-2}$ *using three different proton exchange membranes, Ti fibre felts sprayed with 1.5 mg cm*$^{-2}$ IrO_2 *as the anode and 0.5 mg cm*$^{-2}$ *Pt/C deposited on carbon cloth as the cathode. The results for each membrane are the average of three separate stability tests.*

Table 1: *The average current densities derived from linear sweep voltammetry and the average membrane degradation rates obtained from stability tests for 100 h at a fixed current density of 1.0 A cm*$^{-2}$ *(all tests were performed at 60 °C). The average current densities and membrane degradation rates were obtained by testing three fresh samples of each membrane, with one test per fresh sample.*

Membrane	**Current density (A cm^{-2}) at 2.0 V**	**Degradation rate (mV h^{-1})**
Aquivion® E98-15S	1.02 ± 0.05	0.84 ± 0.13
PFSA D170-U	1.11 ± 0.08	1.42 ± 0.15
Nafion™ N117	0.97 ± 0.03	1.33 ± 0.4

Table 2: *The performance of proton exchange membrane water electrolysers using different components and conditions. Pt/C and IrO_2 were employed as cathode and anode catalysts, respectively.*

Membrane	**Current density ($A\ cm^{-2}$) at 2.0 V**	**Mass loading ($mg\ cm^{-2}$)**	**Temperature**	**Ref**
Nafion™ N117	0.97	0.5 (cathode) 1.5 (Anode)	60 °C	**This work**
Aquivion® E98-15S	1.02	0.5 (cathode) 1.5 (Anode)	60 °C	**This work**
PFSA D170-U	1.11	0.5 (cathode) 1.5 (Anode)	60 °C	**This work**
Aquivion® E87-12S	1	2 (cathode) 2 (Anode)	80 °C	[20]
Nafion® 117	~ 0.11	1 (cathode) 2 (Anode)	25 °C	[21]
Nafion® 117	~ 0.35	NA	70 °C	[22]
Nafion® 117	~ 0.4	0.138 (Cathode) 1.305 (Anode)	80 °C	[23]

To confirm that these stability test results were not influenced by any potential leaching of the catalysts, elemental analysis of the anolyte and catholyte after each stability test was conducted using inductively coupled plasma-optical emission spectroscopy (Table 3). The IrO_2 catalyst leaching was negligible, with content in solution being below 0.005 mg cm^{-2} after all tests, whilst the concentrations of Pt were below the limit of detection (0.02 mg L^{-1}) of the ICP-OES instrument, confirming the robustness of the catalysts in all cases.

Table 3: *The average IrO_2 and Pt content in the anolyte and catholyte, respectively, after stability tests for 100 h at a fixed current density of 1.0 A cm^{-2} at 60 °C. The values were calculated by accounting for the volume of electrolytes circulating in the cell at the time of sample collection (catholyte = 1.9 L and anolyte = 0.7 L) , then normalised to the geometric area of the GDLs (13.7 cm^2).*

Membrane	**IrO_2 content in anolyte (mg cm^{-2})**	**Pt content in catholyte (mg L^{-1})**
Aquivion® E98-15S	0.003 ± 0.001	< 0.02
PFSA D170-U	0.004 ± 0.003	< 0.02
Nafion™ N117	0.002 ± 0.001	< 0.02

4.3.2. Hydrogen crossover measurements

Measurements of H_2 crossover from the cathode side to the anode side for each membrane in its pristine form were taken after applying a fixed current density of 1.0 A cm^{-2} for 1 h. Subsequently, electrolysis was resumed at 1.0 A cm^{-2} and continued for 100 h, after which electrolysis was paused and the anolyte thoroughly purged with Ar to remove all the H_2 generated during the 100-h electrolysis (which was confirmed by gas chromatography). After this, electrolysis was resumed again for 1 h at 1.0 A cm^{-2}, after which time the amount of hydrogen gas in the anolyte reservoir headspace was measured and compared to the amount that had crossed over during the 1 h electrolysis with the pristine membrane (Figure 7 and Table

4). In the membranes' pristine form, the membranes showed similar H_2 crossover characteristics (within the margin of error). In contrast, in the measurements taken after stability tests and after 1 h galvanostatic electrolysis, PFSA D170-U and Nafion N117 showed similar levels of crossover (within the margin of error), as did Nafion N117 and Aquivion E98-15S. However, PFSA D170-U and Aquivion E98-15S did not exhibit similar levels of crossover, whereby slightly lower levels of crossover were observed using Aquivion E98-15S, highlighting a measurable distinction between these two membranes despite their respective similarities with Nafion N117. Relating the H_2 crossover results obtained using these membranes to the literature were not possible, as the percentage of H_2 concentration in O_2 (vol%) were not measured, due to the leakage of O_2 gas from the anolyte reservoir under pressurised conditions at elevated O_2 quantity.

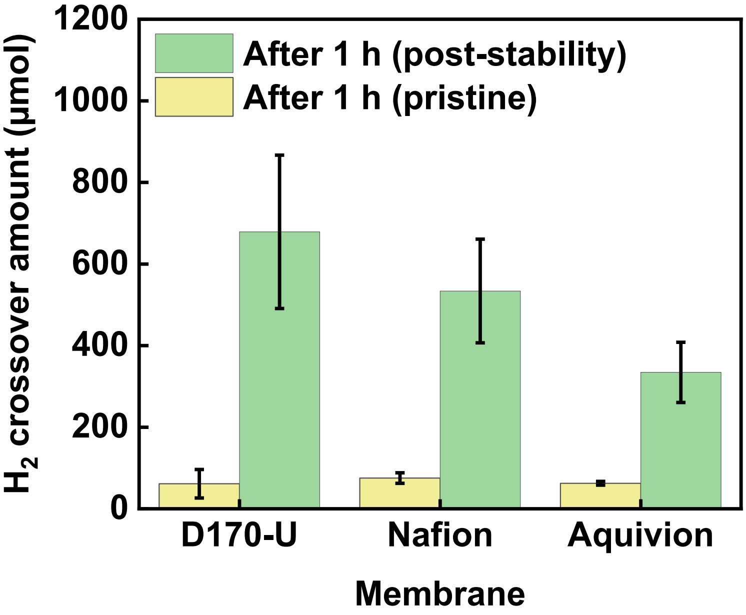

Figure 7: *The average extent of H_2 crossover into the anolyte headspace observed after 1 h of electrolysis, performed before (yellow) and after (green) a 100 h galvanostatic stability test. In all cases, a current density of 1.0 A cm^{-2} was applied at 60 °C.*

Table 4: *The average extent of* H_2 *crossover into the anolyte headspace observed after 1 h of electrolysis, performed before (yellow) and after (green) a 100 h galvanostatic stability test. In all cases, a current density of 1.0 A* cm^{-2} *was applied at 60 °C.*

Membrane	**H_2 in anolyte headspace (µmol) after 1 h**	**H_2 in anolyte headspace (µmol) after 100 h**	**Difference in amount of H_2 in anolyte headspace (µmol) after 1 h and 100 h**
Aquivion® E98-15S	62.6 ± 4.7	334.5 ± 74.8	271.9
PFSA D170-U	61.4 ± 34.8	678.8 ± 188.0	617.4
Nafion™ N117	75.3 ± 12.8	533.8 ± 128.1	458.5

4.3.3. Fourier transform infrared (FT-IR) measurements

To investigate any change in the polymer matrix of the D170-U membrane after the stability test for 100 h at 1.0 A cm^{-2} (at 60 °C), FT-IR measurements were taken on the membrane in its pristine form and after the stability test (Figure 8). The chemical structure of the D170-U membrane was retained, whereby the following characteristic peaks did not disappear after the stability test (Figure 8): the symmetric S–O stretching (~ 1060 cm^{-1}), the C–S stretching vibration (~ 630 cm^{-1}), the C–O–C stretches (~ 970 cm^{-1}), and the strong symmetric C–F stretching (~ 1145 cm^{-1}) and asymmetric C–F stretching (~ 1201 cm^{-1}) [24–27]. Additionally, a broad peak appears at ~ 3400 cm^{-1} corresponds to the water molecule O–H stretching vibration, and the water molecule O–H bending vibration appears at ~ 1640 cm^{-1} [28–30].

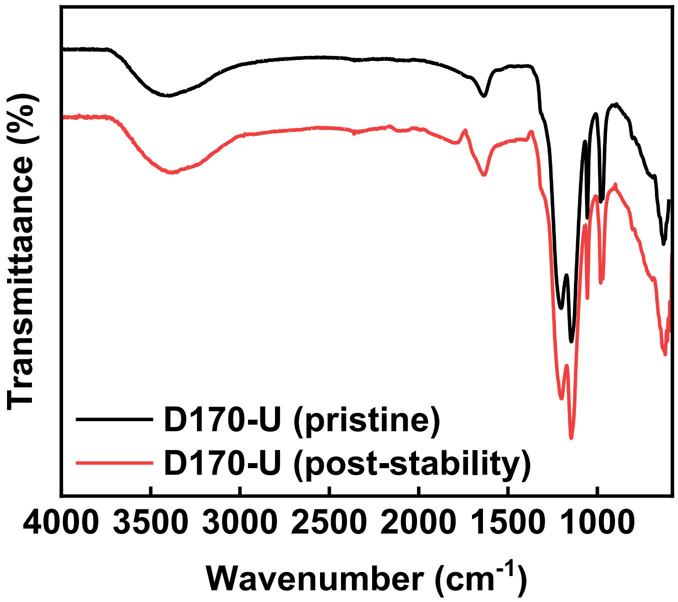

Figure 8: *The Fourier transform infrared spectroscopy (FT-IR) spectra of the D170-U membrane before (i.e. in its pristine form) and after 100 h operational electrolysis at 1.0 A* cm^{-2} *(at 60 °C).*

4.3.4. Scanning electron microscopy imaging

Scanning electron microscope images of the top surface of the PFSA D170-U membrane were taken in its pristine form and after the stability test for 100 h. Although some debris from the carbon cloth and Pt/C covered some of the pores on the membrane structure after the stability test, the membrane structure did not change, indicating the mechanical robustness of the membrane during the stability test (Figure 9).

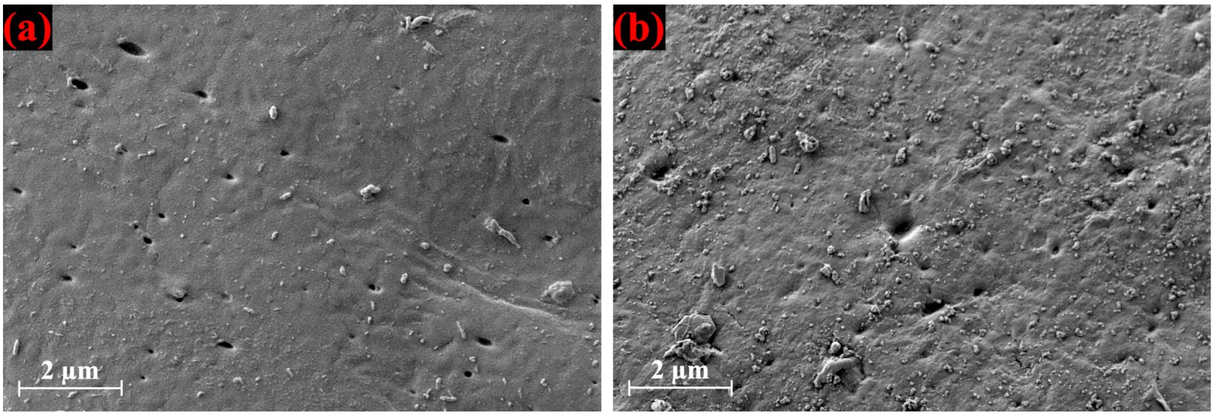

Figure 9: *Scanning electron microscope images of the PFSA D170-U membrane in its pristine form (image a) and after the galvanostatic electrolysis for 100 h at 60 °C (image b).*

4.4. Conclusions

Herein, a new commercially available perfluorinated sulfonic acid membrane (PFSA D170-U) was evaluated in a water electrolyser as an alternative proton exchange membrane to Nafion and Aquivion, which have been in short supply recently. The performance, stability, and H_2 crossover characteristic of PFSA D170-U were investigated and compared to those of Nafion™ N117 and Aquivion® E98-15S. On timescales of up to 100 h (suitable in many research and development contexts), PFSA D170-U showed broadly similar performance to that of the two other membranes, positioning it as a promising alternative proton exchange membrane for water electrolysis applications.

References

[1] P.J. McHugh, A.D. Stergiou, M.D. Symes, Decoupled Electrochemical Water Splitting: From Fundamentals to Applications, Adv. Energy Mater. 10 (2020) 2002453, https://doi.org/10.1002/aenm.202002453.

[2] S. Shiva Kumar, H. Lim, An overview of water electrolysis technologies for green hydrogen production, Energy Rep. 8 (2022) 13793–13813, https://doi.org/10.1016/j.egyr.2022.10.127.

[3] S. Shiva Kumar, V. Himabindu, Hydrogen production by PEM water electrolysis – A review, Mater. Sci. Energy Technol. 2 (2019) 442–454, https://doi.org/10.1016/j.mset.2019.03.002.

[4] M. Carmo, D.L. Fritz, J. Mergel, D. Stolten, Comprehensive review on PEM water electrolysis, Int. J. Hydrogen Energy 38 (2013) 4901–4934, https://doi.org/10.1016/j.ijhydene.2013.01.151.

[5] A.K. Samuel, A.H. Faqeeh, W. Li, Z. Ertekin, Y. Wang, J. Zhang, N. Gadegaard, D.A.J. Moran, M.D. Symes, A.Y. Ganin, Assessing Challenges of 2D-Molybdenum Ditelluride for Efficient Hydrogen Generation in a Full-Scale Proton Exchange Membrane (PEM) Water Electrolyzer, ACS Sustain. Chem. Eng. 12 (2023) 1276–1285, https://doi.org/10.1021/acssuschemeng.3c06616.

[6] X. Lin, J.Z.Y. Seow, Z.J. Xu, A brief introduction of electrode fabrication for proton exchange membrane water electrolyzers, JPhys Energy 5 (2023) 034003. https://doi.org/10.1088/2515-7655/acccb1.

[7] A.H. Faqeeh, M.D. Symes, A standard electrolyzer test cell design for evaluating catalysts and cell components for anion exchange membrane water electrolysis, Electrochim. Acta 444 (2023) 142030, https://doi.org/10.1016/j.electacta.2023.142030.

[8] A.H. Faqeeh, M.D. Symes, Zero-gap bipolar membrane water electrolyzers: Principles, challenges and practical insights, Electrochim. Acta 493 (2024) 144345, https://doi.org/10.1016/j.electacta.2024.144345.

[9] E.Y. Safronova, A.A. Lysova, D.Y. Voropaeva, A.B. Yaroslavtsev, Approaches to the Modification of Perfluorosulfonic Acid Membranes, Membranes 13 (2023) 721, https://doi.org/10.3390/membranes13080721.

[10] G.H. Byun, J.A. Kim, N.Y. Kim, Y.S. Cho, C.R. Park, Molecular engineering of hydrocarbon membrane to substitute perfluorinated sulfonic acid membrane for proton exchange membrane fuel cell operation, Mater. Today Energy 17 (2020) 100483, https://doi.org/10.1016/j.mtener.2020.100483.

[11] R.T. Liu, Z.L. Xu, F.M. Li, F.Y. Chen, J.Y. Yu, Y. Yan, Y. Chen, B.Y. Xia, Recent advances in proton exchange membrane water electrolysis, Chem. Soc. Rev. 52 (2023) 5652–5683, https://doi.org/10.1039/d2cs00681b.

[12] S. Banerjee, D.E. Curtin, Nafion® perfluorinated membranes in fuel cells, J. Fluor. Chem. 125 (2004) 1211–1216, https://doi.org/10.1016/j.jfluchem.2004.05.018.

[13] D.J. Connolly, W. Frank, D. Nemours, Fluorocarbon vinyl ether polymers, US 3282875, 1966.

[14] H. Nguyen, C. Klose, L. Metzler, S. Vierrath, M. Breitwieser, Fully Hydrocarbon Membrane Electrode Assemblies for Proton Exchange Membrane Fuel Cells and Electrolyzers: An Engineering Perspective, Adv. Energy. Mater. 12 (2022) 2103559, https://doi.org/10.1002/aenm.202103559.

[15] R. Baghel, Global Market Size, Forecast, and Trend Highlights Over 2024-2036 (2024), https://www.researchnester.com/reports/nafion-market/3384 (accessed Sept. 2024).

[16] Z. Luo, Z. Chang, Y. Zhang, Z. Liu, J. Li, Electro-osmotic drag coefficient and proton conductivity in Nafion® membrane for PEMFC, Int. J. Hydrogen Energy 35 (2010) 3120–3124, https://doi.org/10.1016/j.ijhydene.2009.09.013.

[17] K. Ham, S. Bae, J. Lee, Classification and technical target of water electrolysis for hydrogen production, J. Energy Chem. 95 (2024) 554–576, https://doi.org/10.1016/j.jechem.2024.04.003.

[18] B.H. Lim, E.H. Majlan, A. Tajuddin, T. Husaini, W.R. Wan Daud, N.A. Mohd Radzuan, M.A. Haque, Comparison of catalyst-coated membranes and catalyst-coated substrate for

PEMFC membrane electrode assembly: A review, Chin. J. Chem. Eng. 33 (2021) 1–16, https://doi.org/10.1016/j.cjche.2020.07.044.

[19] E.A. Ticianelli, C.R. Derouin, A. Redondo, S. Srinivasan, Methods to Advance Technology of Proton Exchange Membrane Fuel Cells, J. Electrochem Soc. 135 (1988) 2209–2214, https://doi.org/10.1149/1.2096240.

[20] A. Skulimowska, M. Dupont, M. Zaton, S. Sunde, L. Merlo, D.J. Jones, J. Rozière, Proton exchange membrane water electrolysis with short-side-chain Aquivion® membrane and IrO_2 anode catalyst, Int. J. Hydrogen Energy 39 (2014) 6307–6316, https://doi.org/10.1016/j.ijhydene.2014.02.082.

[21] L. Morales, L.G. Arriaga, U. Cano, R. Acosta, Nafion Quantity Variation on Electrodes used in SPE Electrolyzer, ECS Meeting Abstracts MA2006-02 (2006) 537–537, https://doi.org/10.1149/MA2006-02/8/537.

[22] S. Oh, J. Yang, C.H. Chu, I.C. Na, K. Park, Degradation evaluation of PEM water electrolysis by method of degradation analysis used in PEMFC, Korean Chem. Eng. Res. 59 (2021) 1–5, https://doi.org/10.9713/kcer.2021.59.1.1.

[23] J.T.H. Kwan, L. Daniel, W.J. Wang, K.L.W. Yao, D.S. Shehata, D.P. Wilkinson, New multi-functional catalyst coated membrane structure for improved water electrolysis, J. Power Sources 591 (2024) 233872, https://doi.org/10.1016/j.jpowsour.2023.233872.

[24] Y. Zhai, H. Zhang, J. Hu, B. Yi, Preparation and characterization of sulfated zirconia (SO_4^{2-}/ZrO_2)/Nafion composite membranes for PEMFC operation at high temperature/low humidity, J. Memb. Sci. 280 (2006) 148–155, https://doi.org/10.1016/j.memsci.2006.01.028.

[25] J. Ostrowska, A. Narebska, Infrared study of hydration and association of functional groups in a perfluorinated Nafion membrane, Part 1, Colloid Polym. Sci. 261 (1983) 93–98, https://doi.org/10.1007/BF01410686.

[26] V. Di Noto, R. Gliubizzi, E. Negro, G. Pace, Effect of SiO_2 on relaxation phenomena and mechanism of ion conductivity of [Nafion/(SiO_2)x] composite membranes, J. Phys. Chem. B 110 (2006) 24972–24986, https://doi.org/10.1021/jp0650331.

[27] M. Laporta, M. Pegoraro, L. Zanderighi, Perfluorosulfonated membrane (Nafion): FT-IR study of the state of water with increasing humidity, Phys. Chem. Chem. Phys. 1 (1999) 4619–4628, https://doi.org/10.1039/a904460d.

[28] R. Sigwadi, M.S. Dhlamini, T. Mokrani, F. Ṋemavhola, P.F. Nonjola, P.F. Msomi, The proton conductivity and mechanical properties of Nafion®/ ZrP nanocomposite membrane, Heliyon 5 (2019) e02240, https://doi.org/10.1016/j.heliyon.2019.e02240.

[29] H.N. Yang, D.C. Lee, S.H. Park, W.J. Kim, Preparation of Nafion/various Pt-containing SiO_2 composite membranes sulfonated via different sources of sulfonic group and their application in self-humidifying PEMFC, J. Memb. Sci. 443 (2013) 210–218.https://doi.org/10.1016/j.memsci.2013.04.060.

[30] M. Tatsumisago, T. Minami, Preparation of Proton-Conducting Amorphous Films Containing Dodecamolybdophosphoric Acid by the Sol—Gel Method, J. Am. Ceram. Soc. 72 (1989) 484–486, https://doi.org/10.1111/j.1151-2916.1989.tb06159.x.

Chapter 5: Testing a Radiation-grafted Anion Exchange Membrane in The Standard Water Electrolyser

Acknowledgements

I want to express my gratitude to Prof. John Varcoe, Sian Franklin, and their research team (University of Surrey, School of Chemistry and Chemical Engineering) for supplying the radiation-grafted anion exchange membrane evaluated in this Chapter.

Additionally, I acknowledge the Geoanalytical Electron Microscopy and Spectroscopy (GEMS) facility at the University of Glasgow for the support and assistance with performing the scanning electron microscope imaging.

Abstract

Radiation-grafted anion exchange membranes are a promising category of anion exchange membranes due to their simple and versatile fabrication method, allowing the synthesis of various membranes with similar backbones but different functional headgroups. Herein, a radiation-grafted anion exchange membrane based on a backbone of poly(ethylene-co-tetrafluoroethylene) and a trimethylamine functional headgroup, supplied by a research group in the University of Surrey, was evaluated in the standard anion exchange membrane water electrolyser presented in Chapter 3. The electrochemical performance, ohmic resistance, stability, and H_2 crossover characteristic were investigated and compared to those of a commercially available anion exchange membrane (Fumasep FAA-3-50). The membrane (as a two-sheet configuration) showed similar characteristics to those of the FAA-3-50 membrane. Both membranes could not withstand the harsh conditions of the stability test for long-term operation, showing a linear drop in the cell potential. The drop in potential during the stability test was a sign of short-circuiting pathway forming between the cathode and anode sides, leading to a loss in the water electrolyser's efficiency. The presence of short-circuiting pathways was confirmed by observing aligned hotspots on the stainless steel fibre and membrane surfaces after disassembling the flow cell, as shown in Figure 9.

5.1. Introduction

Ion exchange polymer membranes are the heart of any anion exchange membrane water electrolyser. Such polymers function as a barrier preventing the mixing of the oxygen and hydrogen gases evolved during the water electrolysis process. In addition, they work as solid polymer electrolytes providing hydroxide-conductive pathways from the cathode side to the anode side, wherein the hydroxide ions are oxidised to oxygen gas [1].

The structure of anion exchange membranes comprises polymer backbones and anion exchange functional headgroups working as hydroxide-conductive channels allowing the permeation of hydroxide ions. The structure of these membranes can consist of a single class of numerous different backbones, such as polysulfone (e.g. Fumasep FAA-3-50 [2]), polystyrene (e.g. Sustainion X37-50 Scheme 1a [3]), and poly(aryl piperidinium) (e.g. PiperION® [4] Scheme 1b), polymer backbones. In addition, these membranes most commonly consist of quaternary ammonium-based [5], imidazolium-based [6], or piperidinium-based [7] functional headgroups.

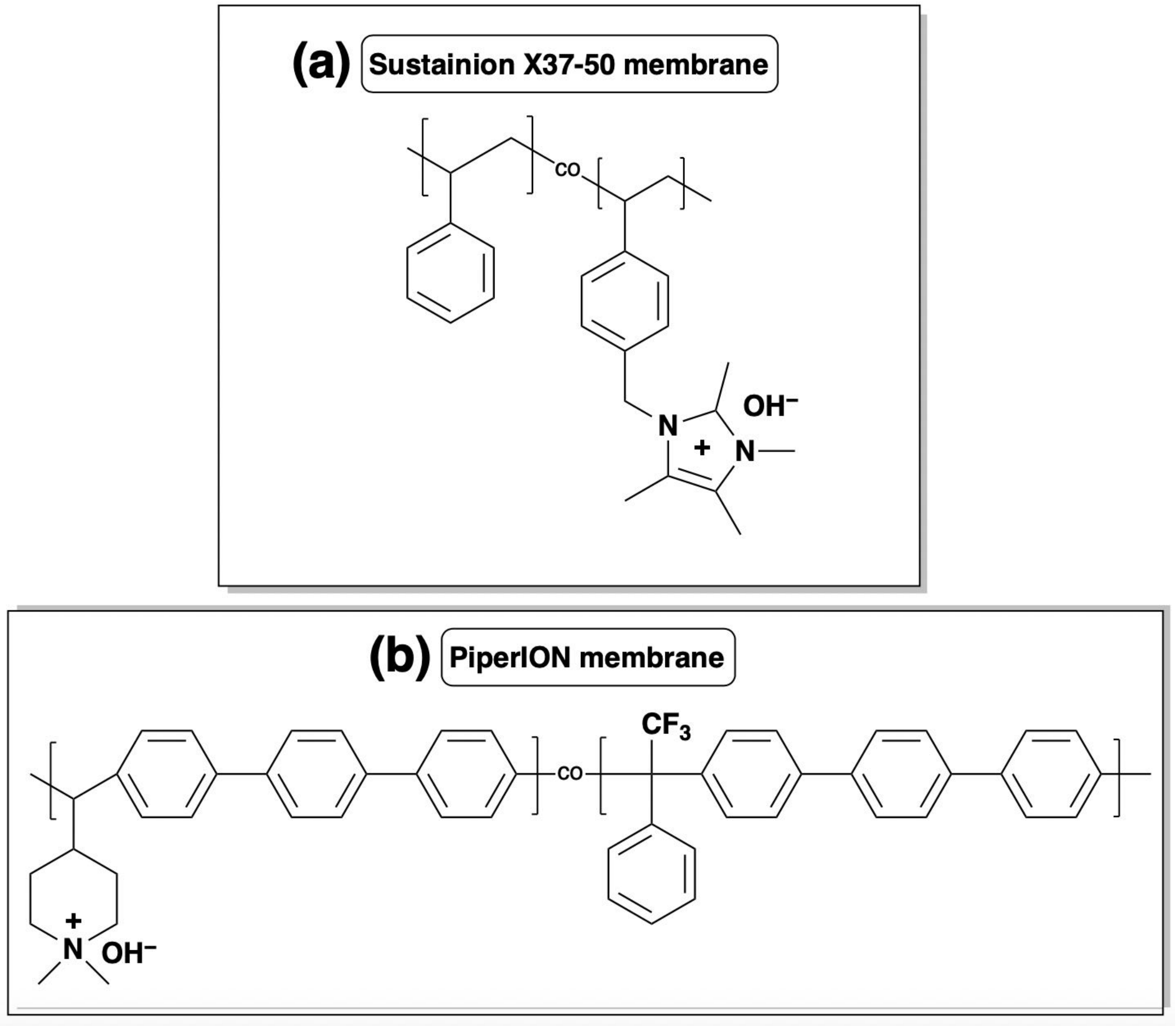

Scheme 1: *The chemical structure of (a) a poly(styrene)-based (Sustainion X37-50 membrane) (b) a poly(aryl piperidinium)-based (e.g. PiperION® membrane) anion exchange membranes.*

Despite the plethora of research conducted recently on developing highly hydroxide ion-conductive anion exchange membranes, with favourable thermal, alkaline, and mechanical durability [8], these membranes still suffer from low durability in practice [9]. There are several key properties affecting the performance and stability of anion exchange membranes. The ion exchange capacity is a pivotal parameter quantifying the number of exchange functional headgroups for hydroxide ion per weight (in grams) of dry polymer [10]. The ion exchange capacity is proportional to the hydroxide ion permeability through an anion exchange membrane, whereby higher ion exchange capacity indicates a higher number of functional headgroups, resulting in better ion permeability/conductivity. The ion conductivity is influenced by the area specific resistance (ASR) of the membrane as well, as shown in equation 1 [10].

$$\text{Ion conductivity (mS cm}^{-1}\text{)} = \frac{Membrane\ thickness}{ASR\ \text{(the membrane resistance × area)}} \qquad (1)$$

Furthermore, the water uptake and swelling ratios are two crucial parameters associated with the performance and stability of ion exchange membranes, due to their correlation to the ion exchange capacity and mechanical properties [11]. The water uptake ratio is proportional to the ion exchange capacity, whereby an anion exchange membrane with sufficient water uptake retains high hydrophilicity and ion conductivity [11,12]. However, an excessive water uptake (i.e. an excessive ion exchange capacity) can cause an over-swelling of the membrane structure (i.e. excessive expansion of the membrane due to water absorption), leading to a decrease in the mechanical stability and ion conductivity [11]. Therefore, the values of these parameters should be optimised to maintain optimal ion conductivity and mechanical stability in practice.

In the literature, various materials and synthetic strategies have been adopted for developing anion exchange membranes, including the radiation-grafting method. Radiation-grafted anion exchange membranes are membranes composed of backbones (e.g. low-density polyethylene and poly(ethylene-co-tetrafluoroethylene) containing anion exchange functional headgroups (e.g. trimethylammonium and imidazolium headgroups) [9,13]. The radiation grafting method consists of three main stages, starting with irradiation of a commercial polymer substrate in air (i.e. peroxidation) using a radiation source (e.g. electron beam), forming grafting sites (peroxides) for incorporating monomers onto the substrates' surface [14]. These radiation-activated (i.e. peroxidated) substrates are grafted with monomers (mostly vinylbenzyl chloride-based monomers [15]), followed by the amination of these grafted monomers [16,17]. A typical example of the radiation-grafting procedure to fabricate a radiation-grafted anion exchange membrane is shown in Scheme 2.

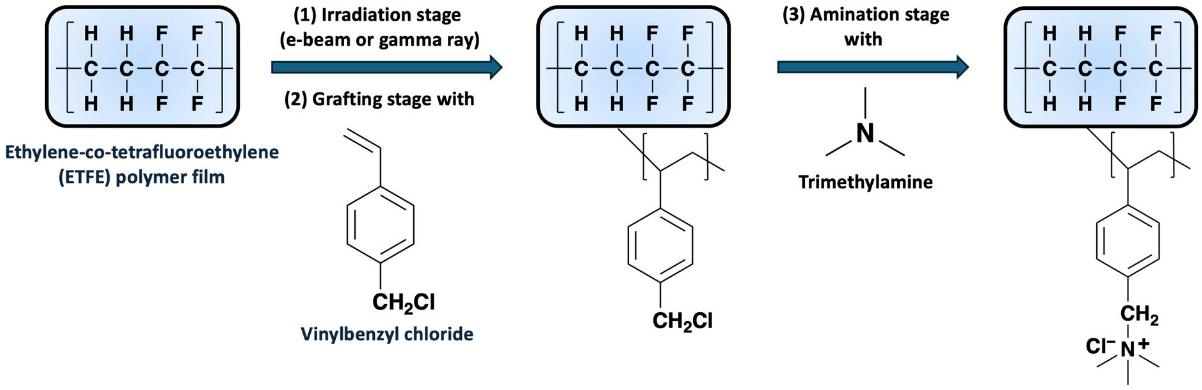

Scheme 2: *The key stages of the fabrication of a radiation-grafted anion exchange membrane: (1) irradiation of a polymer film in air (peroxidation); (2) followed by grafting the irradiated polymer film with monomers, working as functional headgroups; (3) followed by the amination of these functional headgroups.*

The radiation-grafted method is a simple and advantageous fabrication approach for anion exchange membranes in industrial scale applications, since a commercial substrate film can be used, and thus no polymer backbone formation step is required. In addition, fabricating anion exchange membranes containing the same backbone but with different grafted functional headgroups is facile, facilitating the investigation and comparison of various functional headgroup chemistries with different properties, such as ion exchange capacity, water uptake, and ionic conductivity [9,18].

Although radiation-grafted anion exchange membranes have attracted attention as polymer membranes in fuel cells since early 2000s, this type of membrane has rarely been reported in the context of water electrolysis [17]. Herein, a radiation-grafted anion exchange membrane synthesised and supplied by Prof. John Varcoe and his research team (University of Surrey, School of Chemistry and Chemical Engineering) was tested in the standard water electrolyser introduced in Chapter 3. This membrane was made by co-grafting vinylbenzyl chloride onto an electron-beam activated poly(ethylene-co-tetrafluoroethylene) (ETFE) film, followed by amination with trimethylamine. This membrane has previously been investigated by Willson *et al.* as a radiation-grafted anion exchange membrane in a CO_2 electrolyser, and these authors have already provided the full synthesis procedure and characterisation of the physiochemical properties of the membrane [18].

5.2. Experimental

5.2.1. Water electrolyser components, setup, and assembly

The same standard water electrolyser and the same components and conditions adopted in Chapter 3 were used to perform the experimental work (unless otherwise mentioned) [1]. An aqueous solution of 1 M KOH made using deionised water (resistivity = 15 MΩ-cm) was used across all experiments. This 1 M KOH solution, placed in two electrolyte reservoirs, was fed to both the anode and the cathode sides simultaneously using two MasterFlex$^{@}$ L/S peristaltic pumps (Cole-Parmer, UK) equipped with two pump heads (Masterflex Easy Load II pump head 77201-60). A radiation-grafted membrane (thickness = 25 μm, supplied by the University of Surrey, School of Chemistry and Chemical Engineering) and Fumasep FAA-3-50 membrane (thickness = 50 μm, supplied by FuelCellStore) were used as anion exchange membranes.

5.2.2. Liquid electrolyte characterisation

Inductively coupled plasma optical emission spectroscopy (ICP-OES), Agilent 5900 ICP-OES, equipped with an Agilent SPS4 autosampler) was used to detect any metal residuals after each stability test; after neutralising the 1 M KOH electrolytes with HNO_3 and diluting them 5-fold with 5% HNO_3. The ICP-OES samples were collected from the anolyte volume of 0.6 L (for testing all membranes) and catholyte volume of 0.85 L (for testing FAA-3-50) and 1.4 L (for testing ETFE membranes).

5.2.3. Anion exchange membrane pretreatment

The Fumasep FAA-3-50 membrane was delivered in a dry form, while the radiation-grafted membrane, referred to as the ETFE membrane throughout this Chapter, was supplied in deionised water. Both membranes were pre-treated before use. The membranes were submerged in 1 M KOH solution at room temperature (around 20 °C) for at least 24 h to convert them into the OH-form. They were kept under 1 M KOH in closed containers to prevent dryness and CO_2 contamination, in which CO_3^{2-} formation might influence the ionic conductivity.

5.2.4. Electrochemical characterisation

All the electrochemical tests were conducted using a BioLogic SP-150 potentiostat with an 80 A booster, following the same procedures adopted in Chapter 3 (unless mentioned otherwise). The data were acquired and analysed using EC-Lab@ software (version 11.43). In brief, a fixed potential of 2.0 V was applied for 1 h at 40 °C to activate the system, followed by measuring the polarisation curves over a potential range of 0 V to 2.0 V at 40 °C. Afterwards, electrochemical impedance spectroscopy tests were performed under the experimental parameters shown in Table 1, followed by chronopotentiometric tests (i.e. stability tests) carried out at 1.0 A cm^{-2} at 40 °C for a week (168 h).

Table 1: *The experimental parameters used in the electrochemical impedance spectroscopy.*

DC Potential (V)	2.0
AC Potential (mV rms)	100
Initial Frequency (kHz)	10
Final Frequency (mHz)	500
Points/Decade	6.0

5.2.5. Gas chromatography analysis

To measure the extent of crossover of H_2 through the membrane from the cathode side to anode side and to measure the H_2 gas produced at the cathode for Faradaic efficiency calculations, an Agilent 8860 gas chromatograph system was used. A flowchart mapping out all the gas samples taken (in order) for gas chromatography analysis is shown in Figure 1. In brief, all gas samples were taken from the headspace of electrolytes' reservoirs, starting with taking gas samples after purging the electrolytes with Ar for 30 min, followed by taking additional samples after applying a fixed current density of 1.0 A cm^{-2} every hour for 3 h. Subsequently, further gas samples were taken after performing the stability tests at 1.0 A cm^{-2} for a week for each test, followed by taking additional gas samples (after completing the stability tests) after purging the anolyte again with Ar for 30 min again. Afterwards, further samples were taken after applying a fixed current density of 1.0 A cm^{-2} for another 3 h (a gas sample was taken after each 1 h). At the beginning of each stability test, to calculate the Faradaic efficiency of the system, a gas sample was collected from the catholyte headspace after 2 min, 20 min, and 40 min (three samples in total), measuring the H_2 produced at the cathode during the water electrolysis process at a fixed current density of 1.0 A cm^{-2}.

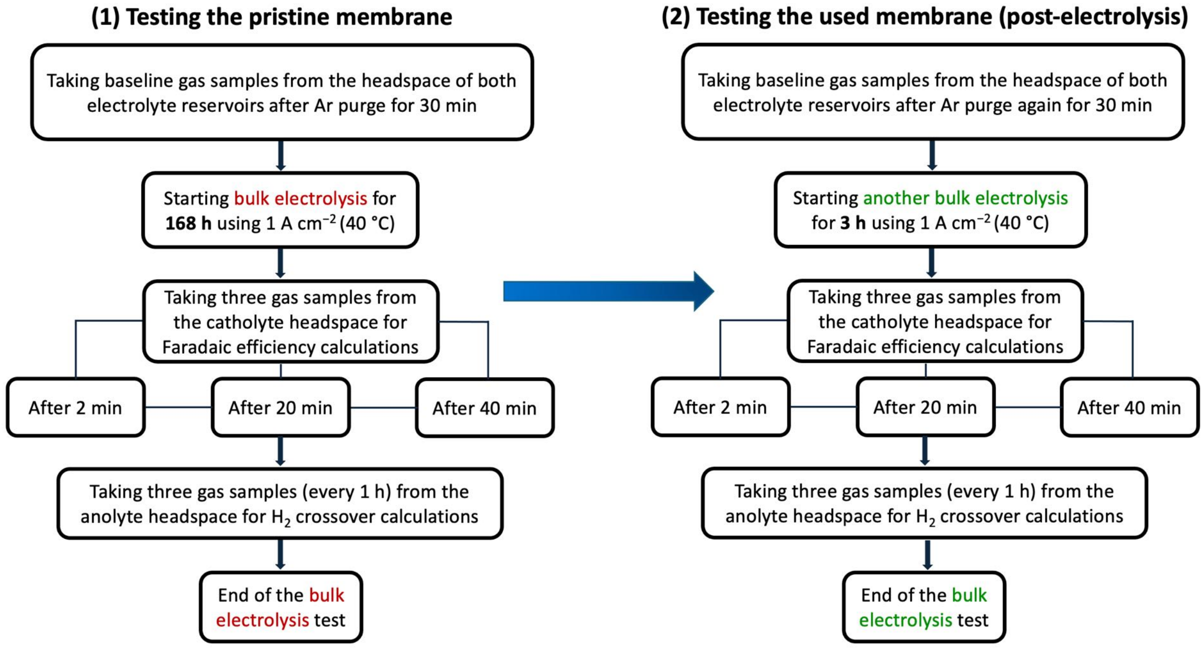

Figure 1: *A flowchart illustrating the sequential collection of gas samples from the headspace of the electrolyte reservoirs for gas chromatography analysis: (1) prior to and (2) following each stability test (bulk electrolysis at 1.0 A cm^{-2} for 168 h).*

Two different calibration curves for H_2 quantitative analysis were generated to correlate the peak areas (generated by the gas chromatography instrument) with the amount of H_2 expressed in moles. A calibration curve (Figure 2) was prepared to quantify the H_2 produced at the cathode side by injecting a standard high-purity H_2 gas (99.9%) using different volumes. The other calibration curve (Figure 3) was prepared to quantify the H_2 crossed over to the anode side by injecting four different standards of H_2 gas (1%, 2%, 3%, 5% H_2/argon standards).

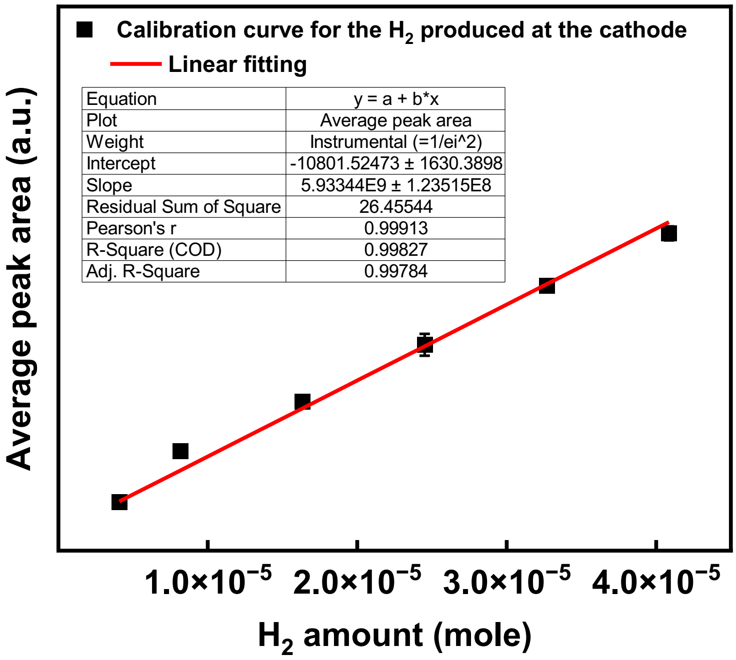

Equation	y = a + b*x
Plot	Average peak area
Weight	Instrumental (=1/ei^2)
Intercept	-10801.52473 ± 1630.3898
Slope	5.93344E9 ± 1.23515E8
Residual Sum of Square	26.45544
Pearson's r	0.99913
R-Square (COD)	0.99827
Adj. R-Square	0.99784

Figure 2: *A calibration curve plot generated by injecting various volumes of standard high-purity H_2 gas (99.9%) to quantify the H_2 produced at the cathode side.*

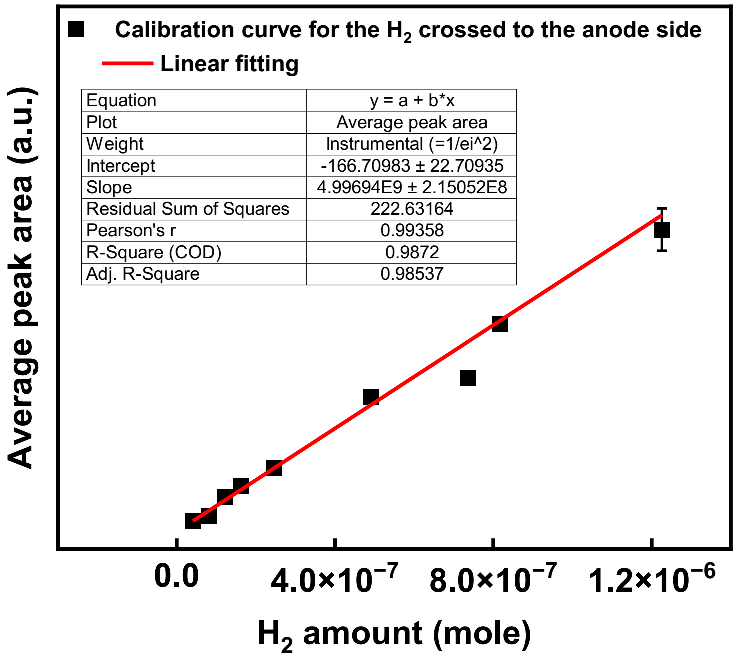

Equation	y = a + b*x
Plot	Average peak area
Weight	Instrumental (=1/ei^2)
Intercept	-166.70983 ± 22.70935
Slope	4.99694E9 ± 2.15052E8
Residual Sum of Squares	222.63164
Pearson's r	0.99358
R-Square (COD)	0.9872
Adj. R-Square	0.98537

Figure 3: *A calibration curve plot generated by injecting four different standards of* H_2 *gas (1%, 2%, 3%, 5%* H_2*/argon standards) using various volumes, to quantify the* H_2 *crossed over to the anode side.*

All the H_2 quantity values were calculated by considering the headspace of the electrolyte reservoirs and the gas microsyringe volume (400 μL) used to collect the H_2 gas samples, as shown in the following equation (equation 2).

$$The\ H_2\ quantity\ (in\ moles) = \frac{Hydrogen\ peak\ area \times headspace\ volume\ (L)}{\text{Calibration curve slope } \times 0.0004\text{ L (gas microsyringe volume)}} \quad (2)$$

The following equation (equation 3) was used to calculate the Faradaic efficiency:

$$\text{Faradaic efficiency} = \frac{2 \times a \times 96485.3\text{ C mol}^{-1}}{Q} \times 100 \quad (3)$$

where 2, a, and Q represent the number of electrons required for the hydrogen evolution reaction, the H_2 quantity (in moles) detected by gas chromatography, and the total charge passed during the water electrolysis process, respectively.

5.2.6. Scanning electron microscope imaging of the membranes

To investigate any possible morphological changes on the surface of the anion exchange membranes, scanning electron microscope top-surface images were taken of the pristine membranes and after long-term stability tests. The scanning electron microscope analysis was performed in the Geoanalytical Electron Microscopy and Spectroscopy (GEMS) facility at the School of Geographical and Earth Sciences, University of Glasgow, using a Zeiss Sigma variable-pressure field-emission scanning electron microscope under high vacuum conditions.

5.2.7. Fourier transform infrared (FT-IR) characterisation of the membranes

To investigate any possible chemical degradation of the radiation-grafted anion exchange membrane, FT-IR analysis was conducted using an infrared spectroscopy apparatus (Jasco (FT/IR-4100). The measurements were taken before and after each stability test, using these parameters: a scan number of 128, a resolution of 4.0 cm^{-1}, and a wavenumber range of 4000 to 600 cm^{-1}.

5.3. Results and discussion

5.3.1. Electrochemical measurements

The performance of the radiation-grafted anion exchange membrane (referred to as the ETFE membrane throughout this Chapter) was evaluated using a sheet of the membrane (thickness = 25 μm) or two sheets of the membrane to match the thickness (50 μm) of the FAA-3-50 membrane. The investigation was conducted in the standard anion exchange membrane water electrolyser using stainless steel fibre paper at the anode and carbon, commercially coated with 0.5 mg cm^{-2} Pt/C with Nafion dispersion - PTFE-treated (5 wt%), at the cathode. The stainless steel fibre paper was purchased from Dioxide Materials, USA, and the carbon cloth (W1S1011) was purchased from FuelCellStore, USA.

As shown in Figure 4, when two sheets of the ETFE membrane (50 μm) were used, similar performance to that of the FAA-3-50 membrane was observed, while a higher performance by around 50% was observed when only one ETFE membrane sheet was used. This higher performance was attributed to the enhanced ionic and water transport, along with a decrease in ohmic resistance (0.18 Ω cm^2 compared to ~ 0.22 Ω cm^2) observed in the thinner membrane configuration, as measured by electrochemical impedance spectroscopy [17–19].

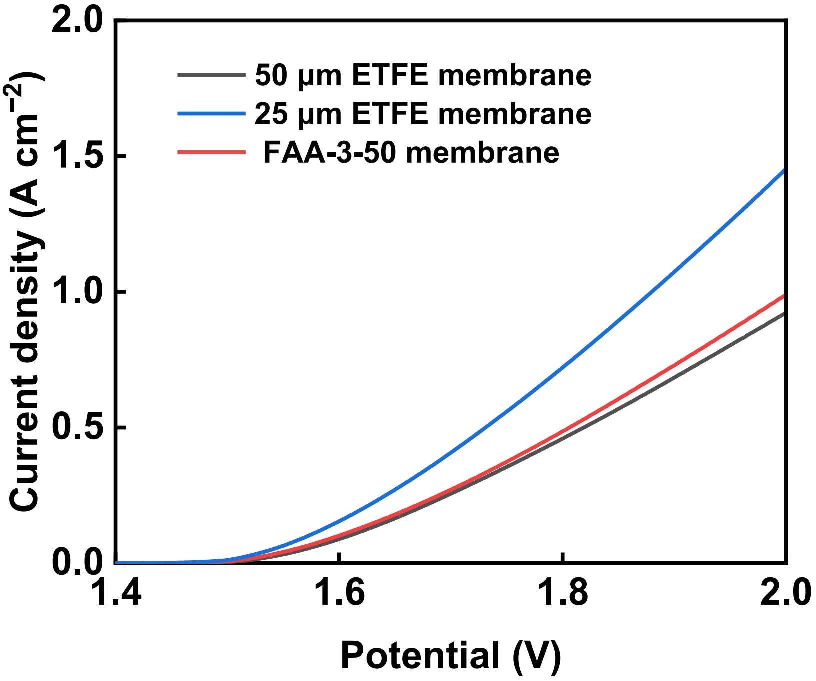

Figure 4: *Polarisation curves (at 40 °C) of the water electrolyser using either an FAA-3-50 membrane or two sheets or one sheet of the ETFE membrane, stainless steel fibre paper at the anode and 0.5 mg cm^{-2} Pt/C deposited carbon cloth at the cathode.*

The performance of the FAA-3-50 membrane and the ETFE membrane with two different thicknesses (25 μm and 50 μm) was compared by iR-correcting the potentials required to achieve 0.92 A cm^{-2}, corresponding to the current density delivered at 2.0 V using the 50 μm ETFE membrane. Due to the similar ohmic resistances (~ 0.22 Ω cm^{2}) of FAA-3-50 and 50 μm ETFE membranes, as measured by EIS at 2.0 V, the potential difference of ~ 20 mV between the two membranes remained constant, assuming that the ohmic resistance remains approximately constant at potentials near 2.0 V. On the other hand, after iR correcting the potentials required to achieve 0.92 A cm^{-2} for the 50 μm ETFE and 25 μm ETFE configurations, the potential difference between the two configurations decreased. The remaining potential difference might be attributed to mass transport limitations, as thicker membranes tend to hinder water diffusion through the membrane [20] and hydroxide ion diffusion between the membrane and catalyst layer [21], leading to higher concentration overpotential compared to thinner membranes.

The stability of each configuration was investigated by a galvanostatic electrolysis using a current density of 1.0 A cm^{-2} at 40 °C for a week (168 h). All the configurations showed similar behaviour, with an initial increase in the cell potential due to the potential creation of a mixed-oxide passivation layer on the stainless steel fibre paper at anodic potential [1], followed by a linear reduction in the cell potential over time (Figure 5). This behaviour was tentatively attributed to the enlargement of the pore (or ionic channel) size within the membranes' structures under the harsh stability test conditions [20].

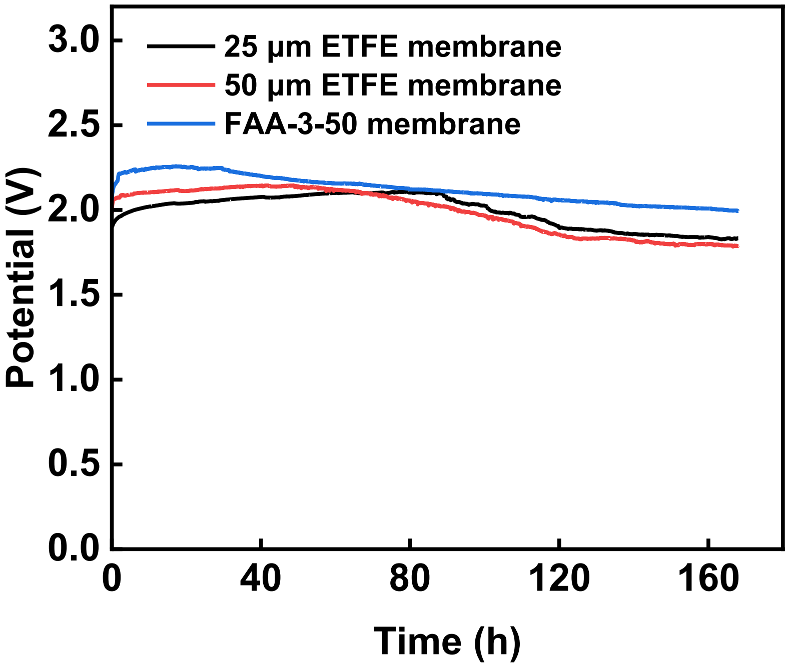

Figure 5: *The chronopotentiometric investigation of the water electrolyser for 168 h (at 40 °C) using either an FAA-3-50 membrane or two sheets or one sheet of the ETFE membrane, stainless steel fibre paper at the anode and 0.5 mg cm*$^{-2}$ *Pt/C deposited carbon cloth at the cathode.*

To investigate the possible enlargement of the pore size (or ionic channel size) within the membranes' structure, scanning electron microscope images were taken of the top surface of the ETFE and FAA-3-50 membranes in their pristine form and after each stability test. The ETFE membrane's structure did not show any change after the stability test (Figure 6). Additionally, the pore size within the FAA-3-50 membrane's structure apparently did not show any change as well although some debris from the carbon cloth and Pt/C covered some of these pores (Figure 7). Therefore, the enlargement of the pore (or ionic channel) size on the membranes' structure was excluded on the basis of the scanning electron microscope images.

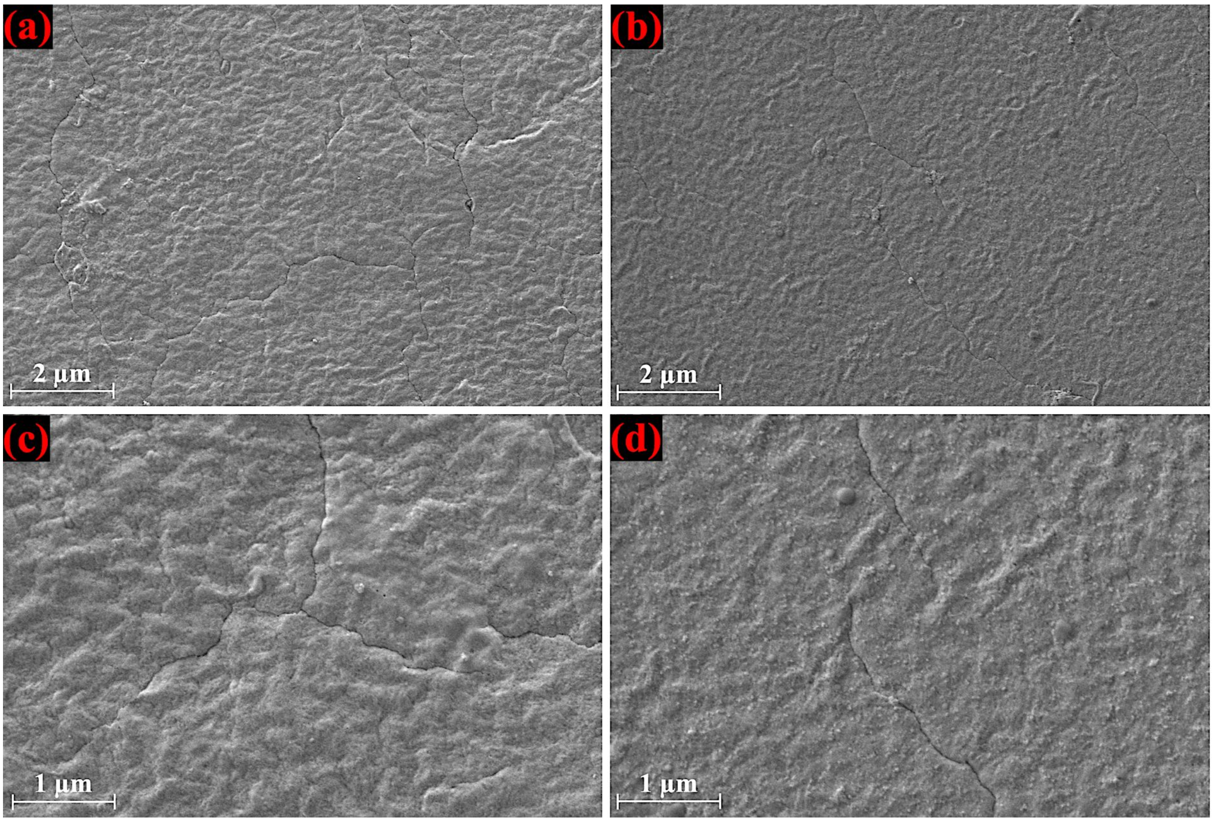

***Figure 6:** Scanning electron microscope images of the ETFE membrane in its pristine form (images: a and c) and after the galvanostatic electrolysis for 168 h at 40 °C (images: b and d).*

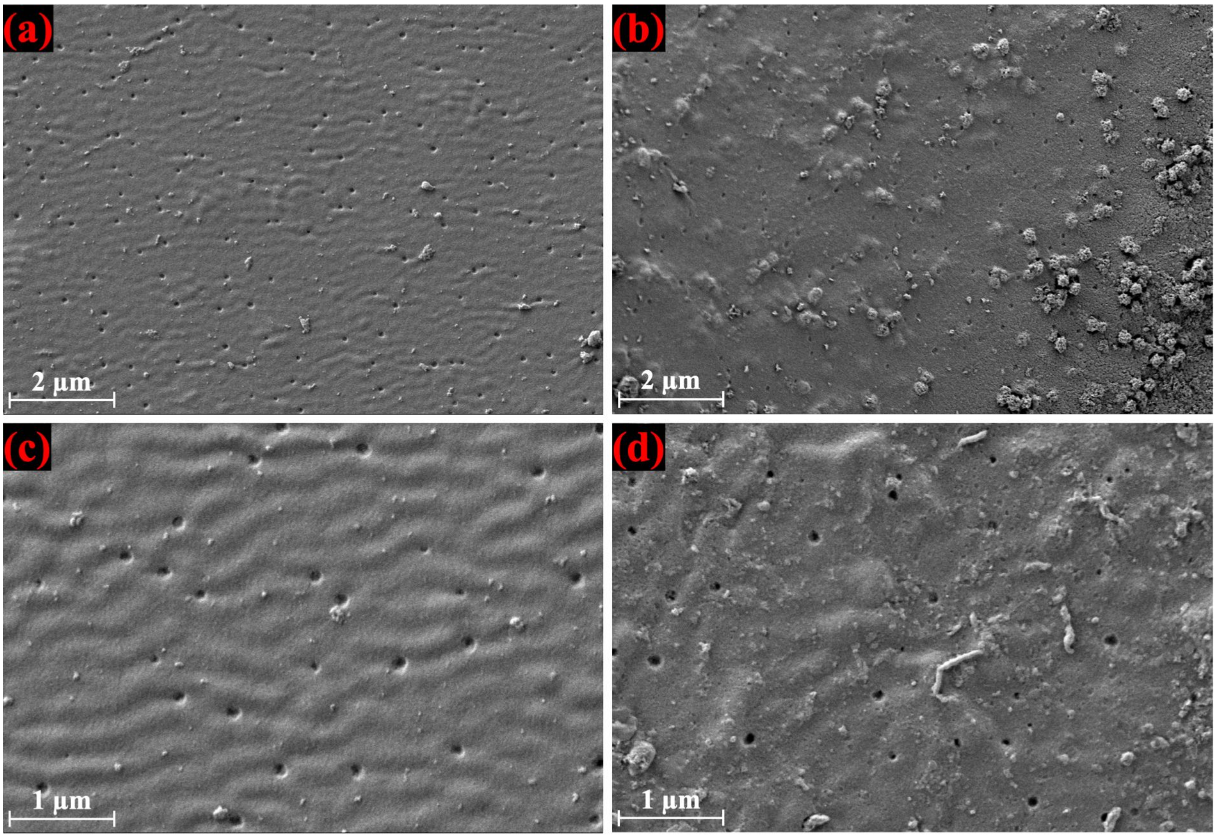

Figure 7: *Scanning electron microscope images of the FAA-3-50 membrane in its pristine form (images: a and c) and after the galvanostatic electrolysis for 168 h at 40 °C (images: b and d).*

Another potential cause of the reduction in the cell potential during the stability tests was attributed to the generation of short-circuit pathways because of the degradation of the membranes under the harsh operating conditions [22,23]. The water electrolyser was held at the minimum potential (1.23 V) theoretically required to split water molecules, where no anodic current density is anticipated, before and after the stability test of the FAA-3-50 membrane (Figure 8). As expected, no anodic current density was observed at 1.23 V in the membrane's pristine form. In contrast, when a potential cell of 1.23 V was held after the end of the stability test, an anodic current density of ~ 185 mA cm^{-2} was generated, signifying the presence of short-circuiting pathways between the cathode and anode sides. This current is known as a shunt current (i.e. parasitic current), where a portion of the charge flows through the liquid electrolyte or other unintended pathways [24]. The same test for the ETFE membrane could not be measured as insufficient quantities of the membrane were available. The presence of short-circuiting pathways was confirmed by spotting aligned hotspots on the stainless steel fibre and membrane surfaces after dismantling the flow cell (Figure 9).

A similar method to that applied by Ranza *et al.* [25] was conducted to measure the shunt current, wherein a FAA-3-50 membrane was used as the anion exchange membrane. In their case, after testing the membrane for 68 h at a constant current density of 0.5 A cm^{-2} at 60 °C (using 1 M KOH), their water electrolyser was then held at 1.3 V, showing a shunt current of 25 mA cm^{-2}.

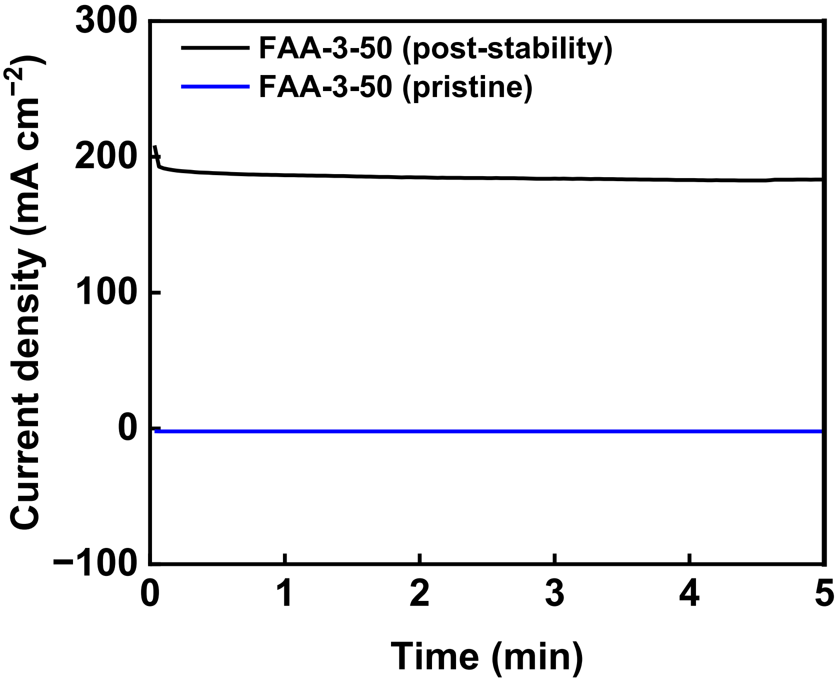

Figure 8: *The chronoamperometric investigation of the water electrolyser at 1.23 V before (i.e. in membrane's pristine form) and after 168 h operational electrolysis at 1.0 A cm^{-2} (at 40 °C) using an FAA-3-50 membrane.*

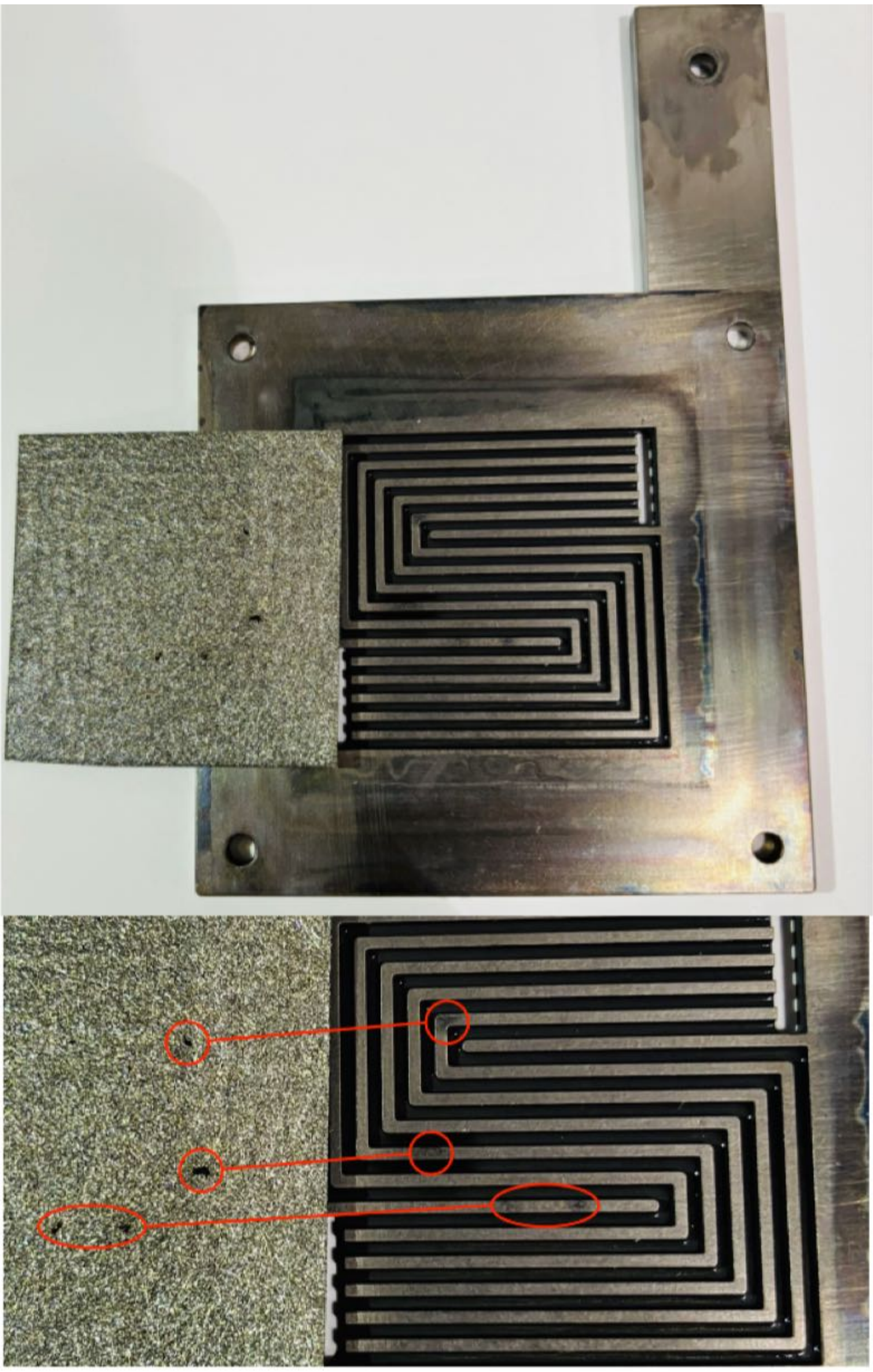

Figure 9: *Photographs of a bipolar plate and the stainless steel fibre paper after the 168 h galvanostatic stability test at a current density of 1.0 A cm*$^{-2}$ *(at 40 °C), showing hotspots on the surface of the bipolar plate and stainless steel fibre paper formed due to short-circuiting pathway formation.*

To investigate the influence of any catalyst leaching on the stability tests, an ICP-OES sample was taken from the anolyte and catholyte after each stability test. An Fe content of 0.004 – 0.008 mg cm^{-2} was observed in the anolyte, while no Ni content was observed in the anolyte among all configurations. No detectable Pt content in the catholyte was observed in the catholytes, signifying a high stability of the Pt/C catalyst at the cathode. All the results are listed in Table 2.

Table 2: *The Fe and Ni content detected in the anolyte and Pt content detected in the catholyte, after stability tests for 168 h at a fixed current density of 1.0 A cm^{-2} at 40 °C. The values were calculated by accounting for the volume of electrolytes circulating in the cell at the time of sample collection, catholyte = 0. 85 L (for FAA-3-50) and 1.4 L (for ETFE) and anolyte = 0.6 L (for all membranes), then normalised to the geometric area of the GDLs (13.7 cm^{2}).*

Membrane	**Fe content in anolyte (mg cm^{-2})**	**Ni concentration in anolyte (mg L^{-1})**	**Pt concentration in catholyte (mg L^{-1})**
25 µm ETFE	0.004	< 0.02	< 0.02
50 µm ETFE	0.008	< 0.02	< 0.02
FAA-3-50	0.008	< 0.02	< 0.02

5.3.2. Faradaic efficiency and H_2 crossover measurements

At 1.0 A cm^{-2}, the Faradaic efficiency of the water electrolyser using either two sheets of the ETFE membrane or the FAA-3-50 membrane was measured by collecting three gas samples from the catholyte headspace at the beginning and after each stability test, as illustrated in Figure 1. The Faradaic efficiency calculated using the first gas sample collected 2 min after bulk electrolysis (at 1.0 A cm^{-2}) for each configuration was similar (~ 92%), and it dropped afterwards (Figure 5). The reduction in Faradaic efficiency was attributed to the leakage of H_2 gas from the catholyte reservoir, as detected by an electrochemical H_2 gas sensor (UST, Germany), due to the pressure effect inside the reservoir. After the stability test for 168 h, another electrolysis operation was conducted, showing a significant reduction in Faradaic efficiency for each membrane (compared to measuring the membranes in their pristine form), starting at 2 min of electrolysis (Figure 10). This significant electrolyser efficiency loss was attributed to the short-circuiting pathway formation [22,23], alongside with the hydrogen escaping from the reservoir.

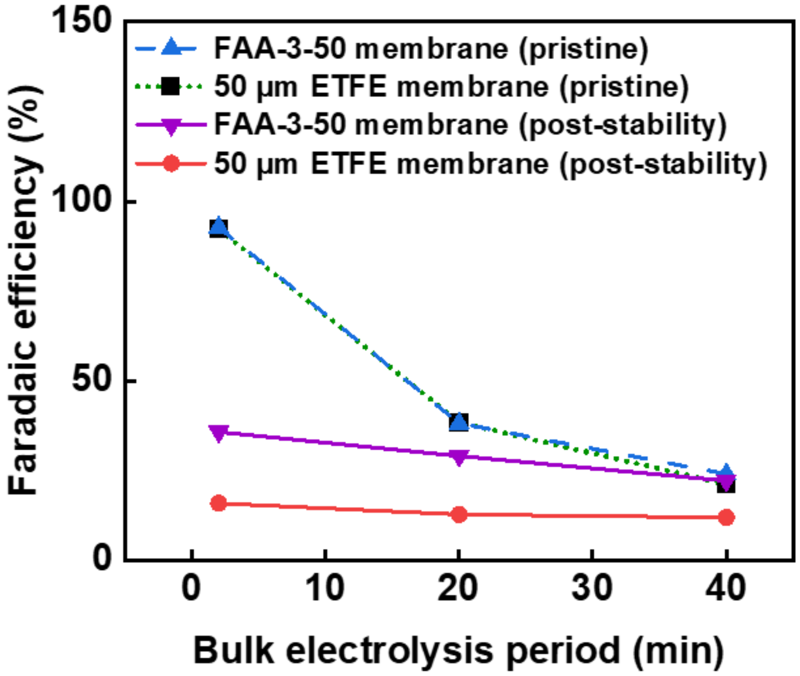

Figure 10: *The Faradaic efficiency measurements of the water electrolyser before (i.e. in the membranes' pristine form) and after 168 h operational electrolysis at 1.0 A cm*$^{-2}$ *(at 40 °C) using either two sheets of ETFE membrane or the FAA-3-50 membrane.*

The H_2 crossover rate measurements were taken 3 times after bulk electrolysis at 1.0 A cm^{-2} for 3 h (a gas sample was taken after each 1 h) in the membranes' pristine form and after each stability test. The two membranes showed similar H_2 crossover behaviour (Figure 11 and Table 3) with higher H_2 crossover rate after the stability test for 168 h compared to both membranes in their pristine form. The higher H_2 crossover rate after the stability test was attributed to the short-circuiting pathway formation under the harsh long-term stability test conditions.

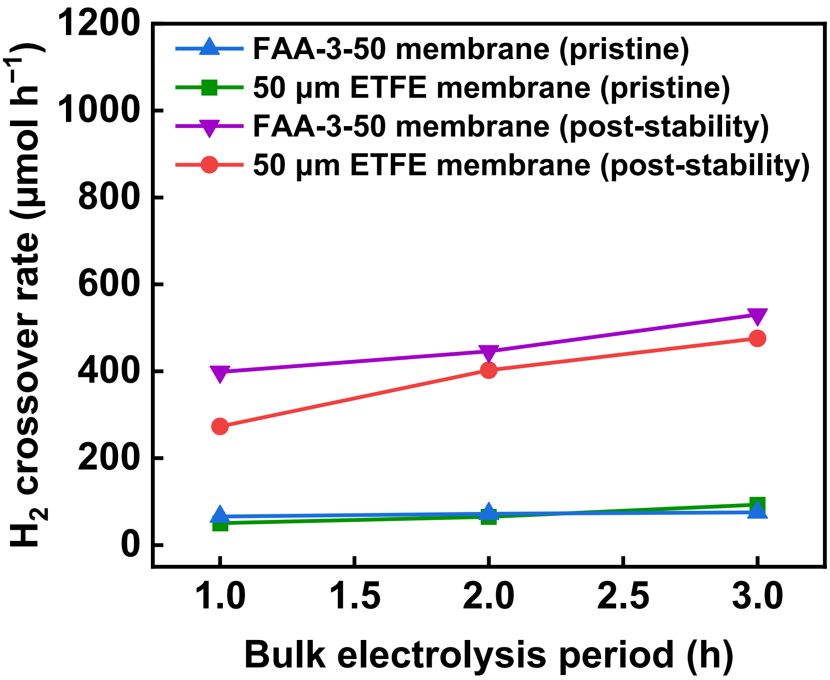

Figure 11: *The* H_2 *crossover rate measurements of the water electrolyser before (i.e. in membranes' pristine form) and after 168 h operational electrolysis at 1.0 A* cm^{-2} *(at 40 °C) using either two sheets of ETFE membrane or a FAA-3-50 membrane.*

Table 3: *The extent of H_2 crossover into the anolyte headspace observed after 1 h, 2 h, and 3 h of electrolysis, performed before and after a 168 h galvanostatic stability test. In all cases, a current density of 1.0 A cm^{-2} was applied at 40 °C.*

H_2 in anolyte headspace (µmol) **Membrane condition (electrolysis period)**	**Two sheets of ETFE membrane**	**FAA-3-50 membrane**
Pristine form (after 1 h)	50	66
Pristine form (after 2 h)	65	72
Pristine form (after 3 h)	93	75
Post-stability (after 1 h)	273	398
Post-stability (after 2 h)	403	446
Post-stability (after 3 h)	475	530

5.3.3. Fourier transform infrared (FT-IR) measurements

To investigate any change in the polymer matrix of the ETFE membrane after the stability test for 168 h at 1.0 A cm^{-2} (at 40 °C), FT-IR measurements were taken on the membrane in its pristine form and after the stability test. The ETFE membrane retained its chemical structure, whereby the following characteristic peaks did not disappear after the stability test (Figure 12):

the O–H stretching vibration (~ 3400 cm^{-1}), the aromatic C=C stretches (1638 cm^{-1} and 1475 cm^{-1}), and the strong C–F stretches (1000-1400 cm^{-1}) [26,27].

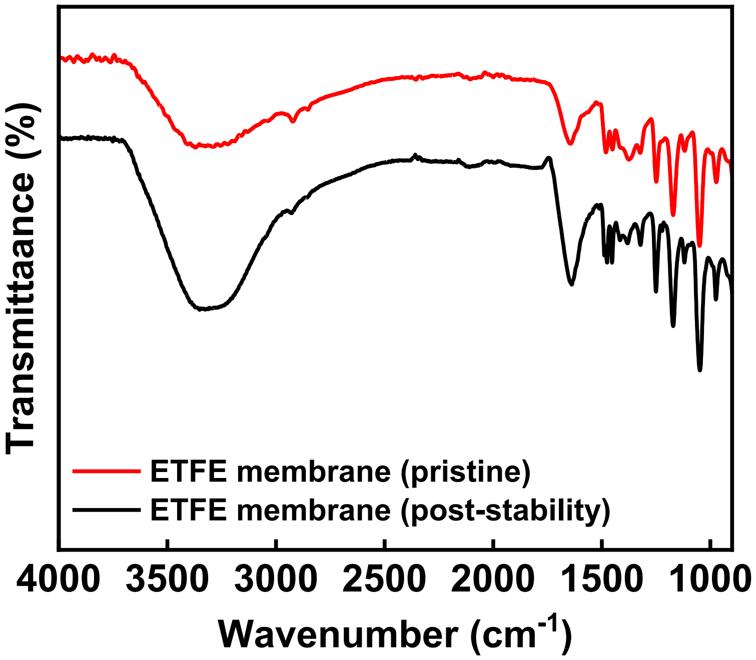

Figure 12: *The Fourier transform infrared spectroscopy (FT-IR) spectra of the ETFE membrane before (i.e. in its pristine form) and after 168 h operational electrolysis at 1.0 A* cm^{-2} *(at 40 °C).*

5.4. Conclusions

In this Chapter, a radiation-grafted anion exchange membrane, supplied by a research group in the University of Surrey was evaluated using my standard anion exchange membrane water electrolyser introduced in Chapter 3. The membrane exhibited similar performance, ohmic resistance, stability, and H_2 crossover characteristics to those of the commercial FAA-3-50 membrane when evaluated as two-sheet configuration (50 µm). Although 50% performance improvement was observed when one sheet of the membrane (25 µm) was used, significant H_2 crossover to the anode side was observed due to the membrane's low thickness. Regarding the membranes' stability, a linear decrease in the cell potential required to maintain 1.0 A cm^{-2} for 168 h was observed for all configurations, due to the formation of short-circuiting pathways between the cathode and anode sides under the harsh long-term electrolysis conditions. The short-circuiting pathway formation was confirmed by observing aligned hotspots on the surfaces of the stainless steel fibre paper and membrane, which perfectly faced each other when overlaid, after disassembling the flow cell. In addition, the substantial loss in Faradaic efficiency and increase in H_2 crossover measured after the stability test for 168 h, also suggest the formation of the short-circuiting pathways.

References

[1] A.H. Faqeeh, M.D. Symes, A standard electrolyzer test cell design for evaluating catalysts and cell components for anion exchange membrane water electrolysis, Electrochim. Acta 444 (2023) 142030, https://doi.org/10.1016/j.electacta.2023.142030.

[2] W. da Silva Freitas, B. Mecheri, C. Lo Vecchio, I. Gatto, V. Baglio, V.C.A. Ficca, A. Patra, E. Placidi, A. D'Epifanio, Metal-organic-framework-derived electrocatalysts for alkaline polymer electrolyte fuel cells, J. Power Sources 550 (2022) 232135, https://doi.org/10.1016/j.jpowsour.2022.232135.

[3] J. Wang, Y. Zhao, B.P. Setzler, S. Rojas-Carbonell, C. Ben Yehuda, A. Amel, M. Page, L. Wang, K. Hu, L. Shi, S. Gottesfeld, B. Xu, Y. Yan, Poly(aryl piperidinium) membranes and ionomers for hydroxide exchange membrane fuel cells, Nat. Energy 4 (2019) 392–398, https://doi.org/10.1038/s41560-019-0372-8.

[4] J.J. Kaczur, H. Yang, Z. Liu, S.D. Sajjad, R.I. Masel, Carbon dioxide and water electrolysis using new alkaline stable anion membranes, Front. Chem. 6 (2018) 263, https://doi.org/10.3389/fchem.2018.00263.

[5] J. Qian, C. Wang, X. Zhang, J. Hu, X. Zhao, J. Li, Q. Ren, Quaternary ammonium-functionalized crosslinked poly(aryl ether sulfone)s anion exchange membranes with enhanced alkaline stability for water electrolysis, J. Memb. Sci. 685 (2023) 121946, https://doi.org/10.1016/j.memsci.2023.121946.

[6] J. Qian, C. Wang, X. Zhang, X. Zhao, J. Li, Q. Ren, Dense 1,2,4,5-tetramethylimidazolium-functionlized anion exchange membranes based on poly(aryl ether sulfone)s with high alkaline stability for water electrolysis, Int. J. Hydrogen Energy 48 (2023) 8165–8178, https://doi.org/10.1016/j.ijhydene.2022.11.258.

[7] X. Chu, Y. Shi, L. Liu, Y. Huang, N. Li, Piperidinium-functionalized anion exchange membranes and their application in alkaline fuel cells and water electrolysis, J. Mater. Chem. A Mater. 7 (2019) 7717–7727, https://doi.org/10.1039/C9TA01167F.

[8] N. Chen, Y.M. Lee, Anion exchange polyelectrolytes for membranes and ionomers, Prog. Polym. Sci. 113 (2021) 101345, https://doi.org/10.1016/j.progpolymsci.2020.101345.

[9] K.L. Lim, C.Y. Wong, W.Y. Wong, K.S. Loh, S. Selambakkannu, N.A.F. Othman, H. Yang, Radiation-grafted anion-exchange membrane for fuel cell and electrolyzer applications: A mini review, Membranes 11 (2021) 397, https://doi.org/10.3390/membranes11060397.

[10] D. Henkensmeier, M. Najibah, C. Harms, J. Žitka, J. Žitka, K. Bouzek, Overview : State-of-the Art Commercial Membranes for Anion Exchange Membrane Water Electrolysis, J. Electrochem. En. Conv. Stor. 18 (2021) 024001, https://doi.org/10.1115/1.4047963.

[11] J. Luque Di Salvo, G. De Luca, A. Cipollina, G. Micale, Effect of ion exchange capacity and water uptake on hydroxide transport in PSU-TMA membranes: A DFT and molecular dynamics study, J. Memb. Sci. 599 (2020) 117837, https://doi.org/10.1016/j.memsci.2020.117837.

[12] R.S. Kingsbury, K. Bruning, S. Zhu, S. Flotron, C.T. Miller, O. Coronell, Influence of Water Uptake, Charge, Manning Parameter, and Contact Angle on Water and Salt Transport in Commercial Ion Exchange Membranes, Ind. Eng. Chem. Res. 58 (2019) 18663–18674, https://doi.org/10.1021/acs.iecr.9b04113.

[13] O.I. Deavin, S. Murphy, A.L. Ong, S.D. Poynton, R. Zeng, H. Herman, J.R. Varcoe, Anion-exchange membranes for alkaline polymer electrolyte fuel cells: Comparison of pendent benzyltrimethylammonium- and benzylmethylimidazolium-head-groups, Energy Environ. Sci. 5 (2012) 8584–8597, https://doi.org/10.1039/c2ee22466f.

[14] W.H. Lee, C. Crean, J.R. Varcoe, R. Bance-Soualhi, A Raman spectro-microscopic investigation of ETFE-based radiation-grafted anion-exchange membranes, RSC. Adv. 7 (2017) 47726–47737, https://doi.org/10.1039/c7ra09650j.

[15] E.J. Park, P. Jannasch, K. Miyatake, C. Bae, K. Noonan, C. Fujimoto, S. Holdcroft, J.R. Varcoe, D. Henkensmeier, M.D. Guiver, Y.S. Kim, Aryl ether-free polymer electrolytes for electrochemical and energy devices, Chem. Soc. Rev. 53 (2024) 5704–5780, https://doi.org/10.1039/d3cs00186e.

[16] A.L.G. Biancolli, D. Herranz, L. Wang, G. Stehlíková, R. Bance-Soualhi, J. Ponce-González, P. Ocón, E.A. Ticianelli, D.K. Whelligan, J.R. Varcoe, E.I. Santiago, ETFE-based anion-exchange membrane ionomer powders for alkaline membrane fuel cells: A

first performance comparison of head-group chemistry, J. Mater. Chem. A Mater. 6 (2018) 24330–24341, https://doi.org/10.1039/c8ta08309f.

[17] A.L.G. Biancolli, B. Chen, A.S. Menandro, F.C. Fonseca, E.I. Santiago, S. Holdcroft, Radiation-grafted anion-exchange membranes: key features for enhanced water electrolysis, J. Mater. Chem. A Mater. 12 (2024) 21442–21454, https://doi.org/10.1039/d4ta02354d.

[18] C.A. Giron Rodriguez, B.Ó. Joensen, A.B. Moss, G.O. Larrazábal, D.K. Whelligan, B. Seger, J.R. Varcoe, T.R. Willson, Influence of Headgroups in Ethylene-Tetrafluoroethylene-Based Radiation-Grafted Anion Exchange Membranes for CO_2 Electrolysis, ACS Sustain. Chem. Eng. 11 (2023) 1508–1517, https://doi.org/10.1021/acssuschemeng.2c06205.

[19] M.S. Thomassen, A.H. Reksten, A.O. Barnett, T. Khoza, K. Ayers, PEM water electrolysis in: Electrochemical Power Sources: Fundamentals, Systems, and Applications, Elsevier B.V., Amsterdam, 2022, pp. 199-228, https://doi.org/10.1016/b978-0-12-819424-9.00013-6.

[20] M. Müller, M. Carmo, A. Glüsen, M. Hehemann, S. Saba, W. Zwaygardt, D. Stolten, Water management in membrane electrolysis and options for advanced plants, Int. J. Hydrogen Energy 44 (2019) 10147–10155, https://doi.org/10.1016/j.ijhydene.2019.02.139.

[21] K. Yassin, R. Attias, Y. Tsur, D.R. Dekel, Identifying and Quantifying Loss Sources in Anion-Exchange Membrane Water Electrolyzers, ACS Electrochem. (2025). https://doi.org/10.1021/acselectrochem.4c00156.

[22] M. Petitjean, M. Reytier, A. Chatroux, L. Bruguière, A. Mansuy, H. Sassoulas, S. Di Iorio, B. Morel, Performance and Durability of High Temperature Steam Electrolysis: From the Single Cell to the Short-Stack Scale, ECS Trans. (2011) 2905, https://doi.org/10.1149/ma2011-01/12/1007.

[23] L. Singh, A.G. Miller, L. Wang, H. Liu, Scaling-up up-flow microbial electrolysis cells with a compact electrode configuration for continuous hydrogen production, Bioresour. Technol. 331 (2021) 125030, https://doi.org/10.1016/j.biortech.2021.125030.

[24] M. Quentmeier, B. Schmid, H. Tempel, R.A. Eichel, Modular CO_2-to-CO Electrolysis Short-Stack Design─Impact of Temperature Gradients and Insights into Position-Dependent Cell Behavior, ACS Sustain. Chem. Eng. 12 (2024) 3876–3885, https://doi.org/10.1021/acssuschemeng.4c00630.

[25] M. Ranz, B. Grabner, B. Schweighofer, H. Wegleiter, A. Trattner, Deciphering Anion Exchange Membrane Water Electrolysis: A Distribution of Relaxation Times Approach, ECS Trans. 114 (2024) 483–492, https://doi.org/10.1149/11405.0483ecst.

[26] T. Zhou, R. Shao, S. Chen, X. He, J. Qiao, J. Zhang, A review of radiation-grafted polymer electrolyte membranes for alkaline polymer electrolyte membrane fuel cells, J. Power Sources 293 (2015) 946–975, https://doi.org/10.1016/j.jpowsour.2015.06.026.

[27] J. Fang, Y. Yang, X. Lu, M. Ye, W. Li, Y. Zhang, Cross-linked, ETFE-derived and radiation grafted membranes for anion exchange membrane fuel cell applications, Int. J. Hydrogen Energy 37 (2012) 594–602, https://doi.org/10.1016/j.ijhydene.2011.09.112.

Final Conclusions and Future Perspectives

In this thesis, a standard anion exchange membrane water electrolyser was built and optimised using various configurations of membrane-electrode assembly, which is the heart of any water electrolyser. The aim was to design a benchmark anion exchange membrane water electrolyser system to be adopted universally as a baseline to assess novel anion exchange membrane water electrolyser components. Additionally, the flow cell used to build the standard water electrolyser can be used in other electrolysis applications, such as proton exchange membrane water electrolysis.

In **Chapter 3**, the construction, operation, and characterisation of the standard anion exchange membrane water electrolyser were described in detail and published as an open access paper "A.H. Faqeeh, M.D. Symes, A standard electrolyzer test cell design for evaluating catalysts and cell components for anion exchange membrane water electrolysis, Electrochim. Acta 444 (2023) 142030, https://doi.org/10.1016/j.electacta.2023.142030". Additionally, 3D drawing CAD files for the flow cell materials were made to allow others to procure the same such materials when they come to reproduce the flow cell. These files are available for download from the University of Glasgow's open access data repository: https://researchdata.gla.ac.uk/1672/. Although the standard water electrolyser demonstrated excellent performance, the aim was not to report a cell with record performance. Instead, the main aim was on providing a detailed description of the construction, operation, and characterisation of a testbed cell for others to use for evaluating and comparing novel water electrolyser components. We arranged for numerous flow cells of this design to be mass machined by an industrial party to be distributed and used by other colleagues. For example, such a flow cell was sent to a research group based at RWTH Aachen University, Germany. The research group managed to reproduce the results reported in Chapter 3; however, they have not managed to operate the water electrolyser for the full 205 h stability measurement yet. Further optimisation of the standard anion exchange membrane water electrolyser can be achieved through investigating the effect of changing other operating parameters, such as flow rate and gasket thickness. Moreover, further work to aid the standardisation of procedures for anion exchange membrane water electrolysers that should be addressed include the establishment of a standardised optimal protocol for catalyst deposition on either gas diffusion layers or anion exchange membranes. This step will contribute to a more comprehensive evaluation of future advancements in the field.

In **Chapter 4**, due to the constrained supply of Nafion and Aquivion proton exchange membranes at the time of writing this Chapter, an alternative new commercially available perfluorinated sulfonic acid membrane (PFSA D170-U) was evaluated in a water electrolyser. The performance, stability and H_2 crossover characteristic of this new membrane were investigated and compared to those of Nafion and Aquivion membranes, using the flow cell introduced in Chapter 3. The three membranes showed similar metrics, positioning PFSA D170-U as a promising alternative proton exchange membrane for water electrolysis applications. Given the modest performance of the non-hot-pressed membrane electrode assembly, it is recommended to use a hot-pressing method for catalyst-coated substrate fabrication to improve interfacial contact between catalyst layer and membrane, potentially enhancing performance. Further characterisation measurements of the physiochemical properties of the PFSA D170-U membrane, such as ion exchange capacity (to assess the retention of proton conductivity) and water uptake and swelling ratios (to evaluate dimensional stability), should be performed before and after long-term stability tests to assess changes in the physiochemical properties of the membrane. Moreover, the mechanical and chemical stability of the PFSA D170-U membrane under industrial-scaled operating conditions should be evaluated through extended continuous stability tests (beyond 1000 h) or accelerated stress tests. While perfluorosulfonic acid (PFSA) membranes remain the state-of-the-art proton exchange membrane in terms of their long-term durability, there are environmental impact and health concerns related to their manufacturing and decomposition, arising from the release of perfluorinated compounds and polyfluoroalkyl substances (PFAS) into groundwater [1]. Therefore, non-fluorinated hydrocarbon-based proton exchange membranes should be assessed as alternatives, since such membranes offer environmental and economic advantages [2], and they can operate at higher temperatures (beyond 100 °C) [3]. However, their mechanical durability remains a key limitation [4,5]. Therefore, future research should focus on improving the mechanical durability of hydrocarbon-based membranes to make them viable and sustainable alternative to PFSA membranes in industrial applications.

In **Chapter 5**, the standard anion exchange membrane water electrolyser was adopted to evaluate a radiation-grafted anion exchange membrane (ETFE membrane) supplied by a collaborative research team based at the University of Surrey. The electrochemical performance, ohmic resistance, stability, and H_2 crossover characteristic of the radiation-grafted anion exchange membrane were evaluated and compared to those of Fumasep FAA-3-55 (a membrane available commercially). Both membranes showed similar metrics, mostly importantly they both showed low mechanical durability under the electrolysis conditions, as confirmed by spotting hotspots on the anode electrode and bipolar plates, probably arising from having short-circuiting pathways between the cathode and anode sides inside the electrolyser. Since the radiation-grafted membrane showed low durability using 1 M KOH, it should be tested at lower alkaline concentrations (0.1 M – 0.5 M) to mitigate the membrane degradation induced by the exposure to OH^- ions, though this will increase ohmic resistance, resulting in lower performance [6]. In addition, the physiochemical properties of the ETFE membrane, such as ion exchange capacity and water uptake and swelling ratios, should be compared before and after the stability tests to assess changes in the physiochemical properties of the membrane.

Looking ahead to the future of the green hydrogen production electrolyser technologies, there is an urgent need for developing high-performance, high-durable, and economically viable OER and HER catalysts. Therefore, adopting standardised electrolysers and evaluation protocols for these catalysts (and indeed other cell components) is crucial to systematically compare the performance and durability of these materials under the same testing conditions across studies. Moreover, due to the critical environmental concerns arising from the contamination caused by the manufacturing and decomposition of PFSA membranes, PFSA-free alternative proton exchange membranes with enhanced mechanical, thermal, and chemical durability should be developed. For anion exchange membrane water electrolysers, the development of anion exchange membranes with high alkaline stability and ion conductivity is an urgent priority to advance this technology. Multiple promising directions are emerging for the future development of anion exchange membranes. The alkaline stability of the membranes can be enhanced by designing membrane structures with the minimum amount of β-H, inhibiting Hofmann elimination, and increasing steric hindrance near the functional headgroups, protecting the membrane from OH^- attack. In addition, the replacement of β-hydrogens with electron-donating groups (e.g. methyl and butyl) near the functional headgroups can help in mitigating the OH^- attack by increasing the electron density of the cation [7]. In terms of ion conductivity, it can be achieved mainly by increasing the ion exchange capacity of the membrane (i.e. increasing number of functional headgroups per dry membrane weight). However, an excessive ion exchange capacity elevates water uptake and swelling, consequently decreases the mechanical strength of the membrane [8]. An effective approach to enhance the alkaline stability and ion conductivity, while preserving the mechanical strength of the membrane, is the formation of hydrophilic/hydrophobic microphase separation within membranes. In microphase-separated anion exchange membranes, the hydrophilic domains establish continuous ion transport pathways for OH^-, ensuring high ion conductivity, while the hydrophobic domains suppress excessive swelling of the membrane, ensuring high mechanical strength [9]. Therefore, further systematic experimental studies of microphase-separation structures and molecular dynamic modelling studies are recommended to correlate different functional headgroup chemistries and polymer backbones and membrane performance and alkaline stability, enabling rational design and optimisation of anion exchange membrane [10]. As discussed before, due to the drawbacks of cation and anion exchange membranes, these membranes have become a main bottleneck for the development of industrial-scale electrolyser [11]. To address these challenges, the replacement of membrane-assisted electrolysers with innovative membraneless electrolysers, where no physical separator is placed between the anode and cathode chamber, have emerged as a new research direction [12]. Membraneless electrolysers can be generally categorised into two main approaches based on the electrode type: flow-through and flow-by electrodes. The flow-by approach based on directing the electrolyte to flow to the surface of closely spaced flat electrodes within the reaction chamber, where laminar flow of electrolyte develops distinct oxygen and hydrogen bubble streams via the Segrè–Silberberg [13]. The flow-through on the other hand contains porous electrodes (e.g. metallic mesh) allowing the flowing of the electrolyte divergently by placing a divider between the hydrogen and oxygen streams, separating the hydrogen and oxygen bubbles. Nevertheless, the flow-by approach experiences low efficiency due to the high resistance arising from the formation of gas bubbles in between the electrode space, while the flow-through approach also experiences low efficiency since the closer spacing between electrodes requires high pumping power to maintain electrolyte flow [13]. Lastly, AI-driven modelling and machine learning are recommended to accelerate the rational design (or discovery of new synthetic routes) of advanced catalysts and membranes with optimal performance and durability, and the optimisation of electrolyser systems featuring simpler, more cost-effective, and energy-efficient designs.

References

[1] R. Lohmann, I.T. Cousins, J.C. Dewitt, J. Glüge, G. Goldenman, D. Herzke, A.B. Lindstrom, M.F. Miller, C.A. Ng, S. Patton, M. Scheringer, X. Trier, Z. Wang, Are Fluoropolymers Really of Low Concern for Human and Environmental Health and Separate from Other PFAS?, Environ. Sci. Technol. 54 (2020) 12820–12828, https://doi.org/10.1021/acs.est.0c03244.

[2] H. Nguyen, F. Lombeck, C. Schwarz, P.A. Heizmann, M. Adamski, H.F. Lee, B. Britton, S. Holdcroft, S. Vierrath, M. Breitwieser, Hydrocarbon-based Pemion^{TM} proton exchange membrane fuel cells with state-of-the-art performance, Sustain. Energy Fuels 5 (2021) 3687–3699, https://doi.org/10.1039/d1se00556a.

[3] G. Wei, L. Xu, C. Huang, Y. Wang, SPE water electrolysis with SPEEK/PES blend membrane, Int. J. Hydrogen Energy 35 (2010) 7778–7783, https://doi.org/10.1016/j.ijhydene.2010.05.041.

[4] E.J. Park, C.G. Arges, H. Xu, Y.S. Kim, Membrane Strategies for Water Electrolysis, ACS Energy Lett. 7 (2022) 3447–3457, https://doi.org/10.1021/acsenergylett.2c01609.

[5] C. Klose, T. Saatkamp, A. Münchinger, L. Bohn, G. Titvinidze, M. Breitwieser, K.D. Kreuer, S. Vierrath, All-Hydrocarbon MEA for PEM Water Electrolysis Combining Low Hydrogen Crossover and High Efficiency, Adv. Energy Mater. 10 (2020) 1903995, https://doi.org/10.1002/aenm.201903995.

[6] K. Yassin, R. Attias, Y. Tsur, D.R. Dekel, Identifying and Quantifying Loss Sources in Anion-Exchange Membrane Water Electrolyzers, ACS Electrochem. 1 (2025) 655–666, https://doi.org/10.1021/acselectrochem.4c00156.

[7] L. Liu, H. Ma, M. Khan, B.S. Hsiao, Recent Advances and Challenges in Anion Exchange Membranes Development/Application for Water Electrolysis: A Review, Membranes 14 (2024) 85, https://doi.org/10.3390/membranes14040085.

[8] J. Luque Di Salvo, G. De Luca, A. Cipollina, G. Micale, Effect of ion exchange capacity and water uptake on hydroxide transport in PSU-TMA membranes: A DFT and molecular dynamics study, J. Memb. Sci. 599 (2020) 117837, https://doi.org/10.1016/j.memsci.2020.117837.

[9] N. Du, C. Roy, R. Peach, M. Turnbull, S. Thiele, C. Bock, Anion-Exchange Membrane Water Electrolyzers, Chem. Rev. 122 (2022) 11830–11895, https://doi.org/10.1021/acs.chemrev.1c00854.

[10] S. Gong, A. Liu, N.A. Qaisrani, L. Han, M. Yuan, Y. Ren, X. Yan, G. He, F. Zhang, Completely Methylene-Free Side Chain Enables Significant Microphase Separation at Medium IECs for Fuel-Cell Anion Exchange Membranes, ACS Appl. Mater. Interfaces 16 (2024) 27741–27749, https://doi.org/10.1021/acsami.4c03693.

[11] A.G. Olabi, A. saleh Bahri, A.A. Abdelghafar, A. Baroutaji, E.T. Sayed, A.H. Alami, H. Rezk, M.A. Abdelkareem, Large-vscale hydrogen production and storage technologies: Current status and future directions, Int. J. Hydrogen Energy 46 (2021) 23498–23528, https://doi.org/10.1016/j.ijhydene.2020.10.110.

[12] A. Manzotti, E. Quattrocchi, A. Curcio, S.C.T. Kwok, M. Santarelli, F. Ciucci, Membraneless electrolyzers for the production of low-cost, high-purity green hydrogen: A techno-economic analysis, Energy Convers. Manag. 254 (2022) 115156, https://doi.org/10.1016/j.enconman.2021.115156.

[13] K. Sravan Kumar, S. Mateo, A.R. de la Osa, P. Sánchez, A. de Lucas-Consuegra, Advancements in membrane-less electrolysis configurations: Innovations and challenges, Curr. Opin. Electrochem. 49 (2025) 101602, https://doi.org/10.1016/j.coelec.2024.101602.